Quantitative Vascular MRI in the Placenta

By
Ruiming Chen

A dissertation submitted in partial fulfillment of
the requirements for the degree of

Doctor of Philosophy
(Medical Physics)

at the
UNIVERSITY OF WISCONSIN-MADISON
2024

Date of final oral examination: 04/25/2024

The dissertation is approved by the following members of the Final Oral Committee:

Oliver Wieben, Professor, Medical Physics
Kevin M. Johnson, Associate Professor, Medical Physics
Diego Hernando, Associate Professor, Medical Physics
Kathleen Antony, Clinical Assistant Professor, Obstetrics and Gynecology
Thaddeus G. Golos, Professor, Reproductive Sciences

Acknowledgements

This work would not have been possible without the help from my mentors, family, and friends. I first would like to thank my research advisor Oliver Wieben, who guided me not only through my research, but also in life. Before joining Oliver's group, I suffered from anxiety issues and was struggling to find a healthy work-life balance. Oliver's positive attitude on life and his "work hard, play hard" philosophy really inspired me to focus on the bigger picture that not only involves making scientific discoveries, but also becoming a well-rounded person that enjoys life as one should.

I would also like to thank my thesis committee members, Kevin Johnson, Diego Hernando, Kathleen Antony, and Ted Golos, for their invaluable help and support through the many mentoring meetings and one-on-one meetings. They always made sure that I was on the correct path in research, and provided exciting new directions that I could pursue.

Third, I would like to thank my Wieben lab mates, past and present, whose friendship I will cherish forever. The help and guidance from alumni Carson Hoffman, Phil Corrado, Grant Roberts, and Dan Seiter lead me into the world of MRI research, and my work would be impossible without the foundation built by them (and many others before them). Special thanks to honorary Wieben lab member, Ante Zhu, for her guidance on placental MRI. My current lab members, Alma Spahic, Tarun Naren, Ruo-Yu Liu, and Tim Houston are some of the most talented collaborators and friends I have ever known. Our lab is a family, and I am grateful that I am a part of it.

In addition, I would like to thank my friends from the department of Medical Physics, Thomas Lilieholm, Yurim Lee, Ruvini Navaratna, Andrew McVea, Jayse Weaver, Xin Tie, and Chenwei Tang, for their constant support from day one.

Lastly, I would like to thank my family for their support in me pursuing a doctorate in medical physics. To my parents in China, thank you for sending your only child half away across the world to pursue her dreams. I know it must not have been easy. I am very lucky to have you as my parents. To my husband Aidan, my best friend, thank you for always being there through all the highs and lows, and I can't wait to see what the future holds for us.

Abstract

The development of utero-placental vasculature plays a significant role in placental health and fetal growth. Abnormal maternal placental vasculature such as local malperfusion can lead to gestational complications such as fetal growth restriction and preeclampsia. Current clinical standard care lacks noninvasive diagnostic tests that can reliably identify patients at risk for such complications early in pregnancy.

MRI is a powerful imaging tool that can assess placental vascular health without the use of ionizing radiation. Compared to ultrasound, MRI can generate various imaging contrasts and probing physiological relevant parameters through quantitative measures (qMRI). A multidisciplinary UW team has pursued novel MR approaches to quantify vascular function and health through measures of macrovascular blood flow, global and local perfusion, oxygenation, and inflammation. These methods laid the foundation of the works presented in this thesis.

The use of exogenous contrast agents allows for improved visualizations of the maternal and placental vasculature. However, only few MR studies have used contrast agents because the most clinically commonly used agents are Gadolinium chelates that pose safety concerns in pregnancy. This work presents the first investigations of using ferumoxytol for placental blood volume estimates. Iron nanoparticle based ferumoxytol is FDA approved for the treatment of anemia and has recently found use as an off-label MR contrast agent, including clinical use in pregnant patient populations. As such, it has potential for a clinically used MRI contrast agent in pregnancy.

In this thesis, I present measurements of quantitative placental qMRI markers obtained either with endogenous contrast or with the use of ferumoxytol. Specifically, I quantitatively

measured and analyzed perfusion and T2* maps without the use of an exogeneous contrast agent. For a human cohort of 97 subjects, early gestation (14 and 20 weeks) T2* values were reported and analyzed assess predictabilities of T2* of gestational complications early pregnancy. Second, I developed methodology for placental blood volume measurements and demonstrate its feasibility in the rhesus macaque and humans. This approach enables the measurements of blood volume in-vivo for the first time. Third, I assessed the diagnostic feasibility of qMRI markers including placental blood volume and cotyledon-specific placenta blood flow in rhesus macaque models with placental injury. I also improved the previous dynamic contrast enhanced (DCE) MRI algorithm to improve the previous 2D watershed algorithm to a 3D method for cotyledon segmentation. Lastly, I introduced a multi-modal analysis and mapping workflow using DCE and T1-mapping data that could potentially improve diagnostic efficacy on placental injury. I hope the projects described in this thesis could motivate early-gestation in-vivo detection of placental vasculature deficiencies.

Table of Contents

Acknowledgements ..... *i*

Abstract ..... *iii*

Table of Contents ..... *v*

List of Tables ..... *ix*

List of Figures ..... *x*

List of Equations ..... *xiii*

Chapter 1. Introduction *1*

1.1 Background **1**

1.1.1 Placental Anatomy and Function 2

1.1.2 Placental Quantitative MRI 5

1.1.3. UW-Madison Placenta MRI Studies 10

1.2 Innovation **11**

1.3 Chapter Outline **13**

Chapter 2. Measuring Longitudinal Placental Perfusion of Zika-Infected Rhesus Macaque Placenta using VS-ASL *15*

2.1 Introduction **15**

2.2 Methods **17**

2.3 Results **20**

2.4 Discussion and Conclusion **23**

Chapter 3. Longitudinal Study on Early Gestation T2-based BOLD effect in Human Placenta* *26*

3.1 Introduction **26**

3.2 Methods **27**

3.3 Results **29**

3.4 Discussion **34**

Chapter 4. Maternal Placental Blood Volume Measurements: Methodology and Applications *37*

4.1 Introduction **37**

4.2 Variable Flip Angle (VFA) T1-Mapping **40**

4.3 Blood Volume Calculation **41**

4.4 Application 1: Longitudinal Placental Blood Volume Measurements in Zika-Infected Rhesus Macaques using Ferumoxytol-Enhanced MRI **44**

4.4.1 Methods 44

4.4.2 Results 46

4.4.3 Discussion 51

4.5 Application 2: Maternal Placental Blood Volume Measurement of Human Placenta with Fetal Growth Restriction **54**

4.5.1 Methods 54

4.5.2 Results 55

4.5.3 Discussion 59

4.6 Application 3: Maternal Placental Blood Volume Measurement of Rhesus Macaques with Placental Injury **60**

4.6.1 Methods 60

4.6.2 Results 61

4.6.3 Discussion 64

Chapter 5. Cotyledon-Specific Flow Evaluation of Rhesus Macaque Placental Injury using Ferumoxytol Dynamic Contrast-Enhanced MRI ***66***

5.1 Introduction **66**

5.2 Methods **67**

5.3 Results **72**

5.4 Discussion **78**

Limitations **80**

5.5 Conclusions **81**

Chapter 6. Vasculature Assessment of Rhesus Macaque Placental Injury using Variable Flip Angle T1-Mapping and Dynamic Contrast Enhanced MRI ***83***

6.1 Introduction **83**

6.2 Methods **84**

6.3 Results **86**

6.4 Discussion **91**

Chapter 7. Summary and Future Work ***93***

7.1 Summary **93**

7.2 Future Work 96

7.2.1 Cotyledon-Specific Correlations with Pathology: Blood Volume and DCE-MRI 96

7.2.2 Big-Data Analysis: Placental Shape, Surface Area, Implantation Site, and More 99

7.2.3 Quantifying Placental Inflammation using T2* Mapping 100

7.2.4 Assessing the Capability of Fe-Enhanced MRA to Visualize Maternal Placental Vasculature 101

Bibliography ***..... 103***

List of Tables

Table 1. Overview of UW placenta MRI studies. 11

Table 2. Information on the pregnant rhesus macaques. 19

Table 3. Comparison of the VS ASL median perfusion measures obtained from the central slice and whole placenta. 23

Table 4. T2* values (mean and standard deviation) for all obese and non-obese subjects, and subjects with various gestation outcomes. 32

Table 5. T2* values in muscle ROI for 10 subjects at 14- and 20-week gestation. 34

Table 6. Rhesus blood volume measurement results. 48

Table 7. Mean values for scans 1 and 2 and maternal blood volume measurements for all three subjects. 57

Table 8. Rhesus macaque treatment, imaging, and delivery date, in gestation day. 68

Table 9. Cotyledon volume, flow per cotyledon, normalized flow per cotyledon, and total flow for each animal at the third imaging timepoint (GD ~145). 73

List of Figures

Figure 1. Placental Structure. The fetal side of vasculature is characterized by the connection to the umbilical cord. The maternal side consists of various maternal feeding arteries that extends into the intervillous space, where the nutrient and oxygenation exchanges occur. Credit: Jansen CHJR, et al. Acta Obstet Gynecol Scand. 2020.....2

Figure 2. Vascular supply of the human placenta. Four major arteries carry oxygenated blood to the uterus, which then is exchanged with the fetus through connection of the umbilical cord to the placenta. Image courtesy of Jacob Macdonald. 3

Figure 3. Placental development across gestation. Credit: The Human Placenta Project. https://www.nichd.nih.gov/research/supported/human-placenta-project 5

Figure 4. Interleaved multi-slice VS-ASL sequence paradigm shown for 4 slices. Image Courtesy of Dr. Kevin Johnson. 19

Figure 5. Perfusion map of six consecutives anterior (A) to posterior (F) slices of a control subject. 21

Figure 6. Median VS ASL perfusion as a function of gestation age. 22

Figure 7. Data selection for this study. 29

Figure 8. Anatomic image (water map) and T2* map for a control subject at 14 and 20 weeks of pregnancy. Image courtesy of Dr. Ante Zhu. 30

Figure 9. Box-and-whisker plots of 14-week, 20-week, and Δ T2* values, with the T2* values of abnormal gestational outcome overlaid on top. 31

Figure 10. Averaged histograms of pixel-wise placental T2* values for week 14 and week 20 grouped by pregnancy complications. 33

Figure 11. Plots of median T2* and birth weight vs birthweight (column 1) and placental volume vs birth weight (column 2). 36

Figure 12. Sample SPGR signal and its relationship with flip angles. 43

Figure 13. Variable flip angle R1 mapping protocol for Ferumoxytol MRI in rhesus. 45

Figure 14. Sample placenta (yellow) and vessel ROI (red) segmentation. 46

Figure 15. Variable flip angle images. 47

Figure 16. Representative fractional blood volume maps. 47

Figure 17. Longitudinal plots of maternal placental blood volume. 49

Figure 18. Pixel-wise blood volume histograms. 50

Figure 19. Image acquisition workflow for this study. 55

Figure 20. T1-weighted anatomical image (flip angle = 15°) used for segmentation and R1 map for corresponding slice position. 56

Figure 21. Three non-consecutive slices (left to right) of contrast-enhanced T1-weighted anatomical images (flip angle = 15°) for each subject (top to bottom) used for segmentation. Slice location selected differ for each subject. 57

Figure 22. Eight slices (non-consecutive) showing maternal fractional blood volume (mFBV) distribution (heat map) overlaid on top of the T1-weighted anatomical images....58

Figure 23. Maternal fractional blood volume (mFBV) and ΔR1 histograms for each subject. 59

Figure 24. Mean FBV as a function of gestation age for all six subjects....62

Figure 25. Three non-consecutive slices (left to right) imaged for three gestational timepoints (top to bottom) of one Tisseel-treated subject, and a control subject (bottom row). 63

Figure 26. R1 and maternal fractional blood volume (FBV) and for a Tisseel-treated subject and a control subject at all three gestational timepoints (GTPs). 64

Figure 27. Dynamic contrast enhanced MRI processing workflow. 71

Figure 28. Histopathological central slice of placenta treated with Tisseel injection....73

Figure 29. Longitudinal plots of placental surface area, placental volume, and total maternal flow across three imaging timepoints for all eleven animals. 74

Figure 30. Box-and-whisker plots of flow, volume, and normalized flow of each cotyledon for each gestational timepoint (GTP; left to right). 76

Figure 31. Contrast arrival time maps for each gestational timepoint (A), a photo of the placenta at dissection (B), and arrival time histograms (C) at available gestational time points (GTP) for a Tisseel-treated and a control animal. 77

Figure 32. Imaging workflow for this study. 86

Figure 33. Co-registered Fractional blood volume map (left column), time-averaged dynamic contrast enhanced (DCE) signal (middle column), and T1-weighted post-contrast anatomical image (right column) used for blood volume calculation. 87

Figure 34. Heat maps of fractional blood volume (left column) and contrast arrival time maps (right column) of the three subjects..... 89

Figure 35. Density maps of pixel-wise locally corresponding fractional blood volume (FBV) vs. normalized time-averaged DCE signal (left column) and vs. contrast arrival time (right column). 90

Figure 36. Placental Necrosis and Ischemia Quantification Methodology Workflow. Image courtesy of Logan Keding. 98

Figure 37. Placental implantation site characterization. Image courtesy of Dr. Philip Corrado. 100

List of Equations

Equation 1. perfusion (p) shown as a ratio percentage of tag on/off difference over PDW.....18

Equation 2. SPGR signal. 40

Equation 3. Rearranged SPGR signal showing linear relationship. 40

Equation 4. Maternal fractional blood volume.....41

Equation 5. Maternal placental blood volume. 41

Equation 6. Concentration (C) of ferumoxytol in blood. 42

Equation 7. Total maternal blood volume. 42

Chapter 1. Introduction

1.1 Background

The overall goal of the proposed work is to develop and evaluate quantitative MRI-based biomarkers for the assessment of placental health, particularly in early gestation. Current diagnostic tests used in clinical care are insufficient to reliably identify patients at high risk for several pregnancy complications[1]. Ultrasound (US) is widely used for clinical in vivo imaging in pregnancy but has limitations in assessing placental health, including 3D coverage, relatively unreliable measurements of placental flow because of vessel tortuosity, and lack of relevant quantitative biomarkers. In 2014, the Eunice Kennedy Shrive National Institute of Child Health and Human Development (NICHD) of the National Institutes of Health (NIH) created a program, the Human Placenta Project (HPP), in an attempt to address this diagnostic gap with the development of real-time, non-invasive diagnostics tests including imaging without ionizing radiation[2].

MRI is capable to quantify vascular function and health through measures of macrovascular blood flow[3], global and local perfusion[4], oxygenation[5], and inflammation[6] of organs including the brain, heart, liver, and kidneys. The biggest hurdles for adapting similar measures to the placenta have been (1) motion artifacts (mother's breathing, fetal body motion, cardiac motion, and pulsatility of two cardiovascular systems. While rhythmic motion artifacts from breathing and cardiac motions can be mitigated with respiratory bellows and cardiac ECG gating, irregular movements such as peristaltic motion and Brackston Hicks contractions need to be treated with thorough post-processing techniques. (2) the small size of the placental/uterine vessels in early gestation. Although increased resolution of image acquisition could provide more detailed information, the prolonged imaging time exacerbates patient discomfort and leads to

potential of motion. (3) its unique physiology with maternal and fetal blood supply and terminal villi. Recent advances in MR methodology by multiple groups including ours, supported by the NICHD HPP and other funding mechanisms, have demonstrated the feasibility of functional placental measures[3,7–12]. However, they often lack normative values across gestation, specifically in early gestation, and remain largely untested in relevant pathophysiological settings.

1.1.1 Placental Anatomy and Function

The placenta is a transient yet crucial organ that plays a critical role in maternal and fetal exchanges of nutrients and oxygen throughout gestation. The placenta consists of both maternal and fetal vasculature and tissue structures. Upon placental implantation, uterine spiral arteries on the maternal side undergo extensive remodeling that supplies blood flow to the placenta. On the fetal side, branched fetal placental villi are originated from the umbilical cord, which connects the placenta to the fetus.

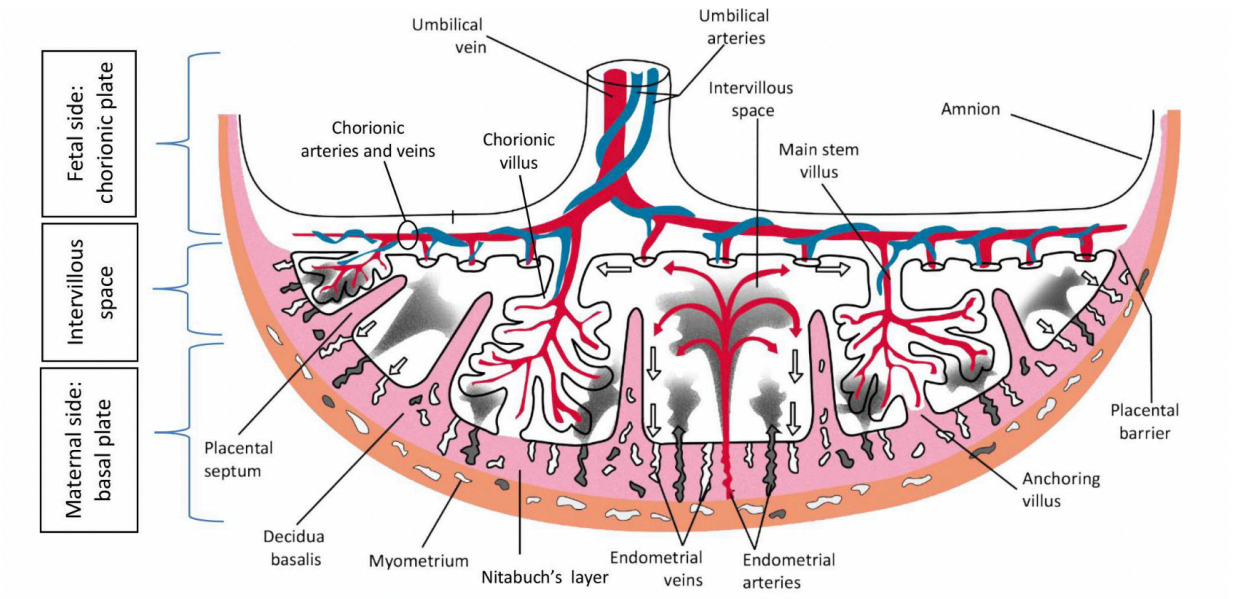

Figure 1. Placental Structure. The fetal side of vasculature is characterized by the connection to the umbilical cord. The maternal side consists of various maternal feeding arteries that extends into the intervillous space, where the nutrient and oxygenation exchanges occur. Credit: Jansen CHJR, et al. Acta Obstet Gynecol Scand. 2020

Separating the maternal and fetal side is the intervillous space, where the nutrient exchanges occur[13]. The intervillous space for human placenta is separated into fifteen to twenty individual placental functional units, or cotyledons. Each cotyledon is fed by a different incoming maternal artery and operates near independently to facilitate nutrient exchanges[14]. Human placenta has only one disc-shaped lobe, whereas non-human primates (rhesus macaques) typically have two lobes. The primary lobe directly connects to the fetus via the umbilical cord, whereas the secondary lobe is connected to the umbilical cord through bridging vessels[15].

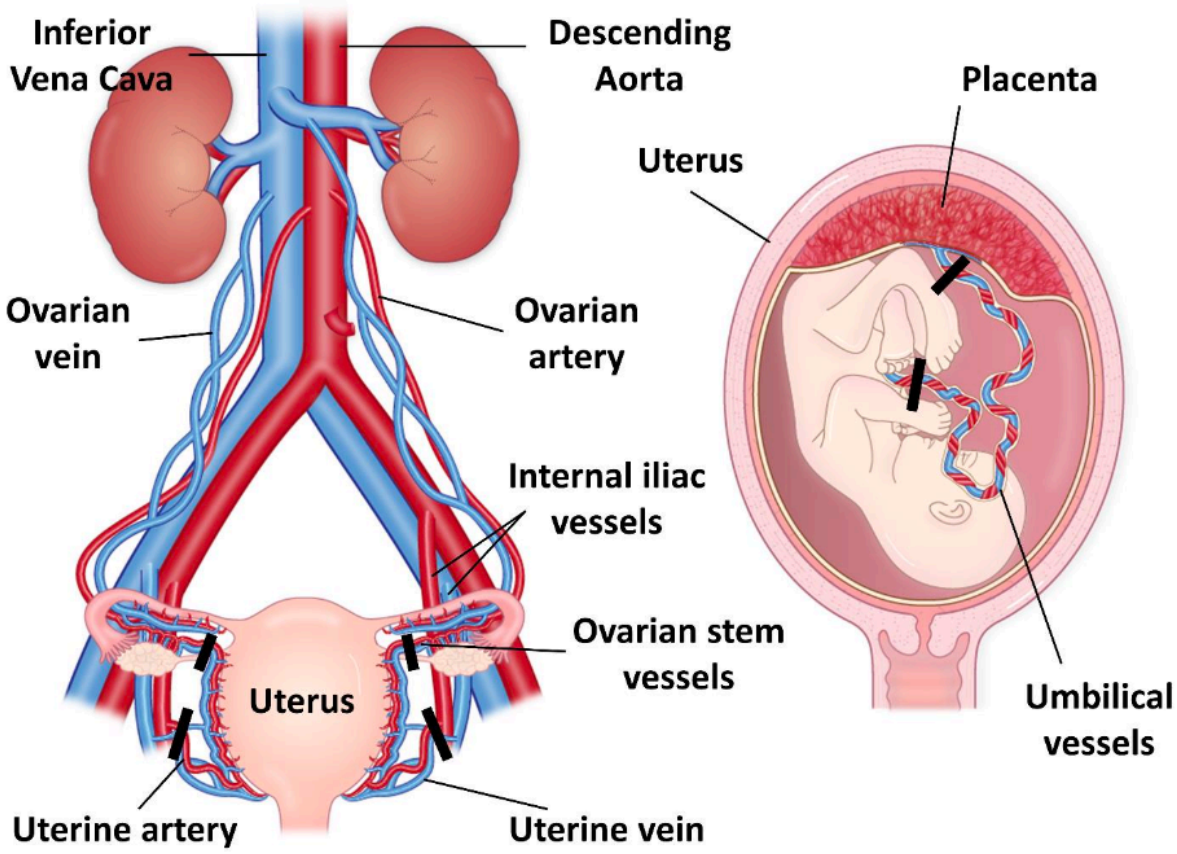

Figure 2. Vascular supply of the human placenta. Four major arteries carry oxygenated blood to the uterus, which then is exchanged with the fetus through connection of the umbilical cord to the placenta. Image courtesy of Jacob Macdonald.

The vascular supply of the human placenta is rather complex. Figure 2 shows a diagram of major vasculature supplying the placental nutrient exchange. On the maternal side, uterine arteries (left and right), and the two uterine branches of the ovarian arteries supply oxygen and nutrient-rich blood to the uterus, which then delivers to the fetus through placenta [15]. On the fetal side, the umbilical cord (containing two umbilical arteries) returns deoxygenated blood to the placenta.

Abnormal placental vasculature developments, if left untreated, could result in increased risk of gestational complications and failure. Structural abnormalities of the placenta and its vasculature could prevent sufficient nutrient exchanges between the mother and the fetus[14]. Viral infections of otherwise healthy placental tissue and structure, if affecting significant number of cotyledons, could trigger an inflammatory response that might lead to abnormal blood flow[16]. additionally, large areas of placental tissue infarctions, characterized by deprivation of blood flow in sections of the placenta, could increase the risk of gestational failure resulting from placental mal-perfusion[13].

Clinically, successful development of placental vasculature is closely linked to satisfactory gestational and delivery outcomes[13]. Abnormal placental development could result in gestational complications such as fetal growth restriction (FGR), small for gestation age (SGA), pre-eclampsia, and pre-term birth[1,13,17]. Placenta-related FGR is associated with mal-perfusion of the placental tissue, which originates from insufficient development of utero-placental vasculature[13,17]. If identified late and/or left untreated, late-onset FGR, which affects 5-10% of pregnancies, could result in neonatal morbidity, mortality, and higher chances of adult disease[18,19].

Additionally, maternal obesity is associated with higher risk of gestational complications, potentially due to insufficient placental flow[16]. High vascular resistance can impede the maternal-fetal nutrient exchange, as well as sufficient oxygenation, resulting in uteroplacental hypoxia[20].

Such complications include gestational diabetes, hypertension, pre-eclampsia, and pre-term birth[21]. Therefore, proper screening of this high-risk group at early gestation could be very valuable to early discovery and intervention of potential gestational complications currently not possible.

1.1.2 Placental Quantitative MRI

Early in-vivo identification and diagnosis of placental pathology could allow for longer time window for intervention and treatment. Specifically, first-trimester is crucial to healthy developments of the fetus, due to the fetus' vulnerability to adverse pregnancy outcomes[22]. Therefore, it is of great clinical value to improve the diagnostic efficacy of early-gestation abnormalities in-vivo.

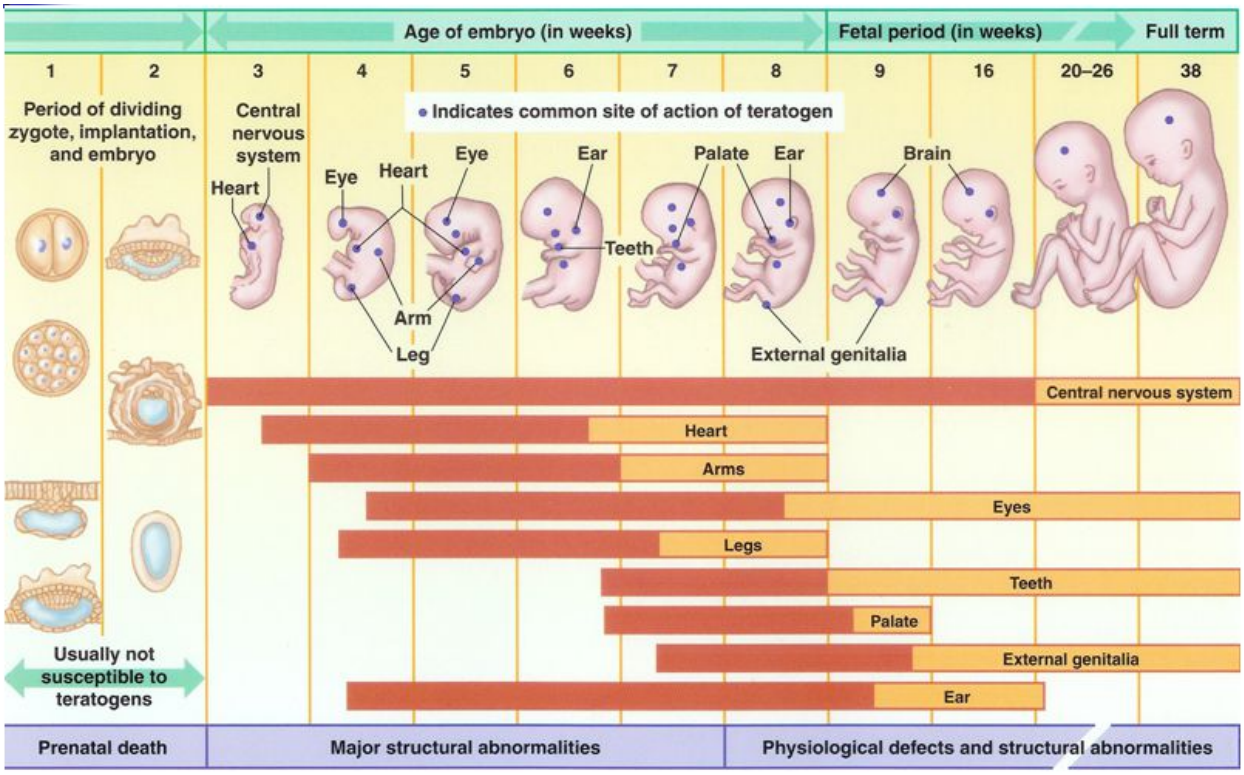

Figure 3. Placental development across gestation. Credit: The Human Placenta Project. https://www.nichd.nih.gov/research/supported/human-placenta-project

Currently, ultrasound is widely used clinically for in vivo imaging in pregnancy as a screening and diagnostic tool. The advantages of ultrasound include cost-effectiveness, accessibility, and faster imaging time. However, ultrasound also has limitations in assessing placental vascular health including relatively unreliable measurements of macroscopic placental blood flow because of low resolution, vessel tortuosity and lack of relevant quantitative imaging markers[23]. Alternatively, MRI provides a framework to quantify vascular function and health through measures of macrovascular blood flow[3], global and local perfusion[4], oxygenation[5], and inflammation[6] of organs including the brain, heart, liver, and kidneys. Recent advances in placental MRI have enabled the assessment of various quantitative markers such as placental perfusion[24], blood oxygenation level dependent (BOLD) effects[25], native R2*/T2* quantification[8], and direct blood flow measures[26]. These 3-dimentional quantitative metrics provide unique depictions of placental structure and health and provides room for future investigations in new quantitative markers indicative of placental pathology.

This thesis investigates several quantitative MRI (qMRI) markers that could reflect placental vasculature health and development. R2* and perfusion using arterial spin labeling (ASL) technique do not require the use of exogeneous contrast agents, and therefore are qMRI markers for both maternal and fetal vasculature. Maternal blood volume, dynamic contrast enhanced (DCE) – based placental blood flow measurements require the intravascular infusion of Ferumoxytol into maternal circulation, and therefore only able to reflect the qMRI measurements on the maternal side.

Blood Oxygenation Level Dependent (BOLD) MRI. Placental R2* is a qMRI marker that has shown great promise in approximating oxygenation levels in the placenta[1,27,28]. T2* is lower in hypoxic tissues due to the presence of deoxyhemoglobin. T2* itself is additionally sensitive to

changes in susceptibility from iron loading and changes in T2 due to microstructure changes. However, changes in T2* serve as a surrogate for local pO2 changes, and therefore could relate to tissue oxygenation levels and its potential role in maternal and fetal oxygenation exchanges. Previous studies have investigated placental baseline T2* values for gestation ages between 24 to 40 weeks for subjects with FGR. These studies showed a longitudinal decrease in mean placental T2* with gestation, as well as lower T2* for subjects with severe FGR [29,30]. Placental R2* sequences with and without hypoxia challenges have been adopted[11,31]. Though widely available, pursued by various research groups, and considered for multi-site studies[7], the sensitivity of BOLD as a global or local measure of placental health remains unclear [29,32–34]. T1 relaxometry has also been shown to reflect tissue morphology and oxygenation[35]. Additionally, combining relaxation times (T2, T2*, T1) might permit estimation of SO2, pO2, and hematocrit levels of the placental vessels[11]. Previous studies have shown a decrease of mean placental T2* value with gestation age, as well as a decrease of mean T2* for placenta with gestational complications[1,17,27]. However, few studies have explored T2* measurements of early gestation age, namely less than 20 weeks[36].

Arterial Spin Labeling Perfusion MRI. Placental perfusion is a biomarker which indicates the quantity of blood in a given amount of placental tissue[37]. Importantly, abnormal placental perfusion is associated with pregnancy complications including preeclampsia[32]. Local perfusion information (such as a perfusion map) could potentially lead to identification of low perfusion zones, which could indicate local ischemia. Additionally, global perfusion information (such as mean, median, and standard deviation of perfusion values) could reflect the overall placental vasculature development, allowing for comparison between controls and diseased models.

Arterial Spin Labeling (ASL) perfusion MRI[38] is a compelling method to safely and non-invasively assess local perfusion without the need for an exogenous contrast agent. However, the

application of ASL perfusion MRI in the placenta poses unique challenges, including (1) motion artefacts (fetus and maternal breathing motion), (2) variability in placental geometry and location, (3) dual blood supply (maternal and fetal), (4) extremely long transit times from the arteries into the intervillous space, and (5) fetal and maternal bulk motion. FAIR ASL[10,39–41] is limited to single slice acquisitions and pseudo-continuous (PC) ASL[26,42,43] is commonly used in vascular regions such as the brain but requires careful selection of tagging regions which are not conducive for placenta imaging due to the location and tortuous path of the feeding maternal arteries.

Velocity-selective (VS ASL) MRI[44] has emerged as an alternative approach where tagging is achieved based on its velocity instead of location, which makes it highly reproducible. Its feasibility for placenta imaging has been recently demonstrated for a 3D spiral sequence[45] and 2 studies have reported successful perfusion measurements in the placenta and the fetus [46,47], but lack measurements early in pregnancy when they would be most useful for risk prediction.

Contrast enhanced MRI with Ferumoxytol: DCE Perfusion, MRA, Blood Volume, and Safety. Contrast agents are routinely used for dynamic contrast enhanced (DCE) MRI perfusion and static MR angiography (MRA)[24]. While Gadolinium (Gd) has been used in nonpregnant human subjects, pregnant non-human primate experimental models[48], and a pilot study in human pregnancy (n=6)[49], concerns about its teratogenic potential and confirmation that it can be transported across the placenta to the fetal compartment[50] limit its potential for diagnostic application. Ferumoxytol (Feraheme®, AMAG Pharmaceuticals, Waltham, MA), a superparamagnetic iron oxide nanoparticle (SPION) approved for the treatment of anemia, is a compelling off-label intravascular contrast agent that is increasingly used for MRI[51–54] with regional T1 and T2* shortening, a long intravascular residency time (~14.5 hrs), and potential for clinical placenta imaging.

Ferumoxytol has been shown to be well tolerated, associated with no serious adverse events, and implicated in few (1.8% mild and 0.2% moderate) adverse reactions in a multi-center MRI safety study of 4240 subjects stretching over 15 years[55]. In 2015, the FDA identified bolus injection of undiluted ferumoxytol as a potential risk factor and issued updated therapeutic prescription recommendations that included dilution, infusion over 15 minutes (originally over 17 seconds), and hemodynamic monitoring for up to 30 minutes after infusion[56]. As such, DCE perfusion MRI will not be pursued in human studies in this proposal although it provides unique insights into placental organization into functional units and their individual kinetics in preclinical studies[57]. Instead, a slow infusion with subsequent steady state imaging will be used in human studies with ferumoxytol. Slow infusion ferumoxytol- (Fe) enhanced MRI is routinely conducted for clinically indicated contrast-enhanced MRI in pregnant patients at our and other institutions and we recently reported safe use of Fe in 70 clinical studies of pulmonary MRA exams in pregnancy[57].

We also note that ferumoxytol is widely considered by obstetricians as an option to treat iron-deficiency anemia in pregnancy, and its usage as a diagnostic imaging agent is a straightforward extension. Besides being used for MRA and structural imaging, MRI with ferumoxytol has also been demonstrated to enable placental fractional blood volumes in mice[58]. Additionally, Fe delivers iron by macrophage phagocytosis with highest density in the reticuloendothelial system but can be taken up by those cells mobilized as part of any inflammatory response[59]. Thus, uptake of ferumoxytol by decidual macrophages provoked by inflammation might allow to localize and potentially quantify these inflammatory cells present in the decidua and associate with placental pathology and development of FGR, but it remains unclear if such uptake will occur in MR measurable quantities.

Recently, Badachhape et al. estimated fractional blood volume (FBV) in pregnant mice from 2 image sets acquired before and after contrast injection of blood-pool liposomal gadolinium-based contrast agents (GABA) to assess maternal-side placental perfusion and found good agreement with nanoparticle contrast-enhanced computed tomography (CE-CT) [58]. Maternal placental blood volume is a placental biomarker that indicates placental perfusion, which is related to vascular health and development[37]. Such measures can possibly identify placental insufficiency that are indicative of local ischemia or fetal growth restriction (FGR).

1.1.3. UW-Madison Placenta MRI Studies

For about 7 years and counting, an interdisciplinary team at the UW is involved in placenta MR imaging for several non-human primate and human pregnancy studies. Table 1 provides an overview of the studies, which differed in purpose, imaging time points in respect to gestation, the use of ferumoxytol, and other factors. Briefly, study 1 was designed to establish and optimize novel quantitative MR sequences in the rhesus macaque. Study 2 was designed to adopt these sequences to human imaging in a small human pilot. Study 3 used these sequences in a large patient population across a wide range of body mass index BMI including some patients with pregnancy complications. In a parallel study number 5, qMRI was used to study rhesus macacques injected with Zika virus. In an ongoing and funded study, we are using qMRI in a novel animal model of placental infarct and inflammation (study 7). We also obtained approvals for the use of ferumoxytol in human subjects and have conducted a small pilot study (study 4, n=3) and hope to generate funding for a larger scale human FGR study with ferumoxytol (study 4). This thesis will draw data from the completed studies 3-5 and will be expanded by incoming data from study 7.

Table 1. Overview of UW placenta MRI studies.

Study #	Name of Study	# of Subjects	GA Imaged	Status	Fe (yes/no)
1	Rhesus U01	12	~day 100	completed	yes
2	Human Pilot	10	14&20 wks	completed	no
3	Human Main Study	97	14&20 wks	completed	no
4	Human FGR	3	36 wk	completed	yes
5	Rhesus Zika	14	~day 55/100/145	completed	yes
6	Rhesus Liposome	3	~ day 100	completed	yes
7	Rhesus Injury	13	~day 100/145	ongoing	yes

Columns (from left to right) are study number, the abbreviated name of the study, number of subjects, gestation age (days or weeks) of imaging, the progress of data acquisition, and whether ferumoxytol is administered in the scan.

1.2 Innovation

There are various aspects of innovation in this work, including novel methodology development, generation of normative quantitative MRI biomarkers in rhesus macaques and humans, and assessing the suitability of imaging biomarkers to detect placental pathology.

Maternal placental blood volume: A major innovation of my thesis work was the development, implementation, and evaluation of methodology to quantify maternal placental blood volume using ferumoxytol enhanced MRIm which we achieved with variable flip angle (VFA) T1 mapping. To our knowledge, this is the first approach to to non-invasively assess

maternal placental blood volumes and our team at UW Madison is the first worldwide to obtained approvals and present results for the use of ferumoxytol in preclinical and human research studies.

Detection of placental infarcts: The underlying concept of using dynamic contrast-enhanced MRI and maternal placental blood volume for the detection of placental infarcts had been previously proposed and developed by our team but was never demonstrated in the presence of such infarcts. Here, I adopted and revised the methodology for robustness and demonstrated, for the first time, its utility in newly developed animal models of placental injury..

Multi-modal analysis of placental qMRI markers: Placental function can be assessed by multiple MRI biomarkers, including oxygenation and perfusion[9]. For example, combining voxelwise measurements of relaxation times (T2*, T2, T1) might permit estimation of SO2, pO2, and hematocrit levels of the placenta[11]. Previous studies have investigated multimodal comparisons between placental anatomy, placental diffusion, and T2* mapping in human subjects[60]. Another study found similar patterns between T2* maps and early uptake using DCE MRI in rhesus macaques[61]. In this thesis, I expanded on previous studies and investigated the correlation between relaxometry and blood volume maps for controls and rhesus macaques with placental injury in a first of its kind study.

Normative T2* values: This thesis generates currently lacking normative early gestation R2* values for a relatively large patient cohort (n=97) of normal BMI and obese patients, some of which had pregnancy complications, thereby greatly expanding on a previous study[62], and provides early gestation R2* values that have been very sparse in prior reports who focused on later gestation[63–66].

Placental Injury: This thesis reports on MRI findings in novel preclinical placental injury models, which have been conceived and carried out for the first time. In particular, Tisseel (Baxter Healthcare Corp) was injected in rhesus macaques in the anterior lobe of the placenta to create local placental thrombosis. Tisseel is an FDA-approved fibrin sealant used surgically to stop bleeding[67]. The infarcts caused by Tisseel could mimic biological processes that holds potential to contribute to clinical gestational complications such as fetal growth restrictions. In addition, this thesis introduces an injection of macrophage chemoattractant protein 1 (MCP1) to the rhesus placenta, with aim of inducing placental inflammation that could result in responses of modified blood flow and ferumoxytol retention.

1.3 Chapter Outline

The chapters of this dissertation are organized as follows:

Chapter 2: **Measuring Longitudinal Placental Perfusion of Zika-Infected Rhesus Macaque Placenta using VS-ASL.** A novel multi-slice velocity-selective arterial spin labeling (VS-ASL) sequence is introduced to measure placental perfusion in rhesus macaques, with 3-D whole placental coverage. Such measurement is reported through three gestational timepoints, for both healthy and zika-infected subjects.

Chapter 3: **Longitudinal Study on Early Gestation T2*-based BOLD effect in Human Placenta.** Early gestation (14 weeks, 20 weeks) baseline T2* mapping is conducted for a large human subject cohort (N=97), to assess T2*-based blood oxygen level dependent (BOLD) effect on subjects with gestational complications. Statistical results, including median T2* and pixel-wise T2* histograms, is reported.

Chapter 4: **Maternal Placental Blood Volume Measurements: Methodology and Applications.** A novel quantitative marker, maternal placental blood volume, is introduced in the context of both human and rhesus macaque subjects. First, the methodology of such measurement is discussed. Second, the feasibility of blood volume measurements in rhesus macaques is demonstrated. Third, preliminary diagnostic capabilities of blood volume measurements are assessed through wider applications, including human subjects with fetal growth restriction, and rhesus macaques with placental vascular injury.

Chapter 5: **Cotyledon-Specific Flow Evaluation of Rhesus Macaque Placental Injury using Ferumoxytol Dynamic Contrast Enhanced MRI.** Placental blood flow measurements for each placental functional unit (cotyledons) are reported on rhesus macaque subjects with placental vascular injury. An improved methodology of such measurement using dynamic feromoxytol-enhanced MRI is described. Placental blood flow is compared between different treatment groups, which results in different levels in pathology.

Chapter 6: Vasculature Assessment of Rhesus Macaque Placental Injury using Variable Flip Angle T1-Mapping and Dynamic Contrast Enhanced MRI. A pixel-wise comparison between co-registered blood volume maps, R1 maps, (discussed in chapter 4), and contrast agent arrival time maps (discussed in chapter 5) of the injured rhesus macaque placenta is reported. Potential local pathology characterized by vascular injury is demonstrated across all three maps for diagnostic fidelity.

Chapter 7: **Summary and Future Work.** A final summary on the work presented by this thesis, and potential future works to the topics discussed.

Chapter 2. Measuring Longitudinal Placental Perfusion of Zika-Infected Rhesus Macaque Placenta using VS-ASL

2.1 Introduction

Abnormal placental perfusion is associated with pregnancy complications including fetal growth restriction and preeclampsia[16,68]. Effective non-invasive assessment of placental health, particularly in early pregnancy, could be important to assist early diagnosis and intervention of placental diseases. Current gold standard vascular visualization and assessment MRI methods require the use of exogeneous contrast agent such as Gadolinium chelates that could pose safety concerns in pregnancy[69,70]. Additionally, the use of contrast agent could be timely inefficient; the amount of the contrast agent and the timing of injection and imaging could also impact the accuracy of quantitative measurement. Therefore, it might be of clinical interest to investigate a method that does not involve exogeneous contrast agent.

Arterial Spin Labeling (ASL) perfusion MRI is a compelling method to safely and non-invasively assess local perfusion without the need for an exogenous contrast agent. Instead, ASL

utilizes the magnetization difference between “labeled” and “unlabeled” blood to highlight the blood vessels. Labeling is done by using radiofrequency (RF) pulses to alter magnetization of the blood in a selected slice. This is done in the upstream of the blood flow, allowing time for the labeled blood to traverse downstream to the imaging plane in time for the imaging sequence. This time between labeling and imaging is called post label delay, or transit time. After the imaging of labeled blood, the same sequence is repeated for the unlabeled blood. The difference between the two scans would highlight just the blood vessels, making the blood an endogenous contrast agent.

However, the application of ASL perfusion MRI in the placenta poses unique challenges, including (1) motion artifacts resulting from breathing motion from both the fetus and the maternal side, and/or Braxton Hicks contractions of the uterine muscle during later stages in pregnancy, (2) variability in placental geometry and location and the tortuous nature of placental vasculature, (3) the inability to separate maternal and fetal contributions when labeling the blood ,and (4) extremely long transit times from the arteries into the intervillous space. Some commonly used ASL sequences have their unique challenges when it comes to placental imaging: FAIR (flow-sensitive alternating inversion recovery) ASL[71] is limited to single slice acquisitions, and pseudo-continuous (PC) ASL[72] is commonly used in vascular regions such as the brain but requires careful selection of tagging regions which are not conducive for placenta imaging due to the location and tortuous path of the feeding maternal arteries.

Velocity-selective (VS-ASL) MRI[44] has emerged as an alternative approach where tagging is achieved based on its velocity instead of location and its feasibility for placenta imaging has been recently demonstrated for a 3D spiral sequence[45,47]. Here we introduce a modified VS-ASL sequence that provides volumetric placenta coverage with an interleaved 2D multi-slice approach

for reduced motion sensitivity and demonstrate its feasibility across gestational stages in a non-human primate model.

2.2 Methods

Subjects: This study was approved by the University of Wisconsin-Madison College of Letters and Sciences and Vice Chancellor Office for Research and Graduate Education Institutional Animal Care and Use Committee, protocols G005401, G005691, and G005263. Six rhesus macaques were imaged up to 3 times across gestational stages as detailed in Table 2. The subjects received a Zika virus (ZIKV) injection of 10^4 (2 subjects) or 10^6 (2 subjects) plaque forming units (PFU) and the control group (2 subjects) received a saline injection. All injections occurred in amniotic fluid around gestational age of 55 days (54.7±1.9 days).

Pathology: After delivery via C-section, the placenta was analyzed for number of cotyledons and subsequently evaluated by a pathologist for abnormalities including chronic histiocytic intervillositis, acute chorioamnionitis, placental infarction, and maternal decidual vasculitis. Every cotyledon was assigned a score from zero to four based on the number of pathologies present (0 = none, 1 = one of the above, etc.). The sum of scores for every cotyledon was then divided by the total number of cotyledons in the placenta to present the average score as a summary of the overall placental health (Table 2).

MRI: Scans were acquired at 3.0 T (Discovery MR750, GE Healthcare) with a 32-channel phased array coil. The maternal monkeys were anesthetized with isoflurane, thereby effectively also eliminating all fetal body motion, and imaged in right-lateral position. Standard SSFSE images were acquired for anatomy assessment and placement of the VS ASL slices.

VS-ASL Sequence: The interleaved 2D multi-slice VS-ASL sequence, newly developed by Dr. Kevin Johnson, is shown in Figure 4. This sequence allows for a 3D whole placental coverage which could improve the accuracy of the perfusion measurements. It is characterized by a 2D SSFSE multi-slice readout with a slice interleaving scheme to avoid a slice bias based on consistent differences in the post label delays. 4 slices were imaged in each shot to balance the increase in SAR and the longer acquisition window with varying post label delays. A cool off period of 2 s was added prior to the next excitation to limit SAR.

Symmetric, adiabatic BIR-8 preparation pulses with and without flow sensitizing gradients (TI=1.2s, TR=6.6s, venc=2.4cm/s) and fat saturation pulses were used for signal preparation. R/L motion encoding was used to reduce influence from maternal respiratory motion. Scan parameters: respiratory trigger (expiration); 2D SSFSE readout (TI = 1.2 s, TE=52.2ms, matrix=256x256, in-plane spatial resolution=1.6mm^2, slice thickness 8 mm); 16 control/ tag pairs; 4 slices per shot; 2 sets of 4 interleaved slices for whole placenta coverage; scan time: ~7 min. In addition, a proton-density weighted (PDW) image without magnetization preparation was acquired in the beginning of the scan.

Processing: Offline image reconstruction and post-processing were performed using Matlab. Placental boundaries were manually segmented from PDW image using inhouse software. Voxel-wise perfusion maps were generated for all 8 slices as the median of the 16 tag-on/off difference images, normalized by PDW (equation 1). For each scan, the mean, median, and standard deviation across all data points in the placental perfusion map were calculated. The coefficient of variation is calculated as a ratio between mean and standard deviation. These values were also assessed for the central slice only.

Equation 1. perfusion (p) shown as a ratio percentage of tag on/off difference over PDW.

$$p = \frac{|S(tag_{on}) - S(tag_{off})|}{M_0}$$

Table 2. Information on the pregnant rhesus macaques.

Subject #	ZIKV Infection	# of Cotyledons	Pathology Score	Gestational Age at MRI [days]	Mean Perfusion [mL/100g-min]	Median Perfusion [mL/100g-min]	Coefficient of Variation
1	10^4 PFU	18	0.93	-/-/145	-/-/1506	-/-/1152	-/-/0.855
2	10^4 PFU	23	0.6	-/100/148	-/593/1022	-/465/916	-/0.849/0.550
3	10^6 PFU	9	0.3	68/106/146	631/1191/1349	583/1128/1234	0.531/0.495/0.488
4	10^6 PFU	22	0.69	65/100/145	301/598/419.2	205/520/333	1.05/0.708/0.879
5	control	15	0.08	66/100/145	487/672/587	427/564/491	0.719/0.735/0.776
6	control	10	0.09	-/-/146	-/-/400.2	-/-/315	-/-/0.954

The subjects received an ZIKV injection of 10^4 or 10^6 plaque forming units (PFU) and the control group received a saline injection. The number of perfusion domains was established after C-section. The pathology score reflects tissue analysis of individual cotyledons. MRI was performed at up to 3 time points during gestation ('- 'indicates no scan performed; full term for rhesus macaque = 166 days) and mean, median, and coefficient of variation for the VSL ASL analysis are reported for those scans.

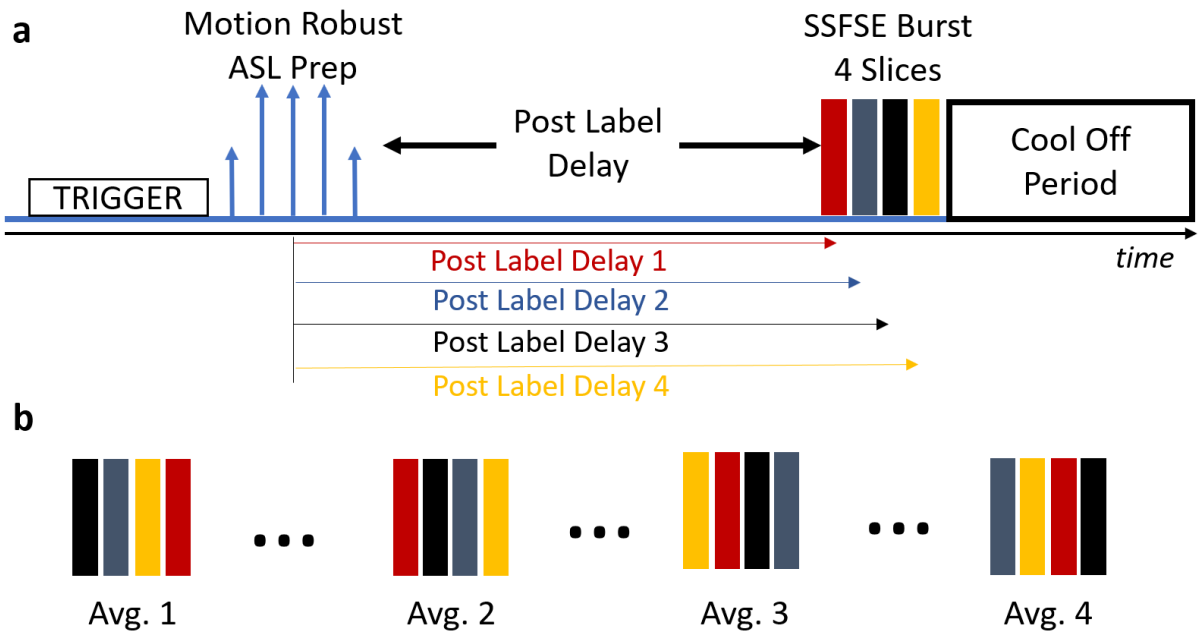

Figure 4. Interleaved multi-slice VS-ASL sequence paradigm shown for 4 slices. Image Courtesy of Dr. Kevin Johnson.

The sequence timing diagram (not drawn to scale) shows how the respiratory trigger (expiration) initiates the motion robust VS-ASL prep module followed by a post label delay (TI: ~1.2 s) and

subsequent rapid acquisition of 4 SSFSE slices and a cool off period. A total of 16 tag-on / tag-off pairs are acquired and averaged for improved SNR. (b) The slice order is cycled to mitigate signal differences from the different post label delays differences, effectively averaging these effects.

2.3 Results

Perfusion maps were successfully obtained for all 13 scans. Zika injections have been shown to result in modest pathology for all subjects; however, a pathology score has been assigned to each subject. All control subjects had pathology scores close to 0, whereas the Zika-infected subjects had pathology scores ranging from 0.3 to 0.93. Tissue analysis by the pathologist also showed an increased number of cotyledons with Zika-treated subjects.

Table 2 shows mean perfusion, median perfusion, and coefficient of variation of each scan. The four Zika-treated subjects (subject 1-4) have mean perfusion of 1056 ml/100g-min, 1022 ml/100g-min, 1349 ml/100g-min, and 419.2 ml/100g-min, respectively. In comparison, the two control subjects, with mean perfusion of 587 ml/100g-min and 400.2 ml/100g-min, have a slightly lower perfusion.

Figure 5 shows perfusion maps of six consecutives anterior (A) to posterior (F) slices for rhesus macaque #6 (control subject) on gestational day 146. The VS-ASL perfusion map (in heat map color scale) is calculated as a ratio between “tag on” and “tag off” signal intensities. The “hot spots”, or areas in yellow, indicate regions with higher perfusion. These regions exhibit special variations from slice to slice. The perfusion maps are overlaid on top of the anatomical proton density image for better spatial visualization.

Figure 6 shows a scatter plot between median VS-ASL perfusion and gestational age. Interestingly, the Zika-infected (ZIKV) group has seemingly higher perfusion that increases with gestation, whereas the control group has fairly constant perfusion throughout gestation.

Table 3 shows the median perfusion using all placenta voxels and central slice voxels only. The last column demonstrates the percent difference between the two median perfusion values. The highest absolute difference is 89%, for subject #4 (Zika-treated) at gestation day 65. In general, the percent difference is lower for higher gestation, and higher for the Zika-treated group, comparing to the control subjects (#5, #6).

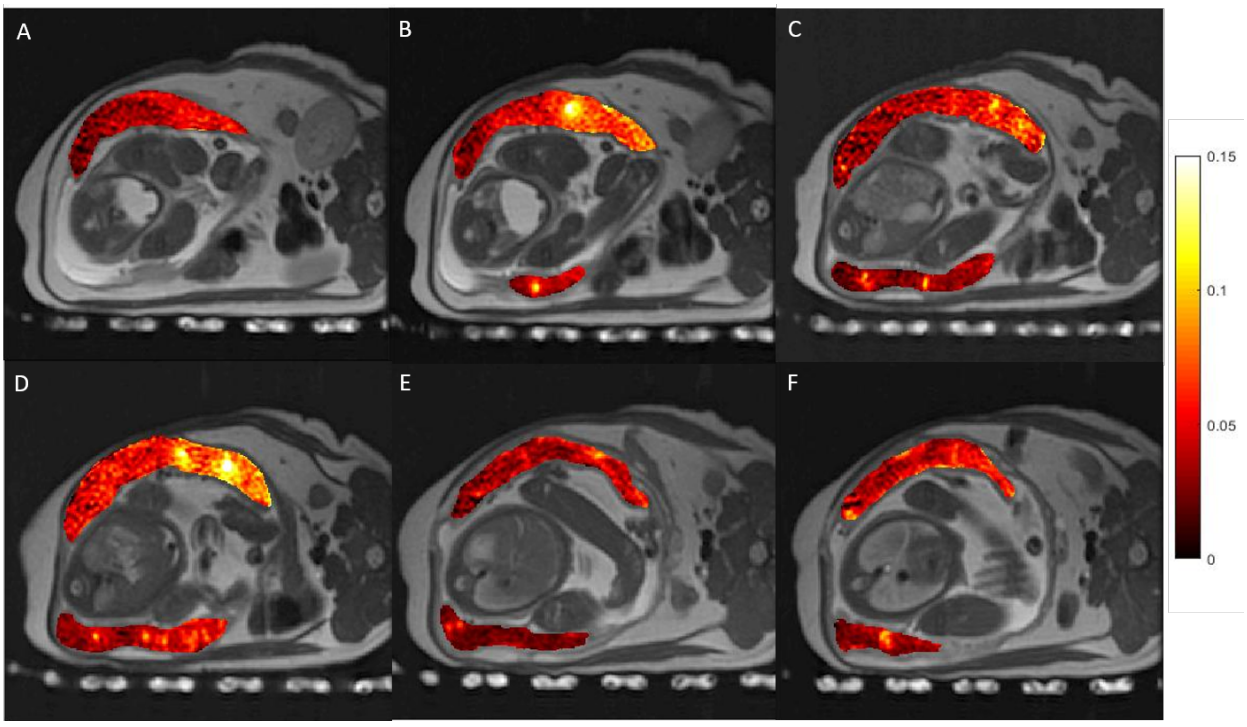

Figure 5. Perfusion map of six consecutives anterior (A) to posterior (F) slices of a control subject.

The VS-ASL perfusion maps were calculated as ratio percentage map and overlaid on top of the proton density image. Note the spatial variations in the VS-ASL signal, indicating the need for whole placenta assessment for a robust perfusion assessment.

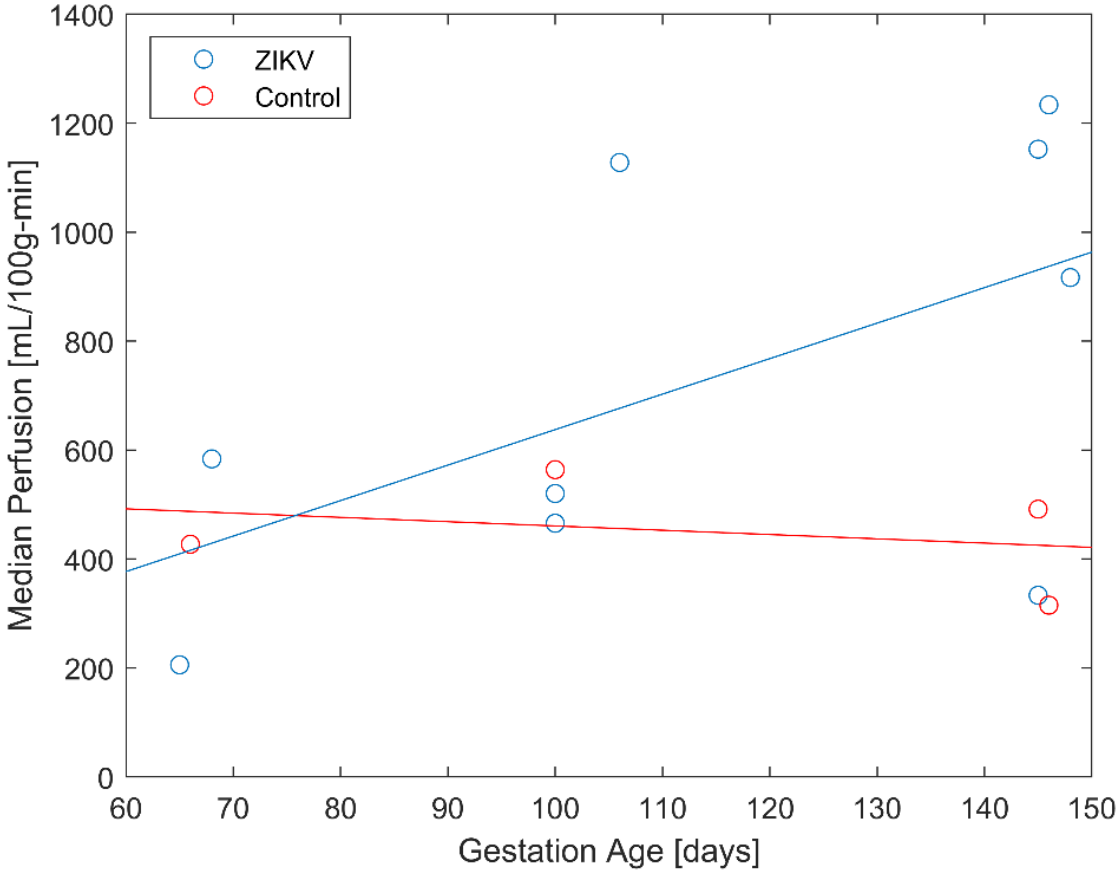

Figure 6. Median VS ASL perfusion as a function of gestation age.

The linear fitting shows possible perfusion differences between Zika-treated group (ZIKV) and control groups, but more samples are required for a thorough statistical analysis.

Table 3. Comparison of the VS ASL median perfusion measures obtained from the central slice and whole placenta.

Rhesus Macaque #	Gestational Age at MRI [days]	Overall Median Perfusion [mL/100g-min]	Central Slice Median Perfusion [mL/100g-min]	% Difference
1	145	1152	1724	49.6
2	100	466	260	-44.3
2	148	917	1245	35.8
3	68	584	540	-7.4
3	106	1128	740	-34.7
3	146	1234	1148	-7.0
4	65	206	389	89.0
4	100	520	311	-40.3
4	145	333	258	-22.8
5	66	427	336	-21.3
5	100	564	422	-25.2
5	145	492	525	6.9
6	146	315	327	3.7

Data shown across all subjects and all gestational timepoints of imaging. The difference between two perfusion values from central slice vs. all slices suggests importance of whole-placenta coverage for VS-ASL perfusion measurements.

2.4 Discussion and Conclusion

This preliminary study demonstrates the technical feasibility of 2D multi-slice VS-ASL with whole placental coverage. To our knowledge, this is the first study that reports non-human primate perfusion measurements using a multi-slice VS-ASL sequence. There are several innovative aspects for this imaging method comparing to existing studies[45,47,71]: First, the rotating of slice order for SSFSE images effectively averages out the difference between post labeling delay

times. Second, the 2 sets of 4 interleaved slices mitigates the effect of signal crosstalk between neighboring slices. Last, this preliminary study allows for further application of such technique in measuring whole-placental perfusion in human subjects[73].

Differences in pathology score, number of cotyledons, and perfusion changes over gestational age were observed between subjects injected with Zika-infected subjects and controls, but more data are needed to allow for thorough statistical testing. In general, the Zika treatment in this study resulted in modest pathology, as no fetal anomalies or infection were detected[74].

Visual inspection and the difference in mean perfusion measures between the central slice and whole placenta in some subjects demonstrate the need for volumetric placenta analysis, especially in cases of local placental mal-perfusion. In addition, the regional heterogeneities of placental perfusion exhibited in most slices agrees with the study from Hutter et al[75], which demonstrated potential link between perfusion heterogeneities and deposition of fibrin.

There are several limitations of our study. First, since this is a feasibility study, the number of subjects is limited for conducting a more thorough statistical analysis on the effect of Zika injection on changes in perfusion, both on a global and local level. Second, the modest pathology resulting from the Zika infection could hinder the effectiveness for a statistical result, even with a larger subject group. Third, the relatively large slice thickness (8mm) and long acquisition times mean that maternal and/or fetal motion could potentially influence the perfusion measurement.

Although there are many positive and innovative aspects with a multi-slice 2D VS-ASL sequence, it should be noted that there are a few considerations of VS-ASL in placental imaging that require careful adjustments for future studies. First, some scan parameter settings, such as cutoff velocity, velocity encoding direction, and post labeling delay, could influence the placental

perfusion measurements. This was demonstrated by Harteveld et al[76]. Second, the perfusion results with VS-ASL contains both maternal and fetal contributions since all areas of selected velocity is tagged. This could result in confounding factors while interpreting the results, especially if only manipulation of maternal blood flow is applied. In contrast, PC ASL[72] offers perfusion measurement from maternal-only contributions, since the tagging can occur on an upstream plane consists of only maternal uterine artery. Our current results that showed potential differences between zika vs control could be further corroborated by a repeatability study of our protocol, and could serve as a future direction of this study.

In conclusion, this preliminary study demonstrated the feasibility of whole-placental perfusion measurements using a novel 2D multi-slice VS-ASL sequence. Future studies include clinical translation with human subjects and assessing the early gestation predictabilities of placental pathology through rhesus macaques with placental injury.

Chapter 3. Longitudinal Study on Early Gestation T2*-based BOLD effect in Human Placenta

3.1 Introduction

The placenta is a crucial organ that facilitates in fetal growth and nutrient exchange between the mother and the fetus during pregnancy. The health and development of placental vasculature are closely linked with pregnancy complications and outcomes; insufficient oxygen and nutrient exchange could lead to fetal growth restrictions (FGR), preeclampsia, and pre-term birth[21,77]. Maternal obesity (characterized as BMI>30) has been shown to potentially increase the risk of placental vascularity malfunction, which could lead to gestational complications[21]. Therefore, proper screening of this high-risk group at early gestation could be very valuable to early discovery and intervention of potential gestational complications currently not possible.

T2* is a quantitative MRI marker which reflects paramagnetic deoxyhemoglobin concentration. A lower value in placental baseline T2* suggests placental hypoxia, which could lead to oxygen exchange deficiency[78]. Therefore, many studies over the years have investigated the correlations between baseline T2* and potential gestational complications and delivery outcomes[63,65,66,79–97]. Lower values of base T2* of the placenta has been shown to correlate with fetal congenital heart disease[98], fetal growth restrictions[29,30], preeclampsia[99], lower fetal weight[100], and other primary and secondary adverse pregnancy outcomes. Additionally, several studies investigated potential diagnostic efficacy using multi-modal imaging combining T2* and uterine artery Doppler ultrasound[64,101], intravoxel incoherent motion[102], susceptibility-weighted MRI[103], T1[104,105], perfusion[106], and diffusion[107,108]. Lastly, potential variables during image acquisition[109],

patient positioning[110], and pre-labor uterine contractions[110–112] that could impact the accuracy of T2* were analyzed by previous studies as well.

Although various pregnancy complications have been investigated through scans in later stages of pregnancy, there are few documentations of early gestational (namely gestation age of less than 20 weeks) time point T2* values with a relatively large cohort, potentially due to the lack of symptoms or representations of disease characteristics. Analysis of early pregnancy placental T2* value could allow early prediction of placental pathology, thus increasing the time window available for intervention or treatments. This study provides in-vivo baseline T2* measurements at 14 weeks and 20 weeks to assess their predictability of gestational complications. In addition, this study investigates baseline placental T2* differences for subjects with maternal obesity.

3.2 Methods

Subjects: This study is approved by the institutional review board (IRB). 98 pregnant women participated in this study. 25 subjects have body mass index (BMI) of over 30 kg/m^2 (33.5 ± 2.74 kg/m^2) and are considered obese for this study. The non-obese (N=72) group has BMI of 23.8 ± 2.55 kg/m^2. All subjects went through up to two scans at gestation ages of 14 and 20 weeks.

Data Collection: MRI scans were acquired on a wide-bore 1.5T MRI scanner (Optima MR 450w, GE Healthcare) with a 48-channel phased-array coil. Subjects were imaged in supine position. A 3D multi-echo spoiled gradient echo (flip angle=9°, TR=43.0 ms, initial TE = 1.5 ms, number of TEs = 16, ΔTE = 2.6 ms, FOV = 42*38*14 cm^3, resolution = 2.2*2.0*3.0 mm^3, scan time = 5:27 mins) sequence with respiratory gating was used for the scans.

Data reconstruction and analysis: Water and T2* maps of each scan were reconstructed through IDEAL processing using monoexponential fit of complex echo images. Both water and T2* maps were evaluated in OsiriX (Pixmeo SARL, Switzerland) by a radiologist of over 10 years of clinical experience. Image quality of both maps was determined on a 5-point Likert scale based on motion, noise, and overall quality. A score from 3 to 5 in overall quality of both maps is considered of diagnostic quality; scans with a score of 1 or 2 is considered clinically unacceptable, and therefore excluded from data analysis. Semi-automated placental segmentation was done through ITK-SNAP[113] based on water maps and evaluated by a radiologist. In addition, a single circular muscle ROI (~3cm^2) in gluteus region were drawn for 10 of the subjects without complication and scanned for both gestational time points. A flowchart summary of data selection is shown in Figure 7.

Data analysis: Mean, median, standard deviation, and histogram distribution of pixel-wise T2* values were generated using the T2* maps. ΔT2* was calculated as difference between mean placental T2* for each subject imaged at both 14 and 20 weeks of gestation. For each gestational time point, mean placental T2* values of obese and non-obese subjects were compared using paired t-tests. Sum-of-T2* is calculated as the sum of all pixel-wise T2* values across all placental areas. To assess reproducibility of scans, muscle ROI for week 14 and week 20 were compared for variation using paired t-tests.

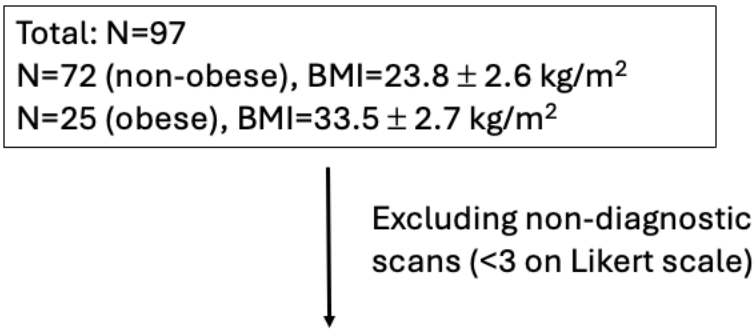

	N (Total)	N (Obese)	N (Non-Obese)
14 Weeks	79	62	17
20 Weeks	72	55	17

Figure 7. Data selection for this study.

Each subject went through up to two scans at gestation ages of 14 and 20 weeks.

3.3 Results

Of all the subjects included with our analysis, 44 had normal gestational outcomes, 4 had gestational hypertension, 2 had preeclampsia, and 3 had preterm birth. T2* maps for all subjects included in the analysis were successfully generated. Mean 14-week and 20-week T2* for all normal pregnancies are 121 ms and 124 ms, respectively. Figure 8 shows anatomical image (water map) and T2* map for one control subject at 14 and 20 weeks of pregnancy.

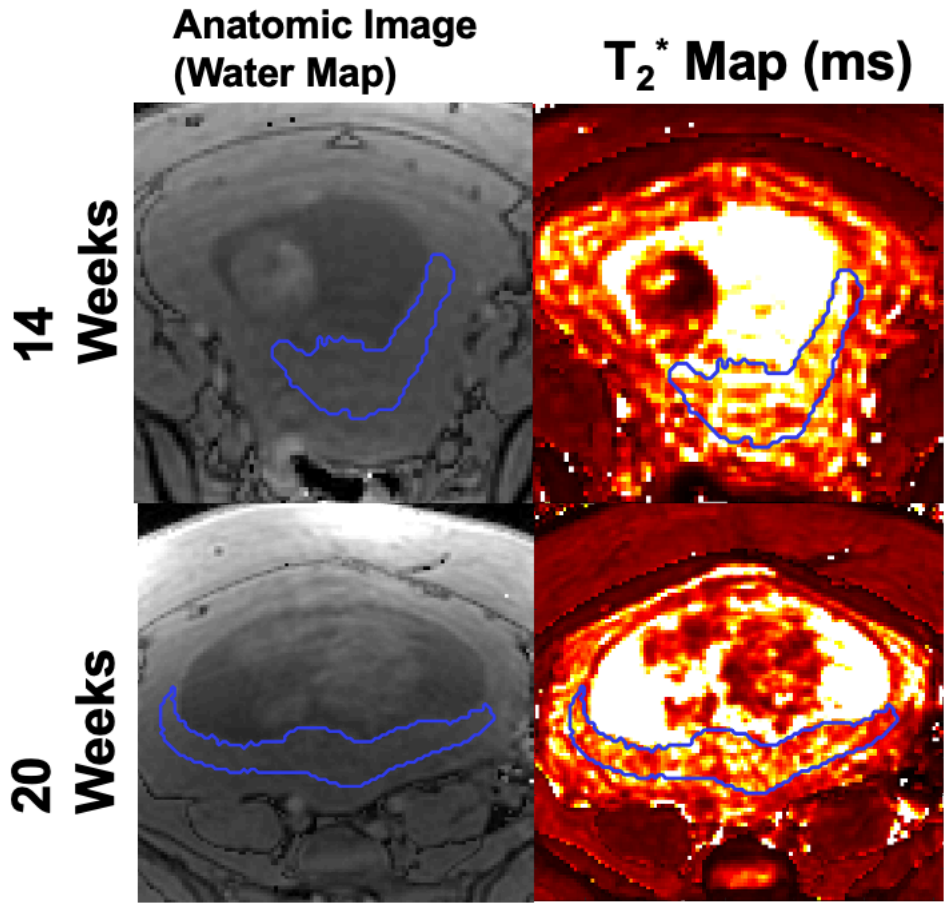

Figure 8. Anatomic image (water map) and T2* map for a control subject at 14 and 20 weeks of pregnancy. Image courtesy of Dr. Ante Zhu.

Figure 9 shows 14-week, 20-week, and difference between 20- and 14-week median T2* (ΔT2*) values for the non-obese and obese groups, with T2* of subjects with abnormal gestation outcomes overlaid on top of the box-and-whisker plots. The non-obese subjects have a trend of increased T2* with increased gestation age; the obese subjects show the opposite trend. However, there are no statistically significant differences in the T2* values between non-obese and obese subjects or from 14 to 20 weeks within these groups. Median T2* values indexed by pregnancy complications and obese vs non-obese are shown in Table 4.

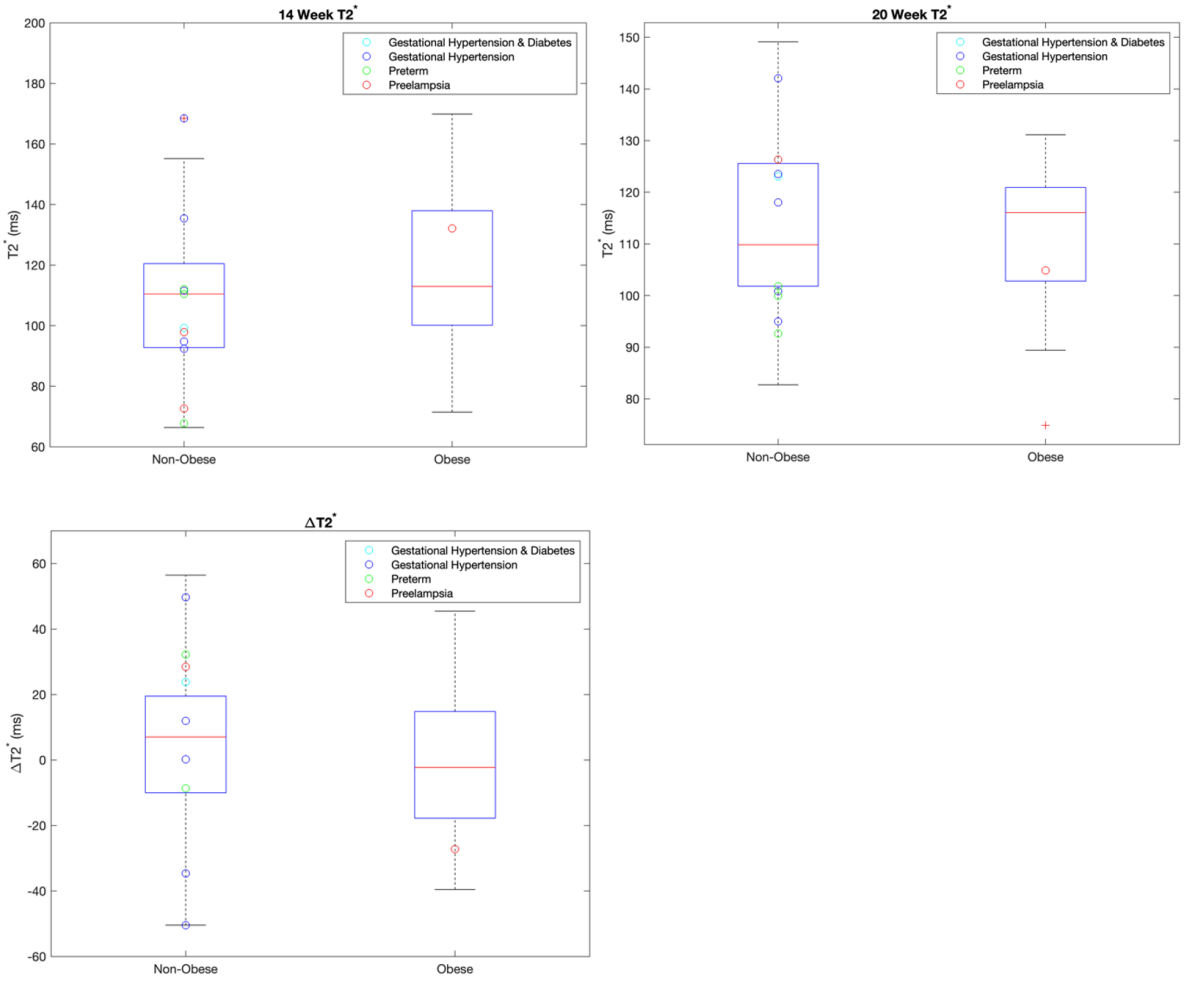

Figure 9. Box-and-whisker plots of 14-week, 20-week, and Δ T2* values, with the T2* values of abnormal gestational outcome overlaid on top.

A trend of increased T2* with gestation age is observed for non-obese subjects. However, there are no significant differences in the T2* values for the two groups.

Table 4. T2* values (mean and standard deviation) for all obese and non-obese subjects, and subjects with various gestation outcomes.

Subjects	14 Weeks T2* (ms)	20 Weeks T2* (ms)
All Non-Obese (N=68)	100 ± 20.4	106 ± 15.2
All Obese (N=20)	108 ± 24.8	103 ± 13.4
Normal Pregnancy (N=68)	102 ± 22.1	105 ± 15.5
Gestational Hypertension & Diabetes (N=1)	94.9	114
Gestational Hypertension (N=10)	106 ± 20.3	106 ± 11.1
Gestational Diabetes (N=3)	105 ± 21.2	97.5
Preterm (N=3)	93 ± 23.3	91.4 ±7.74
Preeclampsia (N=3)	96 ± 26.8	109 ± 14.5

Figure 10 shows the averaged T2* histogram representation for each group of pregnancy complications along with uncomplicated obesity groups. The histograms show notable differences in shape: at 14 weeks, the histogram for subjects with hypertension and preterm birth has similar shape than normal but lower counts; preeclampsia is characterized by a shift to lower T2* values and a less symmetric shape; hypertension and gestational diabetes has a higher and sharper peak. At 20 weeks, the overall counts are increased, reflecting growth of the placenta. Patients with hypertension and preeclampsia show lower counts than controls; patients with hypertension and gestational diabetes show much lower counts; and patients that delivered preterm show a slightly steeper histogram shape that is shifted towards lower T2* values.

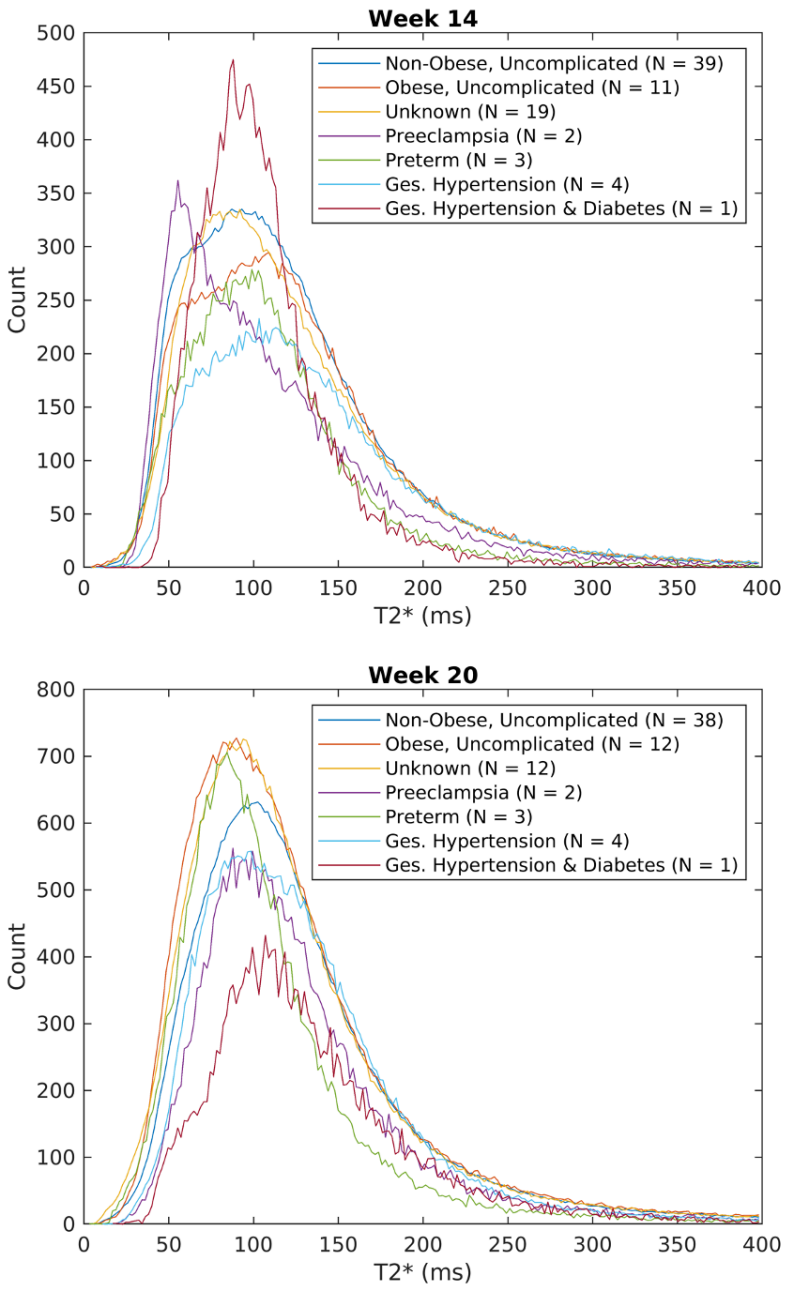

Figure 10. Averaged histograms of pixel-wise placental T2* values for week 14 and week 20 grouped by pregnancy complications.

Here, 'control' means no reported pregnancy complications or outcomes and incudes obese and non-obese subjects.

Figure 11 shows median T2* and placenta volume for week 14 and week 20 as a function of birthweight. T2* values alone are not predictive of birth weight outcomes at the early gestation window; however, some subjects with pregnancy complications are associated with relatively lower placental volume. Muscle measurements in the 10 subjects (Table 5) show no statistically significant variation between 14-week and 20-week gestation, suggesting the repeatability of our protocol.

Table 5. T2* values in muscle ROI for 10 subjects at 14- and 20-week gestation.

Subject #	14-Week Muscle T2* [ms]	20-Week Muscle T2* [ms]	ΔT2* [ms]
1	29.4	27.8	-1.6
2	32.3	31.3	-1
3	28.6	29.4	0.8
4	31.3	30.3	-1
5	29.4	30.3	0.9
6	31.3	30.3	-1
7	28.6	28.6	0
8	29.4	27.8	-1.6
9	28.6	29.4	0.8
10	29.4	27.8	-1.6

3.4 Discussion

This study reported 14-week and 20-week placental T2* of obese and non-obese subjects, along with subjects with gestational complications. A non-significant trend of increased T2* with gestation was observed for the group without complications; this agrees with a preliminary study of 6 subjects done by our group.[114]

Our analysis shows median T2* values alone were not significantly different between subjects with and without adverse events or different between non-obese and obese subjects at early gestation ages. Overall, our T2* values for 1.5T were slightly lower (~125 ms) than reported by Sorenson at 1.5T (~150ms)[7]. This could be due to the different echo times used to obtain the images used for T2* fitting.

Subjects with certain gestational complications were associated with low placental volume; however, the number of determined pathological cases in our cohort is too small to provide more in-depth statistical analysis and prior studies have shown limited value in placental volume as a predictor for pregnancy complications.

There are a few limitations of our study. The maternal and/or fetal motion during the scans has caused a number of scans to be excluded from our analysis, thus limiting our potential data volume. The discontinuation of the study for several subjects, especially those with adverse pregnancy outcomes, decreased our number of data points for a conclusive statistical analysis. Additionally, only up to two gestational timepoints were imaged per subject, which limited a regression analysis of T2* with respect to gestational age. Lastly, although we tested for repeatability of our scanning protocol using muscle ROIs, we did not conduct a multi-center study to assess the robustness of our methods off-site.

The differences in T2* histograms between pregnancies with no reported complications and those with complications are intriguing and resemble findings by Schabel et al.[115], which inspired this analysis. Further investigation using radiomics analysis with more subjects is needed to identify shape descriptors that can predict pregnancy complications and, possibly, improve patient care by early therapeutical interventions. As this study shows, large number of subjects

need to be prospectively enrolled to image the few patients early in pregnancy who will later develop complications. Hence, multi-center studies would be likely needed.

Acknowledgements

We gratefully acknowledge GE Healthcare for research support of UW-Madison, and funding support from NIH U01-HD087216, NIH R01 HD103443, UW-Madison Dept. of Radiology R&D Fund, and UW-Madison Dept. of Obstetrics and Gynecology R&D Fund.

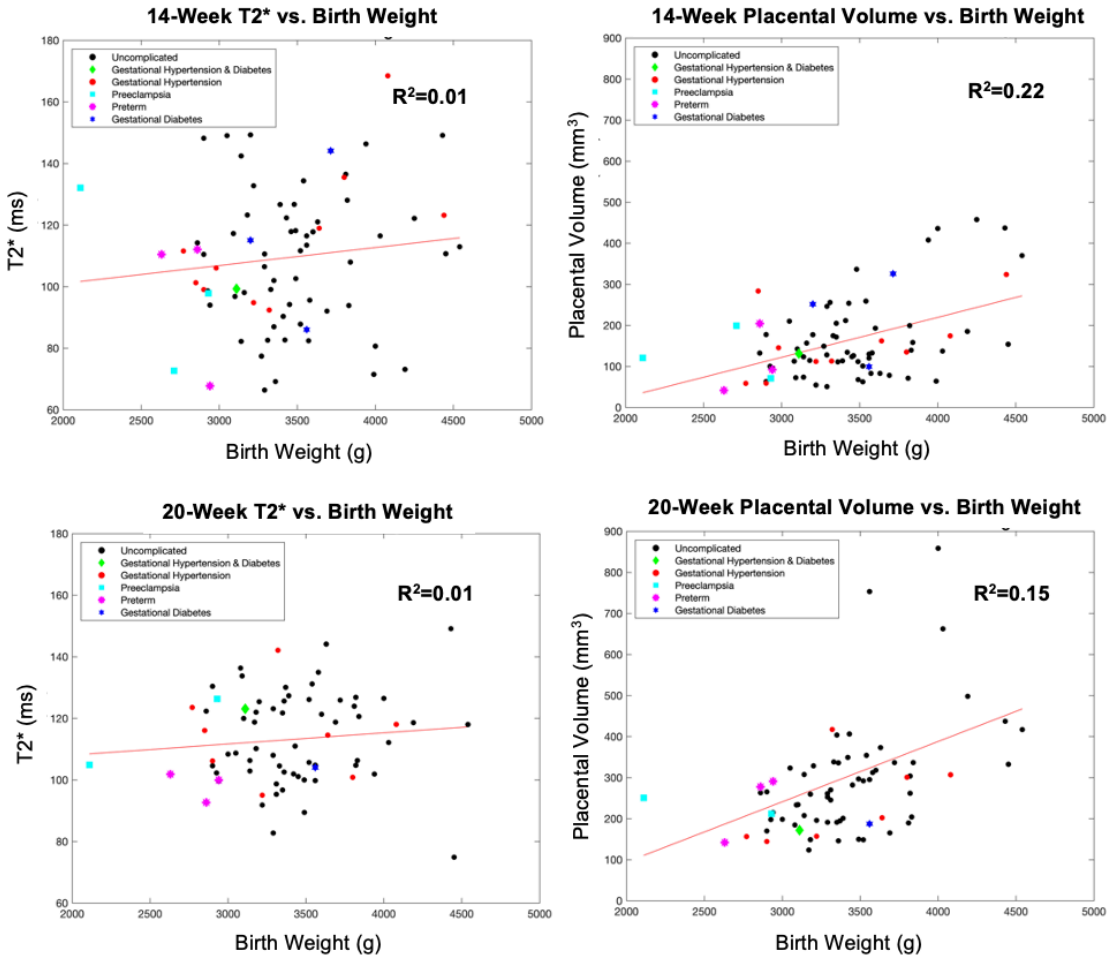

Figure 11. Plots of median T2* and birth weight vs birthweight (column 1) and placental volume vs birth weight (column 2).

Certain gestation complications are associated with lower birth weight and low placental volume; more subjects are needed to perform more in-depth statistical analysis.

Chapter 4. Maternal Placental Blood Volume Measurements: Methodology and Applications

4.1 Introduction

The development of utero-placental vasculature plays a critical role in placental health and fetal growth. Abnormal adaptation of placental vasculature to fetal demands can lead to malperfusion and gestational complications such as fetal growth restriction and preeclampsia [27,68,116]. Therefore, there are potential benefits to accurately tracking and quantifying placenta vascular development throughout the multiple stages of gestation, including early gestation where there is a potential window for interventions and treatments.

Clinically, ultrasound is widely used for in vivo imaging in pregnancy. The advantages of ultrasound include cost-effectiveness, accessibility, and faster imaging time. However, ultrasound also has limitations in assessing placental vascular health including relatively unreliable measurements of macroscopic placental blood flow because of vessel tortuosity and lack of relevant quantitative imaging markers[23]. Alternatively, MRI provides a framework to quantify vascular function and health through measures of macrovascular blood flow[3], global and local perfusion[4], oxygenation[5], and inflammation[6] of organs including the brain, heart, liver, and kidneys. Recent advances in placental MRI have enabled the assessment of various quantitative markers such as placental perfusion[24], blood oxygenation level dependent (BOLD) effects[25], native R2*/T2* quantification[8], and direct blood flow measures[26]. These quantitative metrics provide unique depictions of placental health; however, they are often confounded by placental anatomy and physiology. For example, T2* relaxometry is sensitive to oxygenation, vessel architecture, and to the presence of iron and calcium. Further, vascular metrics from non-contrast perfusion

MRI using arterial spin labeling (ASL) can be limited by the long transit time in the intervillous space and unique architecture of the spiral arteries, leading to underestimation of the placental perfusion [24].

Placenta-related fetal growth restriction (FGR) is associated with mal-perfusion of the placental tissue, which originates from insufficient development of utero-placental vasculature[13]. Measurements of maternal placental blood volume could potentially detect local ischemia and poorly developed placental vasculature, thus providing insight on placental health and fetal development. Recently, studies have demonstrated maternal placental blood volume measurements in pregnant mice and rhesus macaques using variable flip angle T1 mapping. However, to our knowledge, no such studies have been performed in humans, in part due to the lack of suitable contrast agents for pregnant subjects.

Contrast-enhanced MRI is a non-invasive tool that holds the potential to add diagnostic information regarding placental intervillous flow and perfusion. Clinically, dynamic imaging of intravenously injected Gadolinium based agents is routinely used to derive blood flow and blood volume measures across multiples organs. While Gadolinium (Gd) has been used in pregnant non-human primate experimental models [48], and a pilot study in human pregnancy (n=6)[49], concerns about its teratogenic potential and confirmation that it can be transported across the placenta to the fetal compartment [50] as well as its unknown safety for the fetal compartment limit its potential for diagnostic application [70]. Ferumoxytol, a superparamagnetic iron oxide nanoparticle approved for the clinical treatment of anemia, is a compelling off-label intravascular contrast agent that is increasingly used for MRI [51–54] with regional T1 and T2* shortening, and a long intravascular residency time (~14.5 hrs). Ferumoxytol has been shown to be well tolerated, associated with no serious adverse events, and implicated in few (1.8% mild and 0.2% moderate) adverse reactions

in a multi-center MRI safety study of 4240 subjects stretching over 15 years[55]. Preliminary studies have also suggested no detectable risk for non-human primates [117] and demonstrated use in patients [118]. Ferumoxytol is used in MRI studies as an off-label contrast agent and has been shown to have good safety profiles when used for pulmonary angiograms in pregnant patients[119].

Current guidelines require ferumoxytol to be injected slowly, which limits its ability to quantify blood flow, but its intravascular nature is ideal to provide measures of placental blood volume through gestation. Recently, Badachhape et al. estimated fractional blood volume (FBV) in pregnant mice from images acquired before and after contrast injection of intravascular liposomal gadolinium-based contrast agents (GABA) to assess maternal-side placental perfusion and found good agreement with nanoparticle contrast-enhanced computed tomography (CE-CT) [58]. Such blood volume measures can possibly identify placental perfusion deficits that are indicative of local ischemia or fetal growth restriction (FGR). Recently, pilot studies for such blood volume measurements have been demonstrated in healthy mice[58] and rhesus macaque models[120], as well as in human placentas with fetal growth restriction[121]. However, the link between blood volume measurements and pathology, such as thrombosis, has not been established.

This work seeks to establish a post-processing workflow to measure ferumoxytol based maternal placental blood volume in humans and non-human rhesus macaques through VFA T1-mapping. The first application of this work is to perform ferumoxytol-based maternal placental blood volume measurements in Zika virus-infected and control rhesus macaques [74] at various gestational timepoints. The second application of this work is applying the same blood volume technique to three human subjects diagnosed with late-gestation FGR. Lastly, this work will assess the diagnostic potential of blood volume measurements for rhesus macaque subjects with placental injury from Tisseel injections.

4.2 Variable Flip Angle (VFA) T1-Mapping

Blood volume mapping was based on T1 mapping before and after the injection of ferumoxytol. T1 mapping was performed with a respiratory-gated center out, 3D radial, variable flip angle (VFA) spoiled gradient echo (SPGR) sequence[122], with flip angles of 2°, 6°, 10°, 14°. Figure 12 (top) shows a naïve SPGR signal (a.u.) with variable flip angles, with the four points corresponding to the four flip angles used in our technique. This signal can be expressed with equation 2; note that the T2* component can be minimized here due to the short TE.

Equation 2. SPGR signal.

$$S = M_0 \cdot \frac{\sin(\alpha) \cdot \left(1 - e^{-\frac{TR}{T_1}}\right)}{1 - e^{-\frac{TR}{T_1}} \cos(\alpha)} e^{-\frac{TE}{T_{2*}}}$$

Figure 12 (bottom) shows that equation 2 can be rearranged to a linear relationship between $\frac{S}{\sin(\alpha)}$ and $\frac{S}{\tan(\alpha)}$. This is also expressed by equation 3, with $e^{-\frac{TR}{T_1}}$ as the slope of the fitting. By using four VFA angles, we could obtain $T_1 = -TR/\ln(m)$ with potentially higher accuracy and stability of the linear fitting than using less VFA angles. This T1 calculation is done on a per-voxel basis to obtain a 3D T1 map.

Equation 3. Rearranged SPGR signal showing linear relationship.

$$\frac{S}{\sin(\alpha)} = e^{-\frac{TR}{T_1}} \frac{S}{\tan(\alpha)} + M_0(1 - e^{-\frac{TR}{T_1}})e^{-\frac{TE}{T_{2*}}}$$

B1+ inhomogeneities were accounted for by using respiratory-gated B1+ maps, which were re-sampled using bi-linear interpolation to match the dimension of the images. All fitting was performed in an in-house tool written in C++ written by Dr. Kevin Johnson. Fitting was performed

in the complex domain with mean square error minimization between the predicted signal and the measurement data.

4.3 Blood Volume Calculation

Maternal placental blood volumes were estimated using the pre- and post-contrast R1 (1/T1) maps generated by variable flip angle fitting. ΔR1 maps were obtained by pixel-wise subtraction of the two registered R1 maps pixel-wise. Three quantitative blood volume measurements were derived:

(1) maternal fractional blood volume (mFBV), which is the fractional amount of placental volume occupied by maternal blood, calculated as the ratio between median ΔR1 in placenta and maternal blood.

Equation 4. Maternal fractional blood volume.

$$mFBV = \frac{\Delta R1_{placenta}}{\Delta R1_{vessel}}$$

Regional mFBV maps were calculated as the ratio of pixel-wise ΔR1 in placenta and median $\Delta R1$ of blood. Placental regions containing mFBV value of 1 suggests 100% blood content (or 0% tissue) in that region.

(2) Maternal placental blood volume (mPBV), which is the total blood volume (in milliliters) in the placenta due to maternal contribution. This is calculated as placental volume, V_{placenta}, multiplied by mean mFBV.

Equation 5. Maternal placental blood volume.

$$mPBV = FBV \times V_{placenta}$$

(3) Total maternal blood volume (mTBV), which is the total blood volume (in milliliters) in the rhesus macaque animals, not counting the fetal blood. This is calculated as a ratio of

amount of ferumoxytol (mol) in placental tissue over concentration of ferumoxyol (M) in blood $C_{b_{total}}$.

Equation 6. Concentration (C) of ferumoxytol in blood.

$$C_{b_{total}} = \frac{\Delta R1_{blood}}{r_1}$$

Equation 7. Total maternal blood volume.

$$mTBV = \frac{m_{FE} \times m_{rhesus}}{M_{FE} \times C_{b_{total}}}$$

We assume a fast-exchange limit of a two-compartment water exchange model since the water protons diffuse quickly across the vessel walls due to the highly permeable nature of the placenta[123]. Therefore, a linear relationship between Ferumoxytol concentration and relaxivity (r_1=8.6725$s^{-1}mM^{-1}$)[124] is assumed.

A paired T-test was used to determine statistical significance in blood volume measurements between controls and Zika-infected rhesus macaques.

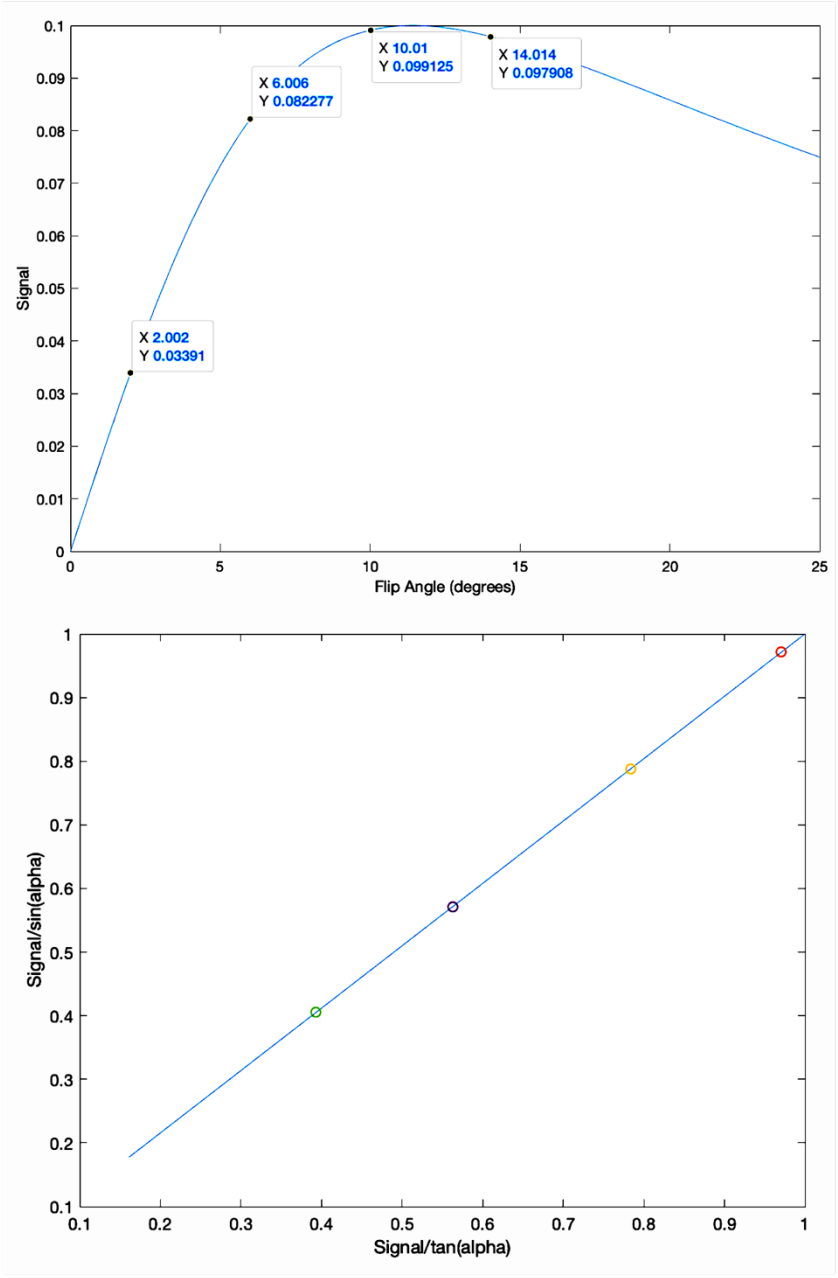

Figure 12. Sample SPGR signal and its relationship with flip angles.

4.4 Application 1: Longitudinal Placental Blood Volume Measurements in Zika-Infected Rhesus Macaques using Ferumoxytol-Enhanced MRI

4.4.1 Methods

Animals: This prospective animal study was approved by our institution's animal care and use committee. Seven pregnant rhesus macaques (maternal body weight 8.20±1.35 kg) were imaged longitudinally at up to 3 timepoints across gestation (days 64.5±1.9, 100.8±3.9, and 145.3±1.8), corresponding to first, second, and third trimester of the rhesus, which has gestation days of 146~180 full term. Three animals received a Zika virus (ZIKV) injection into the amniotic fluid of 10^4 plaque forming units (PFU) and one animal received 10^5 PFU. Three control rhesus macaques received a saline injection. All injections occurred at gestational age 54.7±1.9 days. Prior to imaging, sedation was completed by injection of up to 10 mg/kg ketamine, followed by intubation and maintenance anesthesia by inhalation of a mixture of oxygen and 1.5% isoflurane.

MRI Data Acquisition: All scans were performed on a 3.0 T MRI system (Discovery 750, GE Healthcare, Waukesha, WI, USA) using a 32-channel torso coil (Neocoil, Pewaukee, WI, USA) with the animal in the right lateral decubitus position. Scanning was performed with a respiratory-gated center out, 3D radial, variable flip angle (VFA) spoiled gradient echo (SPGR) sequence[122] (TR = 6.0 ms, TE = 1.2 ms, imaging FOV = 200 x 200 mm^2, BW = 125 kHz, scan time = 8 min 46 sec). After pre-contrast imaging, Ferumoxytol (4mg/kg with respect to maternal body weight, diluted 5:1 with saline) was intravenously administered with a power injector. Approximately 30 minutes later, the T1 mapping sequence was repeated with identical parameters. Separate to VFA imaging, a vendor supplied 2D Bloch-Siegert sequence was used to perform B1+ mapping. This B1+ map covered the imaging volume of interest contiguously. This workflow is illustrated by Figure 13.

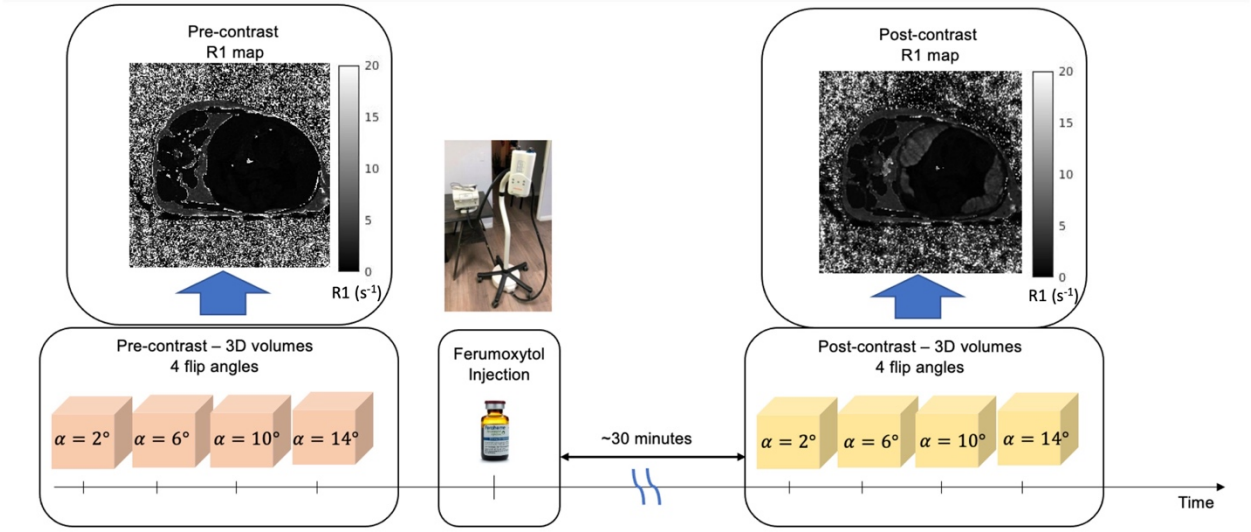

Figure 13. Variable flip angle R1 mapping protocol for Ferumoxytol MRI in rhesus.

R1 mapping was performed with a respiratory-gated center out, 3D radial variable flip angle T1 weighted spoiled gradient echo sequence. After pre-contrast image acquisition, ferumoxytol was intravenously administered at 4mg/kg with a power injector. The same T1 mapping sequence was performed approximately 30 minutes after contrast injection. R1 (1/T1) maps were obtained using an in-house toolbox for complex fitting to spoiled gradient echo signals.

Image Registration and Segmentation: To minimize effects from maternal and fetal motion on blood volume estimates, registration of the pre- and post-contrast R1 maps was performed based on the $\alpha = 6°$ T1-weighted scans. Fully automated registration using Advanced Normalization Tools (ANTs) [125] was performed using user-defined symmetric normalization (SyN), including affine followed with deformable transformation, with mutual information as optimization metric. Each registration metric uses a 3-level image pyramid with each level 200 iterations at most. The result of the registration is then applied as a matrix transform to all the other flip angles, prior to R1 fitting. Placental segmentations were conducted manually on the heavily T1-weighted 14° flip angle post-contrast images using an inhouse segmentation tool (MATLAB). In addition, a circular ROI was drawn on the uterine artery to measure R1 values in blood. Figure 14 shows a sample placenta and vessel ROI segmentation.

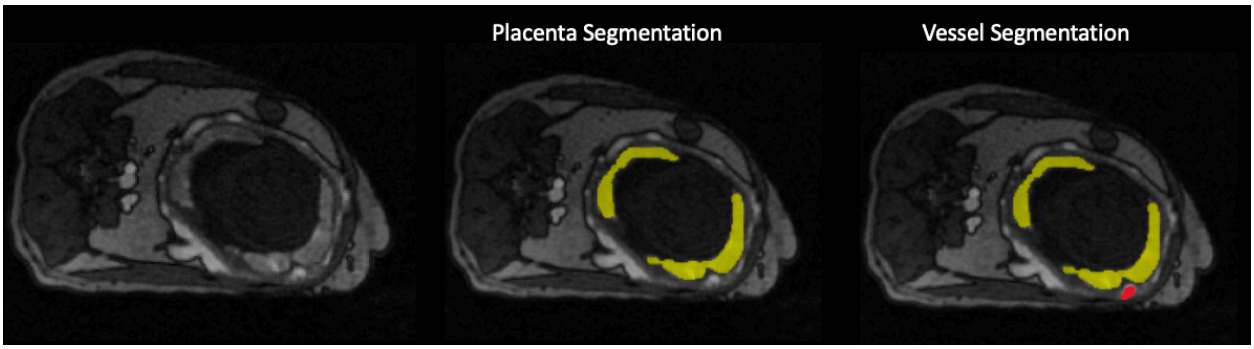

Figure 14. Sample placenta (yellow) and vessel ROI (red) segmentation.

4.4.2 Results

Measurements of R1 values and blood volume measures for each scan were successfully achieved. Figure 15 shows pre- and post-contrast anatomical T1-weighted scans (left to right: 2°, 6°, 10°, 14°) of a control animal (#3), as well as the corresponding R1 maps on the right. The ZIKV infection model in this study has previously been determined, via histopathological analysis, to have very modest placental pathology in a related study. Average maternal fractional blood volume (mFBV) values across animals were 0.33 ± 0.05, 0.38 ± 0.06, and 0.40 ± 0.06 for gestational time points (GTPs) 1, 2, and 3 respectively.

Figure 16 shows 6 non-consecutive slices of mFBV (values are color-coded with heat map fashion) of the same animal as that of Figure 15, overlaid on top of T1-weighted SPGR anatomical images imaged with flip angle of 14°. mFBV range from 0 to 1, with 1 meaning the region has 100% blood (such as it being a blood vessel). mFBV exhibits a regionally heterogeneous distribution both across slices and within each slice. The white arrows indicate regions with high blood volume, which could correspond to spiral artery inflow zones of the placenta.

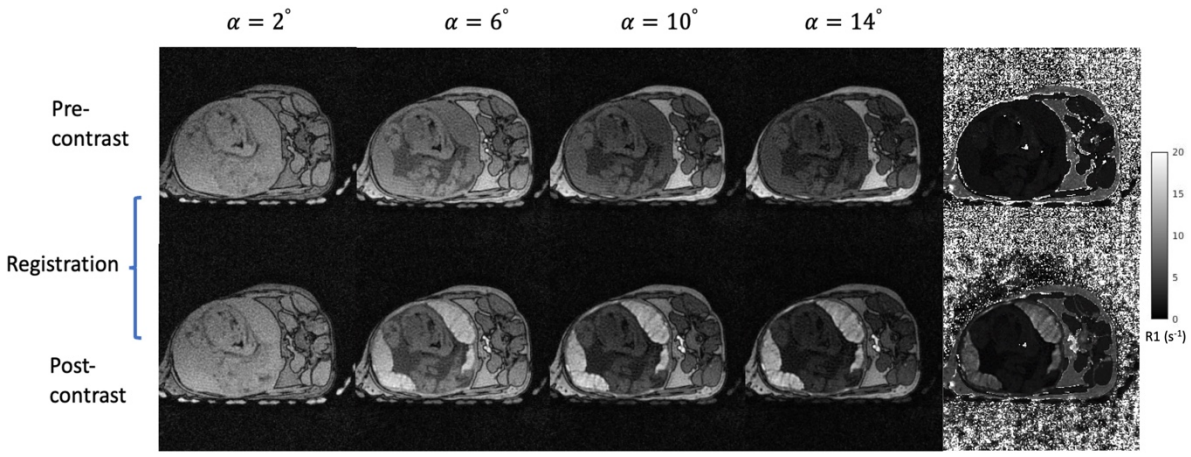

Figure 15. Variable flip angle images.

Left four columns show Pre- and post-contrast (top and bottom) T1-weighted anatomical images at each flip angle (left to right: 2°, 6°, 10°, 14°) of control animal #3. The R1 fitting result is shown on the right. Pre- and post- contrast T1-weighted images were registered using affine then non-rigid registration.

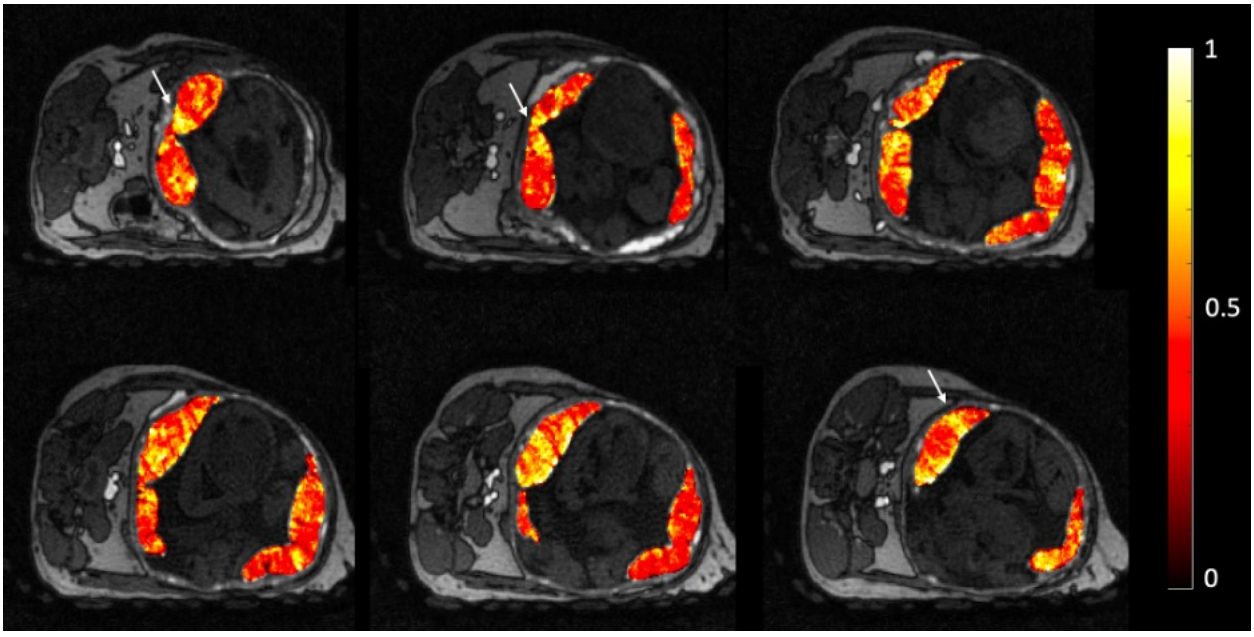

Figure 16. Representative fractional blood volume maps.

Six selected slices (out of ~150 slices covering the placenta) of maternal fractional blood volume maps are overlaid on top of the corresponding anatomical T1-weighted images (animal # 2, gestation day = 146). A value of 1 indicated a region that contains 100% blood. The mean mFBV of this scan is 0.48. The maternal fractional blood volume exhibits a regionally heterogeneous distribution (for example, the white arrows point towards regions with high blood volume), which indicates local perfusion variations.

Table 6 shows mFBV, mPBV, and $\Delta R1_{blood}$ values for each animal at each gestation time point scanned. Mean mFBV values increase slightly with gestational ages. mPBV value is 11.1±5.0 ml, 19.2±4.0 ml, and 39.4±9.7 ml for GTPs 1, 2, and 3 respectively. mPBV increases consistantly with gestation age; mFBV also increases with gestation age but the increase is more modest.

Table 6. Rhesus blood volume measurement results.

Subject #	Ges. Age (Day)	mFBV	$\Delta R1_{blood}$ (s^{-1})	mPBV (ml)
1	66	0.39	7.1	13.2
1	102	0.44	3.9	22.0
1	142	0.41	6.1	40.5
2	100	0.44	5.3	25.5
2	145	0.48	6.2	58.5
3	62	0.32	11.1	10.0
3	97	0.34	8.7	15.6
3	146	0.35	8.6	33.4
4	63	0.37	11.4	9.2
4	95	0.45	3.0	18.7
4	145	0.45	6.7	33.4
5	64	0.33	6.6	6.7
5	100	0.31	4.1	19.8
5	148	0.32	10.9	34.8
6	67	0.25	13.2	6.9
6	106	0.33	9.4	13.5
7	106	0.41	6.1	19.0
7	146	0.39	5.4	35.8

This table shows maternal fractional blood volume (mFBV), maternal placental blood volume (mPBV), and pre- and post-contrast R1 difference in blood vessels ($\Delta R1_{blood}$) values for each animal at each gestation time point scanned.

Figure 17 shows median mFBV and mPBV measurements for all animals across gestation ages. Statistical analyses show no significant differences in mFBV between controls and zika-

infected rhesus macaques, which corresponds to our finding of modest placental pathology from zika virus. Figure 18 shows histograms of maternal fractional blood volume, ΔR1 in placenta, and ΔR1 in blood averaged over the 4 animals imaged for all three gestational time points. Median TBV across all scans is 740.3 ml, and median TBV normalized by maternal body weight is 93.4 ml/kg.

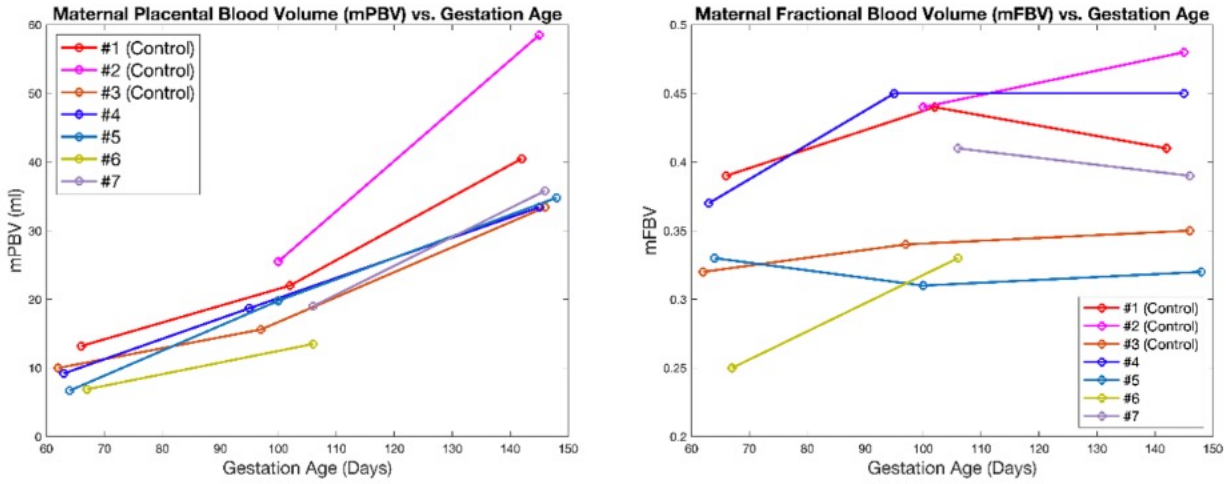

Figure 17. Longitudinal plots of maternal placental blood volume.

This shows consistent increase in blood volume with respect to gestation age. The maternal fractional blood volumes show a more heterogeneous distribution: most animals tend to have an increase in mean blood volume with gestation, whereas two animals show decrease in blood volume from the second to the third gestational timepoint. Note that the zika infection in this study resulted in very modest pathology difference, which is supported by our data showing no significant difference in blood volume between the two treatment groups.

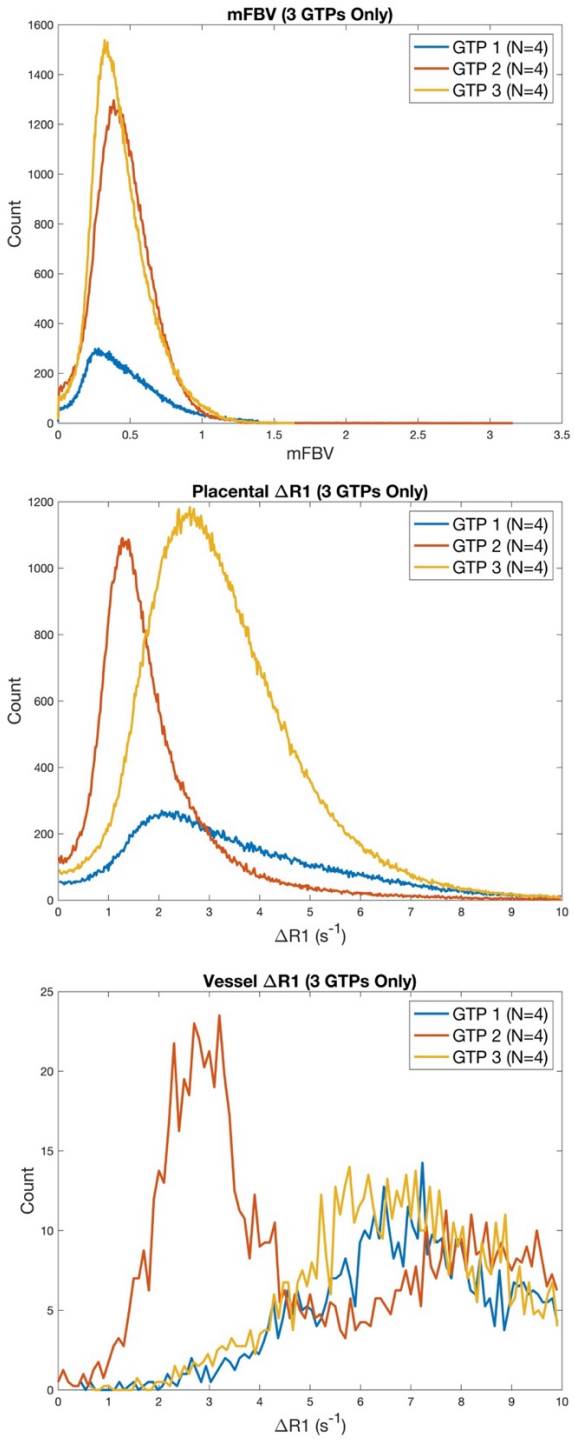

Figure 18. Pixel-wise blood volume histograms.

This shows (top to bottom) maternal fractional blood volume, ΔR1 in placenta, and ΔR1 in blood averaged over all animals imaged for all three gestational time points (GTPs).

4.4.3 Discussion

This preliminary study demonstrated the possibility of quantitatively measuring maternal placental blood volume using ferumoxytol enhanced MRI. This study also successfully measures rhesus macaque placental regional blood volumes in-vivo, with direct application to human gestation.

Ferumoxytol increased R1 relaxivity in both placental tissue and in blood vessels, but no enhancement in signal was observed quantitatively or visually in fetal tissue. This agrees with previous study in humans that were limited to visually evaluated images[126]. This continues to provide additional evidence supporting the used of ferumoxytol given that it does not cross the maternal-fetal barrier. This in contrast to current Gd based agents, which do pass to fetus in trace amounts. However, this also means that ferumoxytol blood volume measures only represent maternal blood volume and these measures do not inform on potential abnormalities in the fetal circulation. Although clinical literature suggests maternal blood-flow deficit in common pregnancy disorders, studies are needed to verify the utility of maternal only blood volume measures using contrast enhanced MRI in identifying pathology.

The mean mFBV across all animals increased with gestation age, although each animal showed slightly different trends individually. This slight increase agrees with the findings by Badachhape et al. in a pregnant mouse model[58]. This suggests possible advances in placental vascular development with gestation. Mean mPBV also showed significant increases with gestation age for all animals, especially from the second to third trimester gestational time point. This is largely due to the overall growth in the placenta volume over gestation, coupled with the slight increase in mFBV.

The mean TBV measured in this study from all scans is 50.4% higher than previous TBV measurement in non-pregnant adult rhesus macaques of 62.1 ml/kg using an indicator dilution methodology[127]. This is within the expected range of normal percent of blood volume increase during human pregnancy[128]. However, some of the observed TBV variations are not physiological plausible. Our TBV measures are dependent on precise knowledge of the amount of ferumoxytol injected and assumes an exact dose of ferumoxytol is delivered to the animal. Errors in dosing may proportionately propagate to errors in dosing given. Animals in this study received a bolus delivery of ferumoytol for dynamic contrast enhanced (DCE) MRI [117]. We suspect that imperfect mixing with saline, incomplete injections solution in line, or extravasation might have occurred in some instances and corrupted TBV estimates. Such situations are avoidable in pharmacy-prepared larger volumes generally used in slow infusion treatments in human investigations, but with the limitations associated with slow infusion rather than concentrated rapid bolus injections.

Local analysis of mFBV showed a heterogeneous distribution of high blood volume zones (~100% FBV), which could correspond to inflow vascular regions for placental functional units. The histogram analysis shows higher skewness for both mFBV and $\Delta R1$ for the first time point. This could be due to less concentrated central perfusion regions at early gestation[9]. We see a left shift in ΔR1 values for both placental and blood regions in the second gestational time point, which could be due to imperfect contrast injection, since our power injector was normally used for larger volume and higher concentration injections for humans. However, this effect is does not affect our mFBV measurements since they do not require prior knowledge of the amount of contrast injected.

There are a few limitations of our study. Maternal and fetal motion during scan can result in motion artifact and imperfect registration between pre- and post-contrast images. Since our animals were sedated for the scans, fetal motion was the main issue since it warps the placental

shapes. This occurs more often at higher gestational ages. One animal (#8) was excluded from analysis due to significant fetal motion during the time between pre- and post-contrast scans. Additionally, the limited number of animals and scan timepoints limits the extent of statistical analysis of our data. Lastly, the ZIKV infection model has previously been shown to have very modest placental pathology in a related study[74]. The modest pathological outcomes of the placentas may result in small blood volume value differences between the control animals and the Zika-infected animals, which then could not serve as a direct indication of clinical detectability of pathology using blood volume measurements.

The use of ferumoxytol contrast agent and a non-human primate model provides insight on the translational potential of in-vivo blood volume measurements. Future work includes blood volume measurements on Rhesus animals with induced pathology (e.g. regional placental infarction) to directly visualize pathology detectability. Additionally, the clinical use of Ferumoxytol allows for quantitative blood volume measurement and analysis on humans with fetal growth restrictions.

Acknowledgements

We gratefully acknowledge funding R01 HD103443, R21 AI129308, U01 HD087216, T32 HD041921 from the NIH. We thank GE Healthcare for research support of UW-Madison, and AMAG Pharmaceuticals for providing ferumoxytol used in our imaging procedures. We also thank the Wisconsin National Primate Research Center (WNPRC) Veterinary, Scientific Protocol Implementation, and Animal Services staff for providing animal care, and assisting in procedures including breeding, pregnancy monitoring, and sample collection.

4.5 Application 2: Maternal Placental Blood Volume Measurement of Human Placenta with Fetal Growth Restriction

4.5.1 Methods

In this IRB approved study and with FDA-IND in place, three human subjects (maternal age = 34, 35, 41y; weight = 95 kg, 73 kg, 91 kg; GA = 35w2d, 35w0d, 34w2d) diagnosed with fetal growth restriction were imaged after providing informed consent. 255 mg Ferumoxytol (corresponding to 2.7, 3.5, and 2.8 mg/kg respectively) was diluted in 50 ml saline for an intravenous infusion administered over 30 mins followed by subsequent resting period, all with maternal and fetal monitoring in the obstetrics triage unit. MRI data (scan 1) were collected 3-4 hours later. The MRI protocol was repeated (scan 2) 3-5 days later, at which ferumoxytol was assumed to have cleared the placenta based on preclinical data6.

MRI scans were acquired on a wide-bore 1.5T MRI scanner (Optima MR 450w, GE Healthcare) with a 48-channel phased-array coil with subjects in supine position. T1 mapping was performed with a respiratory-gated center out, 3D radial, variable flip angle T1-weighted spoiled gradient echo sequence (TR = 4.0 ms, TE = 0.2 ms, imaging volume = 360x360x360 mm3, spatial resolution = 1.41x1.41x1.41 mm3, 4 flip angles = 2°, 6°, 10°, 15°, total scan time = 8 min).

R1 maps were generated for each scan session using pixel-wise complex fitting to SPGR signals through an inhouse toolbox in MATLAB (Mathworks, Natick, MA). Scan 2 was treated as a baseline scan after washout of the Ferumoxytol. Non-rigid registration was performed between each of the four flip angle scans, as well as scan sessions 1 and 2. Placental segmentations were conducted manually on the heavily T1-weighted 15° flip angle post-contrast images using ITK-SNAP. In addition, a circular ROI was drawn on a vascular region near the placenta to measure R1 values in blood.

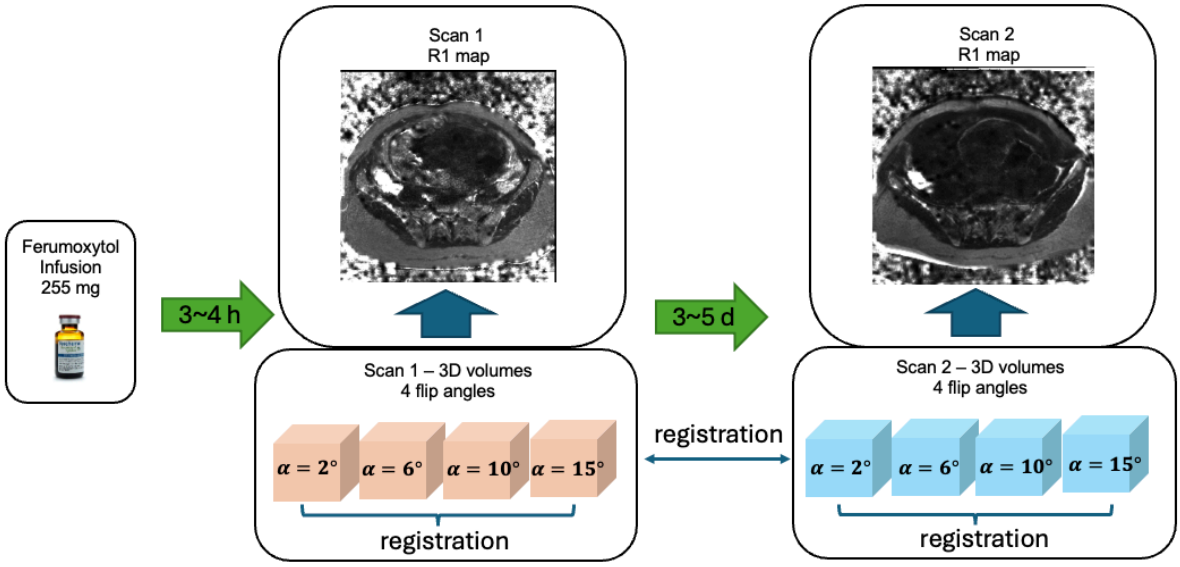

Figure 19. Image acquisition workflow for this study.

4.5.2 Results

Figure 20 shows T1-weighted anatomical images used for segmentation, and the R1 maps corresponding to the same slice position. The images show signal enhancement of post-contrast anatomical images and R1 maps. The yellow arrows point to some of the vessel regions used for ROI delineation.

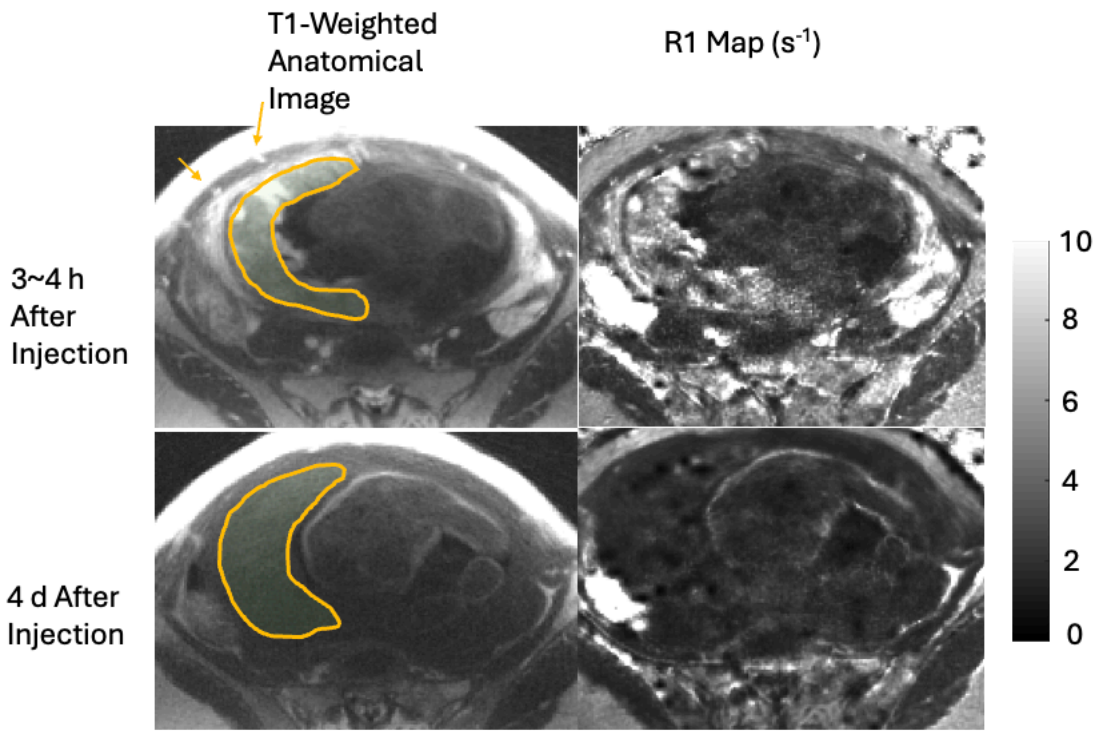

Figure 20. T1-weighted anatomical image (flip angle = 15°) used for segmentation and R1 map for corresponding slice position.

Scan 1 (top row; obtained 3~4 h after contrast administration) and scan 2 (bottom row; obtained 4 d after contrast administration) are co-registered to mitigate effects of maternal & fetal motion, as well as subject positioning difference for the two scans. A significant enhancement in placental region is shown in both images of scan 1.

Figure 21 shows 3 slices of contrast-enhanced T1-weighted images for each subject. Clear vascular and placental (delineated with orange boundaries) signal enhancement was observed. For quantitative comparison, Table 7 shows mean placental R1 and blood volume measurements for all subjects.

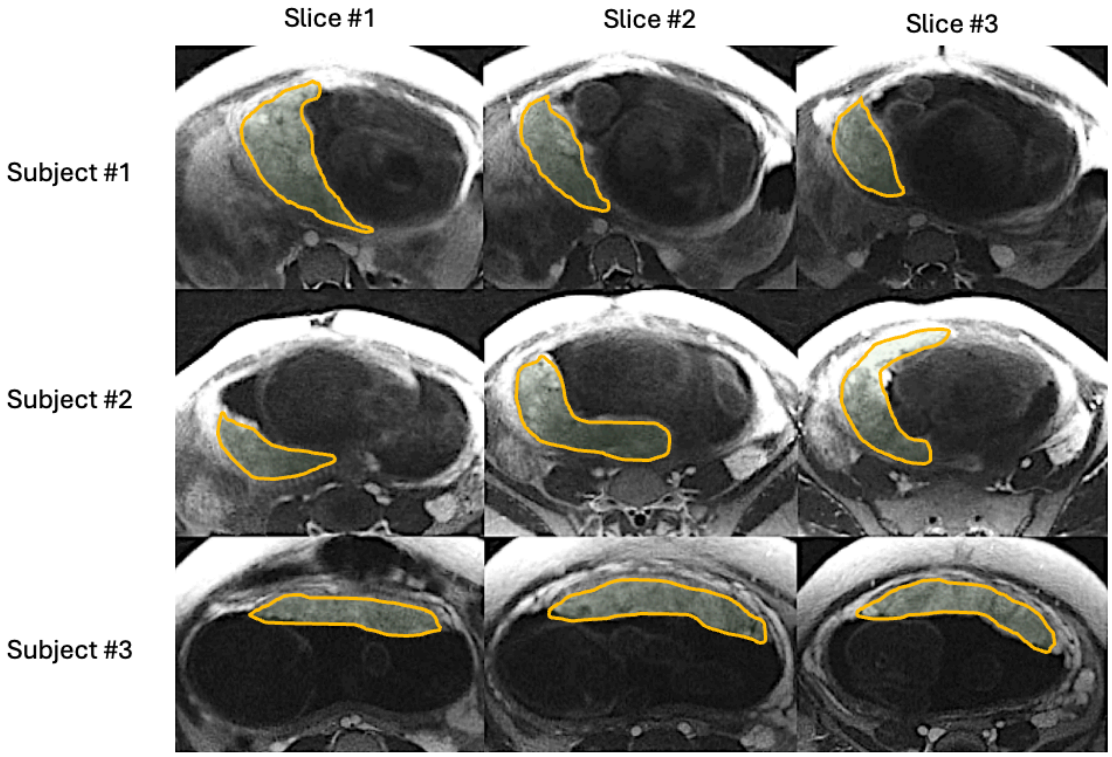

Figure 21. Three non-consecutive slices (left to right) of contrast-enhanced T1-weighted anatomical images (flip angle = 15°) for each subject (top to bottom) used for segmentation. Slice location selected differ for each subject.

Table 7. Mean values for scans 1 and 2 and maternal blood volume measurements for all three subjects.

Subject	3~4 h Post-Injection R1 (s^{-1})	3-5 days Post-Injection R1 (s^{-1})	ΔR1 (s^{-1})	mFBV	mPBV (ml)	mTBV (L)
1	2.95	1.78	1.17	0.15	98.6	5.14
2	2.58	1.19	1.38	0.22	151.6	6.35
3	4.04	0.85	3.20	0.44	347.5	5.51

Maternal fractional blood volume (mFBV) indicates the percent amount of placental volume occupied by maternal blood. Maternal placental blood volume (mPBV) is the total amount of maternal blood (in ml) in placenta.

Figure 22 shows eight slices in which the FBV map (heat map) is overlaid on top of the T1-weighted anatomical images of subject #2. Regional heterogeneities of the FBV values can be observed within each slice; for example, the white arrows show regions with low FBV values, which could indicate local mal-perfusion in the placenta. Lastly, Figure 23 shows histograms of all pixel-wise mFBVs and ΔR1 values in the placenta for each subject. Subject 3 was observed to have higher mFBV and higher ΔR1 than the other two subjects.

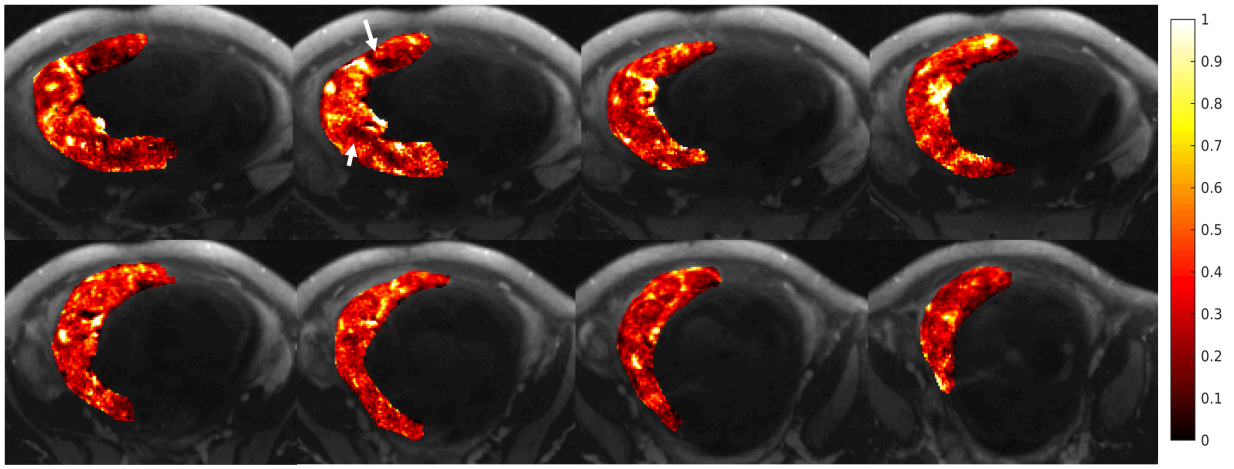

Figure 22. Eight slices (non-consecutive) showing maternal fractional blood volume (mFBV) distribution (heat map) overlaid on top of the T1-weighted anatomical images.

mFBV ranges from 0 to 1, with 1 being 100% blood in certain placental regions. mFBV exhibits regional heterogeneity; white arrows indicated regions with low blood volume, which could indicate local placental pathology.

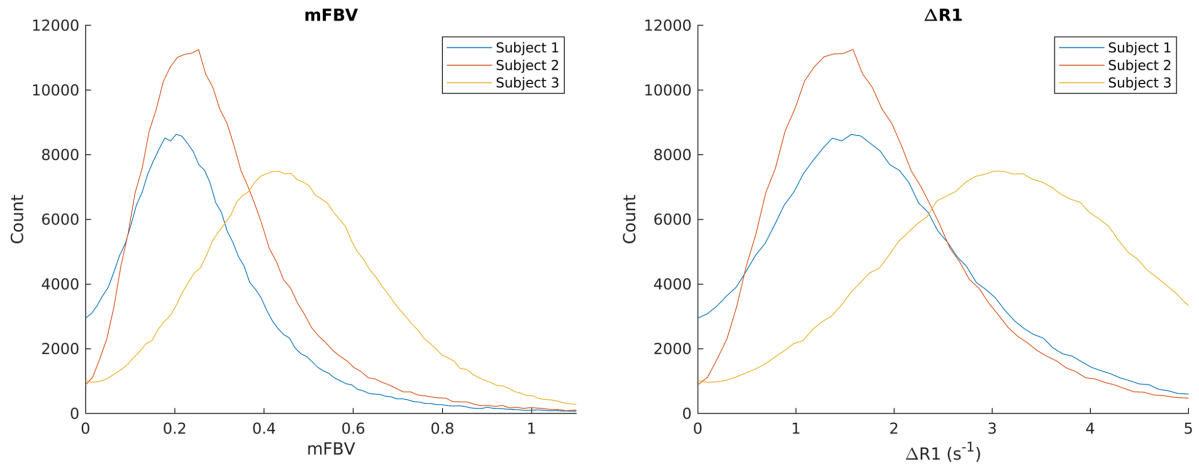

Figure 23. Maternal fractional blood volume (mFBV) and *Δ*R1 histograms for each subject.

Note that the highest mFBV is larger than 1 because FBV is calculated as each pixel of placental ΔR1 over mean ΔR1 of blood. ΔR1 is calculated as pixel-wise subtraction of the two R1 maps fitted using scan set 1 (3~4 h after contrast injection) and scan set 2 (3~5 d after contrast injection).

4.5.3 Discussion

This pilot study demonstrates the feasibility of quantitative assessment of human maternal placental blood volumes from maternal contributions using ferumoxytol as a contrast agent. To our knowledge, this is the first study to report such measurements in human subjects. Maternal total blood volume (mTBV) for the three subjects were measured to be 5.1L, 6.4L, and 5.5L respectively; this is in line with an approximately 45% increase of maternal blood volume during pregnancy[129]. Local analysis of mFBV demonstrated a heterogeneous distribution that includes high blood volume zones (~100% mFBV), which could correspond to inflow vascular regions for placental functional units. Low mFBV zones were also identified to reflect potential pathology. Substantial fetal motion and Braxton-Hicks contractions were observed during some scans, necessitating the need of deformable registration not only between scans but also across different flip angles within the 8 min VFA scan. A limitation of the study is that the contrast infusion outside

the bore prohibits the acquisition of a well co-registered pre-contrast baseline R1 map. Additionally, this could impact the baseline (without contrast) scan accuracy depending on the effectiveness of ferumoxytol washout between two scan times. Future studies of interest include comparisons with normal subjects, regional comparisons with pathology, and imaging across multiple gestation timepoints to assess sensitivity for early detection of placental perfusion abnormalities and related pregnancy complications such as FGR.

Acknowledgements

We gratefully acknowledge GE Healthcare for research support of UW-Madison, and funding support from NIH U01-HD087216, NIH R01 HD103443, UW-Madison Dept. of Radiology R&D Fund, and UW-Madison Dept. of Obstetrics and Gynecology R&D Fund. Ferumoxytol for the study was donated by AMAG Corp., MA after NIH funds were awarded.

4.6 Application 3: Maternal Placental Blood Volume Measurement of Rhesus Macaques with Placental Injury

4.6.1 Methods

Animals: Six rhesus macaques went through three longitudinal scans at around days 100, 115, and 145 of gestation. One day after the first imaging date, three of the subjects received a 0.5ml Tisseel injection into the anterior lobe of the placenta, and the other three received a saline injection as controls. Tisseel (Baxter Healthcare Corp) is an FDA-approved fibrin sealant used surgically to control bleeding[67]. We hypothesized its injection would create blood clots within cotyledons in the placenta, thereby mimicking vascular infarcts. Histopathological analysis was performed on the placentas following cesarean section delivery at gestation day 155.

Imaging: All subjects were sedated with isoflurane prior to imaging. The scans were acquired on a 3.0 T system (Discovery MR750, GE Healthcare) with a 32-channel phased array coil. The subjects were imaged in right-lateral position. A respiratory-gated center out, 3D radial spoiled gradient echo sequence (TR=6.0ms, TE=1.2ms, scan time=525.9s, BW=125kHz, spatial resolution=0.87×0.87×1.00mm3) covering the entire placenta was performed at four different flip angles (2°, 6°, 10°, 14°). The same protocol was performed 30 minutes after intravenous ferumoxytol (4mg/kg) infusion. Figure 13 from chapter 4.4.1 demonstrates the imaging workflow. Following delivery, each placenta was evaluated by a pathologist of over 15 years of experience.

4.6.2 Results

Two out of three Tisseel-treated subjects had only a single disc of the placenta; all other subjects had the rhesus typical two placental discs. Figure 24 shows longitudinal measures of mean FBV for each subject. All control subjects have a trend of increasing FBV with gestation, whereas the Tisseel-treated subjects have a relatively constant trend through gestation.

A wide range of pathology was detected for each subject, including the controls; however, one Tisseel-treated placenta in particular (rh3014) was inferred from pathology seen upon histologically analysis to have significant ischemia that multifocally affects large portions of several cotyledons. Post-delivery histopathological analysis (not shown here) of a center cut of cotyledon B in rh3014 shows significant regions of diffused ischemia and coagulative necrosis, as well as regions of villus tissue likely disrupted by fibrin injection (Tisseel).

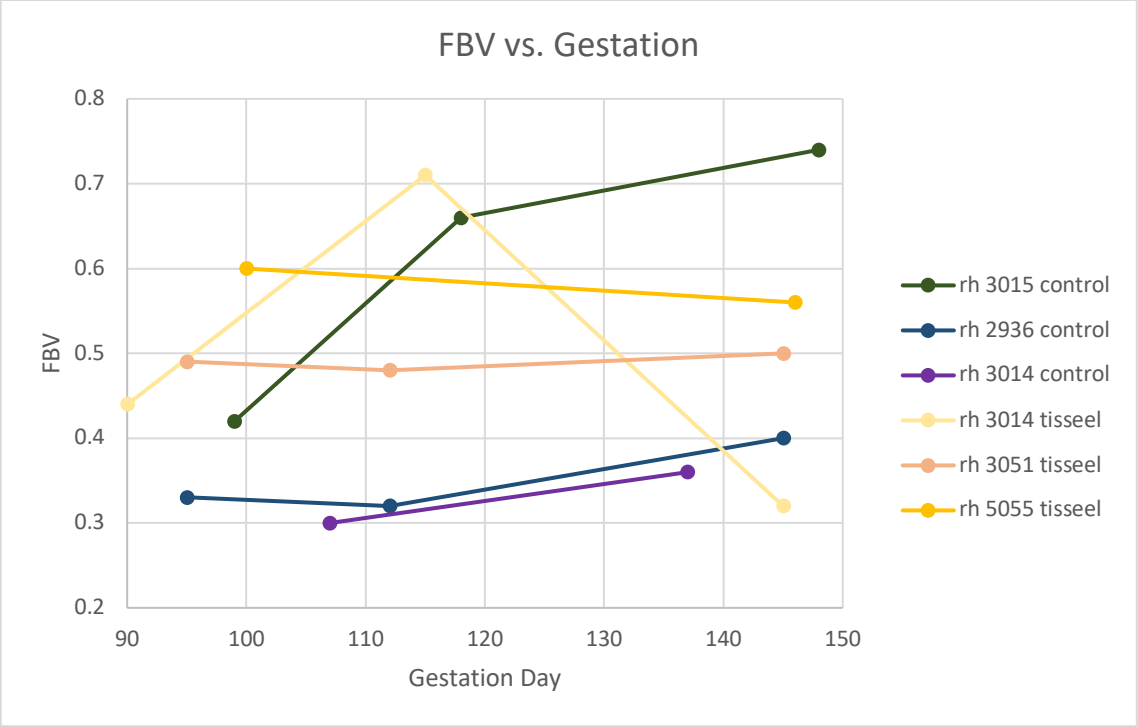

Figure 24. Mean FBV as a function of gestation age for all six subjects.

The control subjects have a trend of increasing FBV with gestation, whereas the Tisseel-treated subjects have a relatively constant trend through gestation, with the exception of rh3014, who demonstrated significant pathology and a sharp rise followed by a sharp decline of FBV across the 3 time points.

Figure 25 shows three non-consecutive slices of maternal fractional blood volume (plotted as heat map overlaid on top of the T1-weighted anatomical images) for subject rh3014, and one control subject on the bottom row. Upon visual inspection, we did not observe congregated regions of low blood volume in the MRI of the first gestation timepoint (before Tisseel injection). However, the second and third gestational timepoint show visually distinct regions of low blood volume regions (white arrow), suggesting potential tissue necrosis and ischemia.

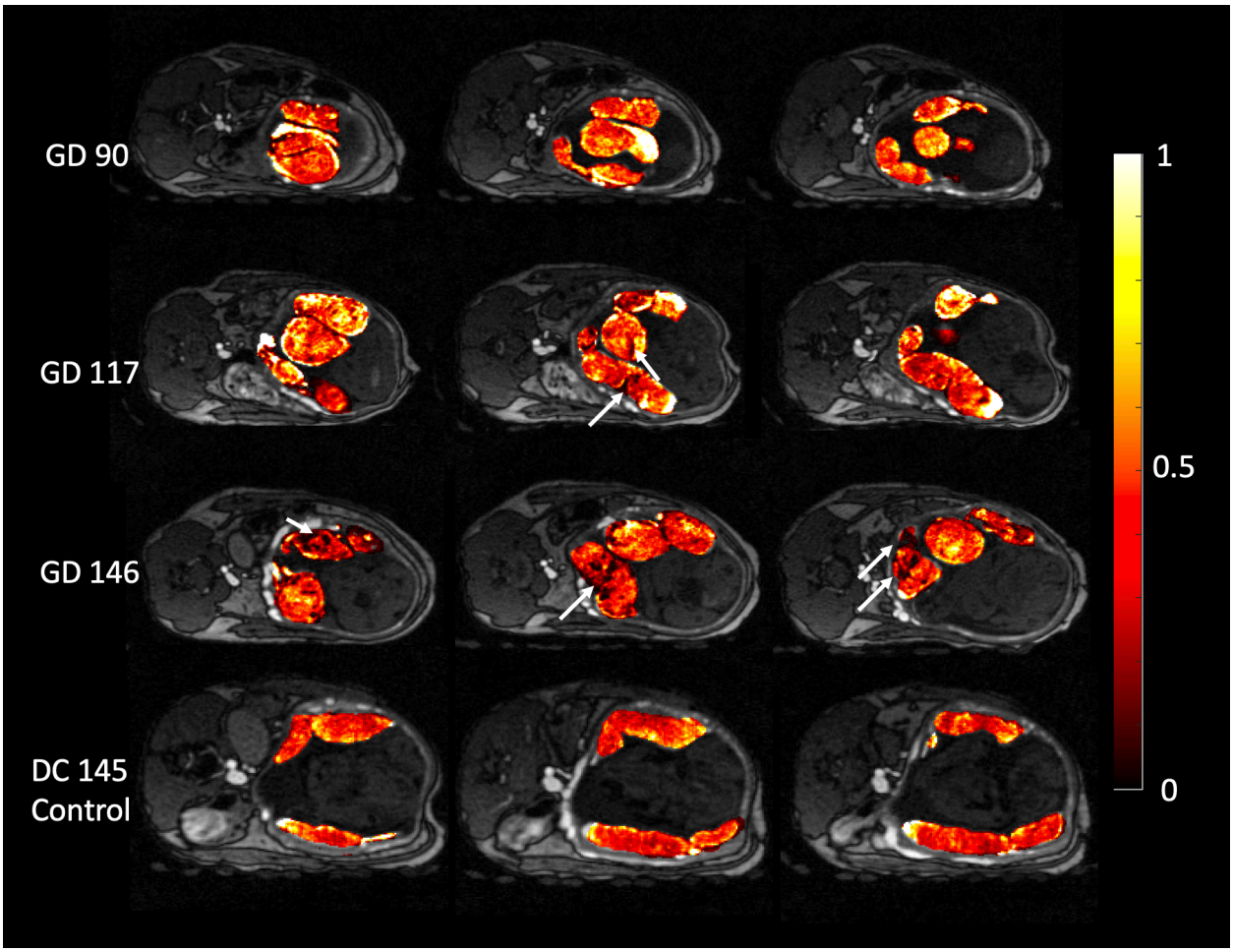

Figure 25. Three non-consecutive slices (left to right) imaged for three gestational timepoints (top to bottom) of one Tisseel-treated subject, and a control subject (bottom row).

Low blood volume regions (dark red or black), indicated by the white arrows, are rarely present before the Tisseel injection at day 90, whereas many of those are visible at day 146.

Figure 26 shows histograms of ΔR1 and FBV of subjects rh3014 and rh2936 (a representative case from the control group). In comparison, the histograms of rh3014 reflect increased regions of reduced FBV in scan 2 which further increases in scan 3.

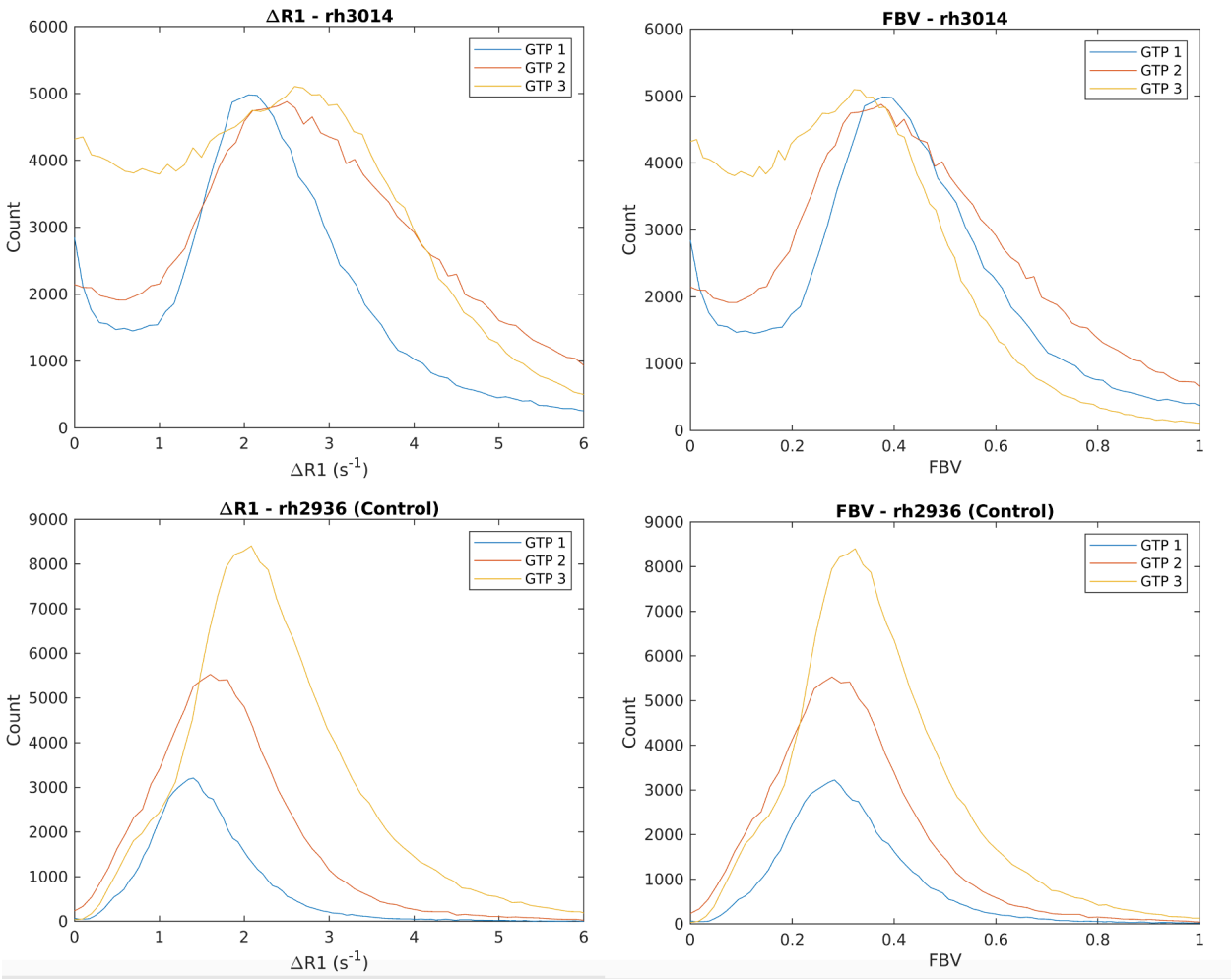

Figure 26. R1 and maternal fractional blood volume (FBV) and for a Tisseel-treated subject and a control subject at all three gestational timepoints (GTPs).

The number of pixels that has low FBV and ΔR1 increases with gestation for rh3014, whereas rh2936 demonstrates a closer to normal distribution with a slightly increasing mode with gestation.

4.6.3 Discussion

This study reports maternal fractional blood volume in a preclinical intervention model designed to create vascular infarcts in the placenta. Histopathological analysis showed diffused ischemia and coagulative necrosis in multiple cotyledons for one Tisseel-treated subject. The FBV maps reflect such conditions through visible low blood volume regions on multiple cotyledons presented throughout the slices; this condition was not reflected by the FBV on the first gestational

timepoint, as Tisseel injections were not introduced then. FBV histograms also quantitatively show the low blood volume regions in the Tisseel-treated subject that are increasing in volume with gestation, likely caused by tissue ischemia and/or necrosis. These results indicate that the intervention was successful in at least one subject and that noninvasive FBV measures are sensitive to the created infarct regions. Future studies will investigate local comparisons between the in vivo FBV data and placental pathology.

Acknowledgements

We gratefully acknowledge GE Healthcare for research support of UW-Madison, and funding support from NIH-NICHD (R01HD103443).

Chapter 5. Cotyledon-Specific Flow Evaluation of Rhesus Macaque Placental Injury using Ferumoxytol Dynamic Contrast-Enhanced MRI

5.1 Introduction

Maternal placental vasculature plays a crucial role in facilitating the exchange of oxygen, carbon dioxide, nutrients, and waste between the mother and the fetus during pregnancy. Abnormal development of the placental vasculature, which is associated with conditions such as local malperfusion, can lead to gestational complications, such as preeclampsia, small for gestation age infants, and pre-term birth[24,27,68]. Therefore, early assessment of placental perfusion and blood flow could be valuable for predicting pregnancy trajectories and possibly allow early intervention if problematic suboptimal growth is identified.

Ferumoxytol is an FDA-approved iron nanoparticle-based supplement for the treatment of anemia, including during pregnancy. Ferumoxytol is frequently used as an off-label MR contrast agent, including clinical applications in pediatric and pregnant patient populations[130,131]. Studies show that ferumoxytol does not cross the maternal-fetal barrier, thus decreasing the risks to the fetus associated with contrast infusion[24,74,117]. Additionally, ferumoxytol was determined to have little to no risk to the mother or the fetus through detailed pathological analysis in a non-human primate model[117]. It has been found to be a safe and viable off-label alternative to gadolinium-enhanced magnetic resonance angiography for assessment of pulmonary embolism (PE) in pregnancy in 94 patients[57,119], and has been proposed as a new approach to characterize internal placental structure in placenta accreta spectrum[118,126].

Dynamic contrast enhanced (DCE) MRI is a promising tool to non-invasively assess placental perfusion and blood flow in vivo throughout gestation. Recent studies have shown promising results in animal studies using DCE MRI to identify functional units in the placenta, or cotyledons, which facilitate nutrient and oxygen exchange between the mother and the fetus, and quantify their number, volumes, and flow[24,74,132]. However, few cotyledon-specific flow values in the presence of placental abnormalities have been reported[74]. Here, we report initial results for DCE analysis of two novel rhesus macaque models designed to induce placental injuries. We hypothesized that placental Tisseel injections would create local infarcts that could be detected as regions of reduced flow with DCE MRI and that placental MCP-1 injections would provoke an inflammatory response with subsequent flow changes detectable with DCE MRI.

5.2 Methods

Subjects: This study was approved by the Research and Graduate Education Institutional Animal Care and Use Committee. Female rhesus macaques were housed with compatible males and monitored for breeding and menses. Date of conception was determined (+/- 2 days) based on initiation of the menstrual cycle, observation of copulation and presence of ejaculate, and ultrasound measurements of fetus and gestational sac[74]. Full term in Rhesus Macaques is approximately 165 days[133]. Three out of the eleven animals went through multiple pregnancies for this study (two went through two pregnancies and one went through three pregnancies), each with a different treatment. Macaques were cared for as outlined in the Animal Welfare Act and the Guide for the Care and Use of Laboratory Animals.

Imaging: Eleven female rhesus macaques were imaged at up to three gestational days (GDs) of ~100, ~115, and ~145 days (Table 8). The full-term gestation age of rhesus macaques is approximately 165 days. One day after the first MRI session, monkeys were injected with 0.5 ml

Tisseel (n=3), 100 ug MCP-1 (n=3), or saline as controls (n=3). All injections were conducted by an experienced obstetrical clinician under ultrasound guidance and targeted to occur in the intervillous space of the anterior lobe of the placenta. Additionally, another n=2 monkeys received 1.5ml Tisseel injections, with the Tisseel being instilled as the needle was being withdrawn from the placenta. The fetuses were delivered via cesarean section at around gestational day 155, and the placentas were obtained for histopathological analysis by a veterinary pathologist.

Table 8. Rhesus macaque treatment, imaging, and delivery date, in gestation day.

Rhesus & Treatment	MRI #1	MRI #2	MRI #3	Delivery & Dissection
Control #1	95	112	145	155
*Control #2	99	-	148	156
***Control #3	-	107	137	155
Tisseel #1	100	-	147	155
**Tisseel #2	-	117	146	154
***Tisseel #3	90	117	146	154
Tisseelx3 #1	-	121	149	156
*Tisseelx3 #2	-	114	139	155
*MCP1 #1	100	115	142	155
MCP1 #2	100	114	144	155
**MCP1 #3	-	114	142	156

*,**,***: Animals that went through multiple pregnancies in this study.
Tisseelx3: Treatment group that received 3 doses of Tisseel.

All scans were performed on a 3.0 T clinical system (Discovery MR750, GE Healthcare) with a 32-channel phased array coil. The animals were sedated by inhalation of 1.5% isoflurane mixed with oxygen and imaged in right-lateral position. Respiratory bellows were used to track respiratory motion during imaging.

A series of time-resolved 4D DCE data sets were acquired during ferumoxytol (Feraheme, AMAG Pharmaceuticals; 4mg/kg, diluted 5:1 with saline), using a respiratory-gated, T1-weighted spoiled gradient echo sequence (DISCO, TR=4.8ms, TE=1.8ms, spatial resolution=0.86×0.86×1.00mm3, number of timeframes = 40). Ferumoxytol and a subsequent flush with 20 ml of saline was administered at 0.5 ml/s with a power injector (MEDRAD® MRXperion MR Injection System, Beyer Healthcare) at the time the scan was started. Equidistant temporal resolution was 4.5s for the control, MCP-1, and Tisseel groups, and 7.7s for the two Tisseelx3 animals to capture potential longer contrast arrival times.

Processing: Semi-manual segmentation (ITK-SNAP 4.0)[113] of the placenta was performed by a graduate student with 5-year experience in placental MRI analysis using the 3D volume from the last timepoint of the DCE imaging sequence. Subsequently, the temporal signal intensity of each voxel in the placenta was fitted to a sigmoid arrival model, and the inflection point of signal enhancement was used to form a contrast arrival time map[74].

Different from prior work, a 3D watershed algorithm (3D suite, ImageJ[134]) was used to identify individual perfusion domains based on detected boundaries in the 3D arrival time map. This algorithm first uses distance transforms to obtain the distance maps, which shows the relative distance between each point and the edge of the object boundaries. The local maxima of the distance map (which correspond to the center of each cotyledon) is then set as the seed point of each domain. The region grows out at a speed depending on the value of the distance map: the higher the distance, the larger the cotyledon and the faster the domain grows. The region stops growing when it reaches the minima of the distance map, which also represents the boundary of each region. Blood flow to each domain (ml/min) was calculated as the largest slope in the total volume of enhanced voxels over time. This is accomplished by calculating the zero point of the

secondary derivative of the fitted sigmoid function. Additionally, a visual cotyledon matching was performed between color photos of the dissected placenta after delivery at term and the DCE MRI-derived 3D in vivo renderings of the individual domains. Figure 27 shows an illustration of this workflow which was adopted from previous studies[24,74,132] and modified by replacing the previously used 2D watershed with a 3D watershed algorithm.

Statistical Analysis: The two animals who received the 1.5ml dose of Tisseel are considered as a separate treatment group (Tisseelx3) from the single dose. Each of the four (Control, MCP-1, Tisseel, Tisseelx3) treatment groups were compared for the distribution of cotyledon volume and volumetric flow for each cotyledon, which was defined as the volume of maternal blood entering a cotyledon per unit time. Additionally, we recorded normalized flow for each cotyledon, which was calculated as flow over volume for each cotyledon, to visualize changes in flow without impact from the cotyledon volume. Box-and-whisker plots were used to visualize such distributions, and the Wilcoxon rank sum test (MATLAB 2022b, MathWorks, Natick, USA) was used to determine the statistical difference ($p<0.05$) between each treatment group. Finally, total blood flow, calculated as the sum of each cotyledon's flow (not normalized), was calculated. In order to track placental growth through time, longitudinal plots across three gestational time points were generated for total placental volume, placental surface area, and total placental flow.

Detailed pathological analysis on all animals was conducted by a veterinary pathologist with over 15 years of experience. Methods include morphological inspection and histological analysis of selected hematoxylin and eosin-stained tissue slices that are central-cut through the entire placenta. Qualitative necropsy report was generated for each animal detailing the ischemic changes throughout the placenta.

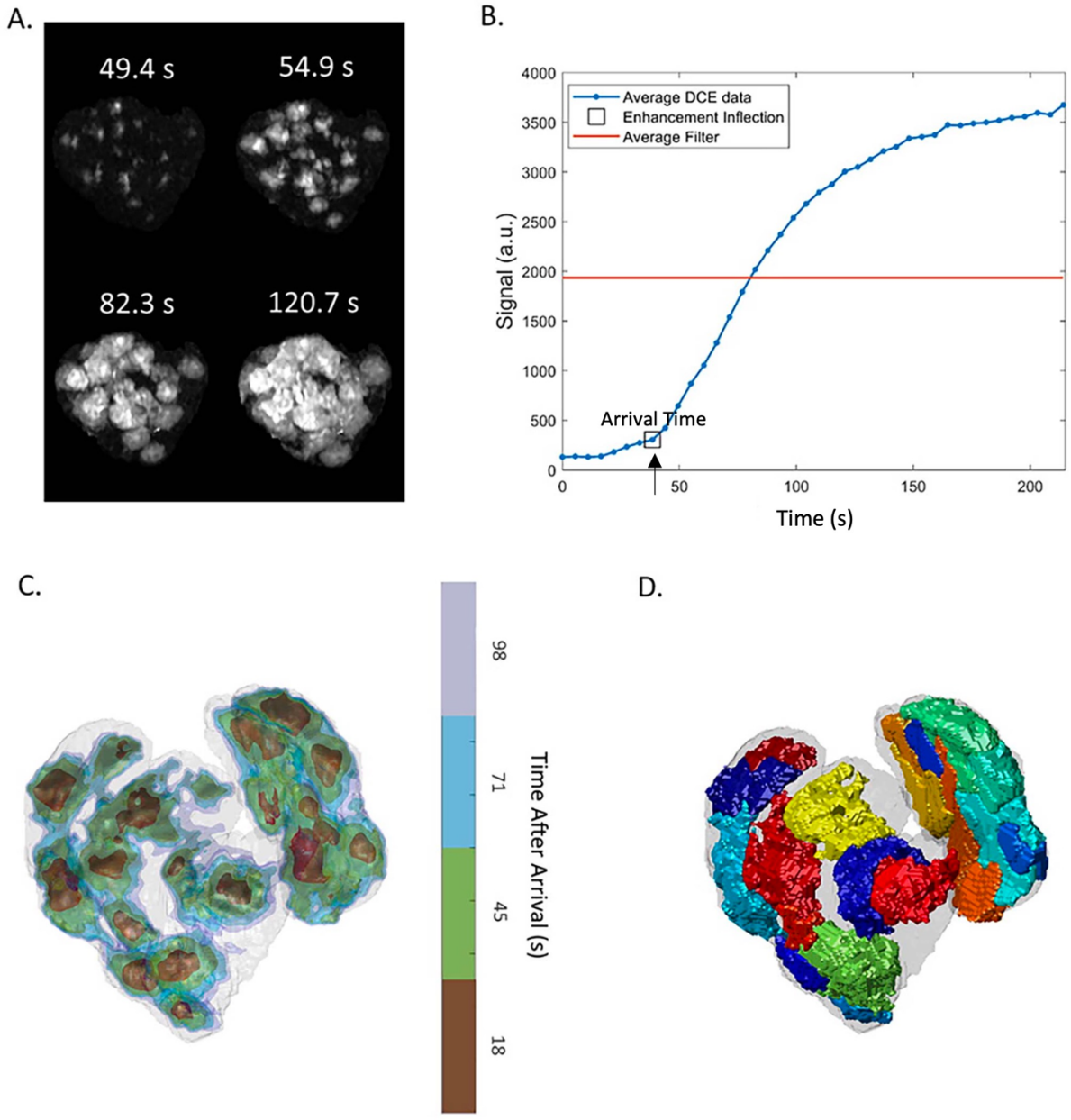

Figure 27. Dynamic contrast enhanced MRI processing workflow.

A) The DCE MRI generates a dynamic series of 40 3D volumes, shown here for 4 timeframes during the arrival of the Ferumoxytol bolus. B) The corresponding signal enhancement over time is used to determine the contrast arrival time highlighted in square. C) 3D contrast arrival time mapped for the entire placenta indicating arrival zones (brown) and peripheral zones (green) of the perfusion domains. D) The perfusion domain map determined using the watershed algorithm, where each perfusion domain is shown in a different color.

5.3 Results

Image acquisition and analysis was successfully conducted for all imaging exams. Unexpectedly, a number of the injury model placentas only developed one placental disc, which deviates from the normal rhesus two-disc pattern (2/3 Tisseel, 2/3 MCP1, 0/3 controls, 0/2 Tisseelx3). Out of the eleven rhesus macaques analyzed, one Tisseel-treated placenta (0.5ml dose) was noted upon histological analysis (Figure 28) to have tissue ischemia that multifocally affects large portions of several cotyledons. In addition, both Tisseelx3 animals were shown via histopathology to have visible areas of multifocal ischemia with coagulative necrosis across the entire placental tissue. Qualitative assessment of written pathology reports from the other animals shows very moderate pathology likely due to underlying factors not associated with Tisseel injection.

Table 9 shows mean and standard deviation of cotyledon volume, flow per cotyledon, normalized flow per cotyledon (flow over cotyledon volume), and total flow for each animal at the third imaging timepoint (GD ~145). For reference, the total number of cotyledons (n) for each treatment group at that timepoint is n=31 for controls, n=28 for MCP-1, n=29 for Tisseel, and n=36 for Tisseelx3. The mean cotyledon volumes (5.5 ml, 5.7 ml), flow per cotyledon (2.9 ml/min, 3.3 ml/min) and total maternal placental flow (57.4 ml, 52.9 ml) for the two Tisseelx3 animals are lower than the same parameters for the control animals.

Longitudinal analysis (Figure 29) confirms increases in placental volume, placental surface area, and total maternal placental flow with gestational age, except for the two Tisseelx3 animals, which show slight decrease in total flow from the second to the third gestational timepoints confirming the utility of Tisseel in inducing placental injury.

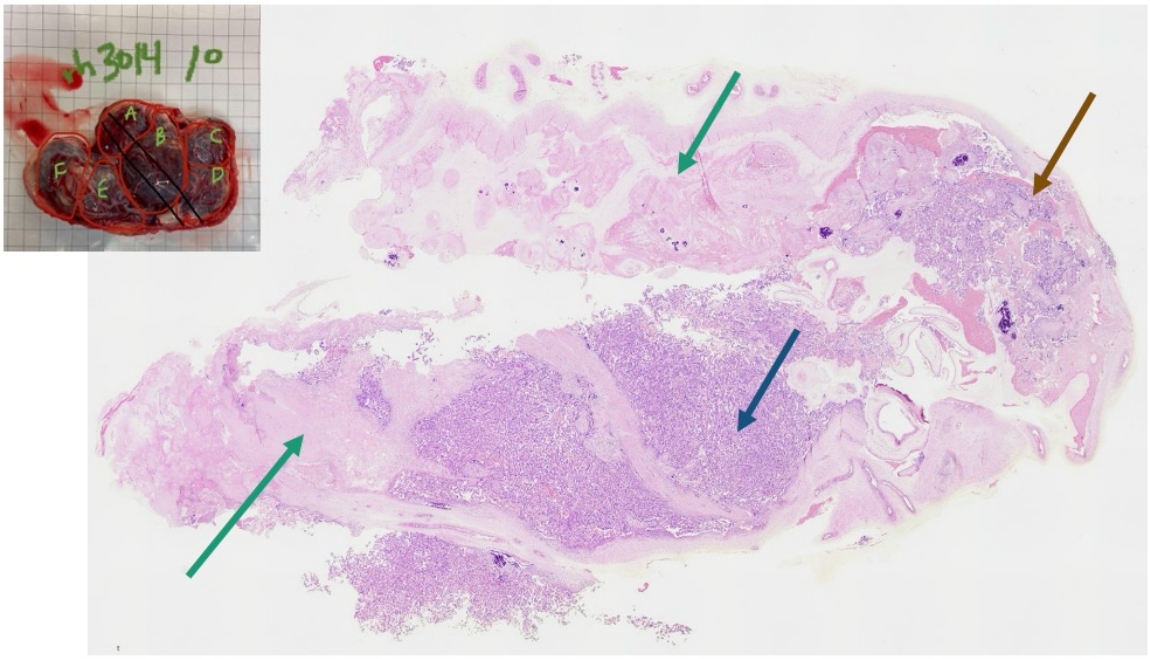

Figure 28. Histopathological central slice of placenta treated with Tisseel injection.

Green arrows are pointing to areas with diffused ischemia and coagulative necrosis characterized by loss of secondary and tertiary villi; dark blue arrow is pointing to healthy villus tissue; brown arrow is pointing to villus tissue likely disrupted by Tisseel.

Table 9. Cotyledon volume, flow per cotyledon, normalized flow per cotyledon, and total flow for each animal at the third imaging timepoint (GD ~145).

Rhesus & Treatment	Cotyledon Volume (ml)	Flow per Cotyledon (ml/min)	Normalized Flow per Cotyledon (min^{-1})	Total Placental Flow (ml/min)
Control #1	7.8±4.5	5.2±3.0	0.70±0.18	67.0
Control #2	9.2±5.3	7.0±3.9	0.79±0.17	69.7
Control #3	10.8±6.1	9.1±3.8	0.91±0.32	72.5
Tisseel #1	12.6±3.8	10.9±2.5	0.84±0.10	65.5
Tisseel #2	10.2±3.5	7.5±2.3	0.75±0.17	60.0
Tisseel #3	7.6±2.4	6.9±1.9	0.95±0.31	102.9
Tisseelx3 #1	5.5±2.9	2.9±1.5	0.53±0.08	57.4
Tisseelx3 #2	5.7±3.3	3.3±2.9	0.53±0.15	52.9
MCP1 #1	7.5±4.2	5.9±3.1	0.82±0.17	89.0
MCP1 #2	18.8±9.0	11.8±6.4	0.61±0.05	59.0
MCP1 #3	11.7±8.7	10.0±5.6	1.03±0.33	79.9

Tisseelx3: Treatment group that received 3 doses of Tisseel.

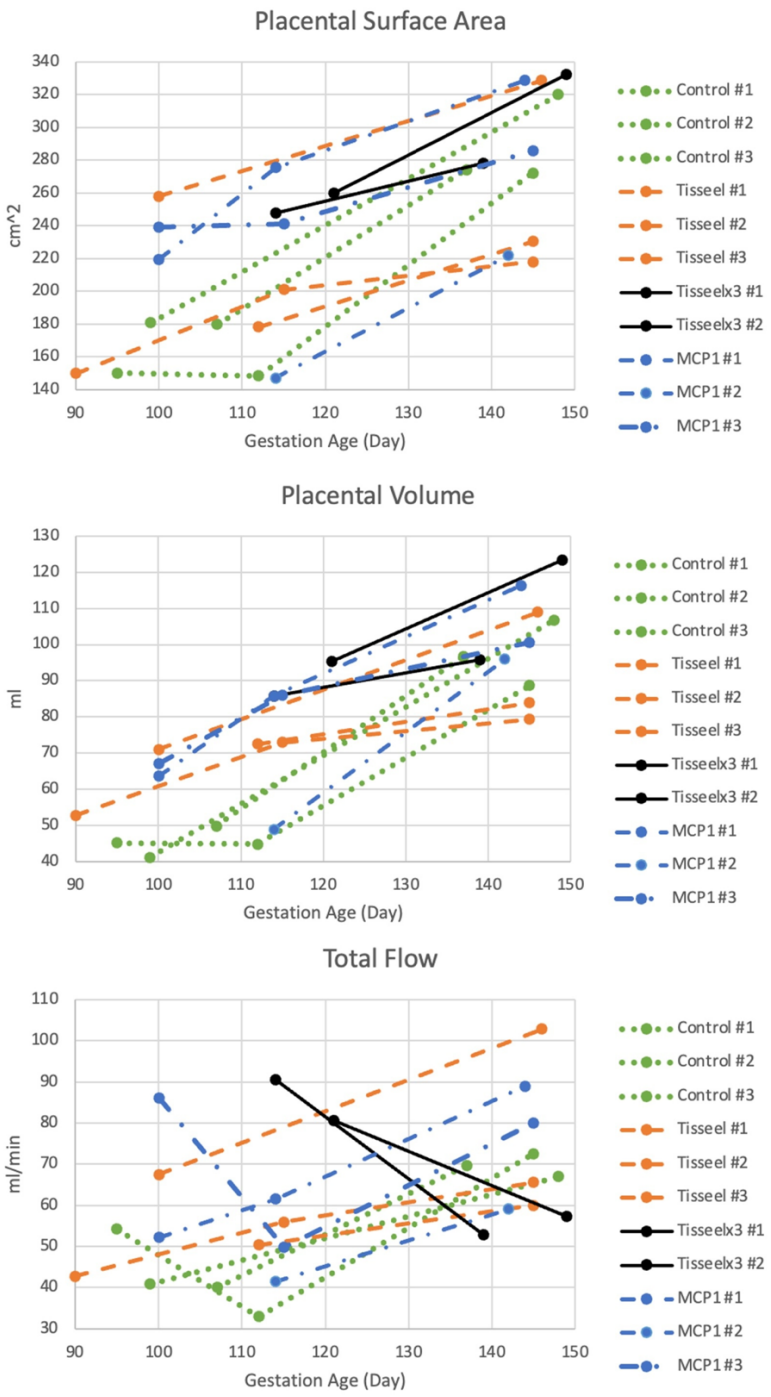

Figure 29. Longitudinal plots of placental surface area, placental volume, and total maternal flow across three imaging timepoints for all eleven animals.

All variables increase slightly with gestation, except for the total flow, where the animal who received three Tisseel injections decrease in flow from the second to the third gestation time points.

Significantly lower flow, cotyledon volumes, and normalized flow (flow divided by volume) for the Tisseelx3 treatment groups at GD 145 (approximately 45 days after the Tisseel treatments) were observed and are presented in Figure 30. Interestingly, this is not observed at the second gestational time point, which is approximately two weeks after treatment. There is no such change in blood flow between the other two treatment groups (MCP-1 and Tisseel) for either gestational time points.

The fast-arrival regions (center of cotyledon, red color) on the contrast arrival time maps (Figure 31) decrease in volume with gestation, likely due to the injection of Tisseel. The number of cotyledons decreases with gestation for the one Tisseel (single dose) animal that demonstrated pathology. The similar decrease in the fast-arrival regions is also observed with the Tisseelx3 animal on the bottom of Figure 31. Both animals have good agreements between arrival time maps and the placenta dissection photo. A comparison between the arrival time histograms between the Tisseel-treated animal and a control animal show decreased mode arrival time with gestation for the Tisseel animal. This could further corroborate the negative influence of Tisseel injection on placental intervillous blood flow. A comparison between the Tisseelx3 animal and the control animal shows a longer mode arrival time in the Tisseelx3 animal. Although the mode arrival time does not change for the two gestational timepoints, the arrival time is more heavily skewed to the right for the third gestational timepoint in the Tisseelx3 animal's histogram.

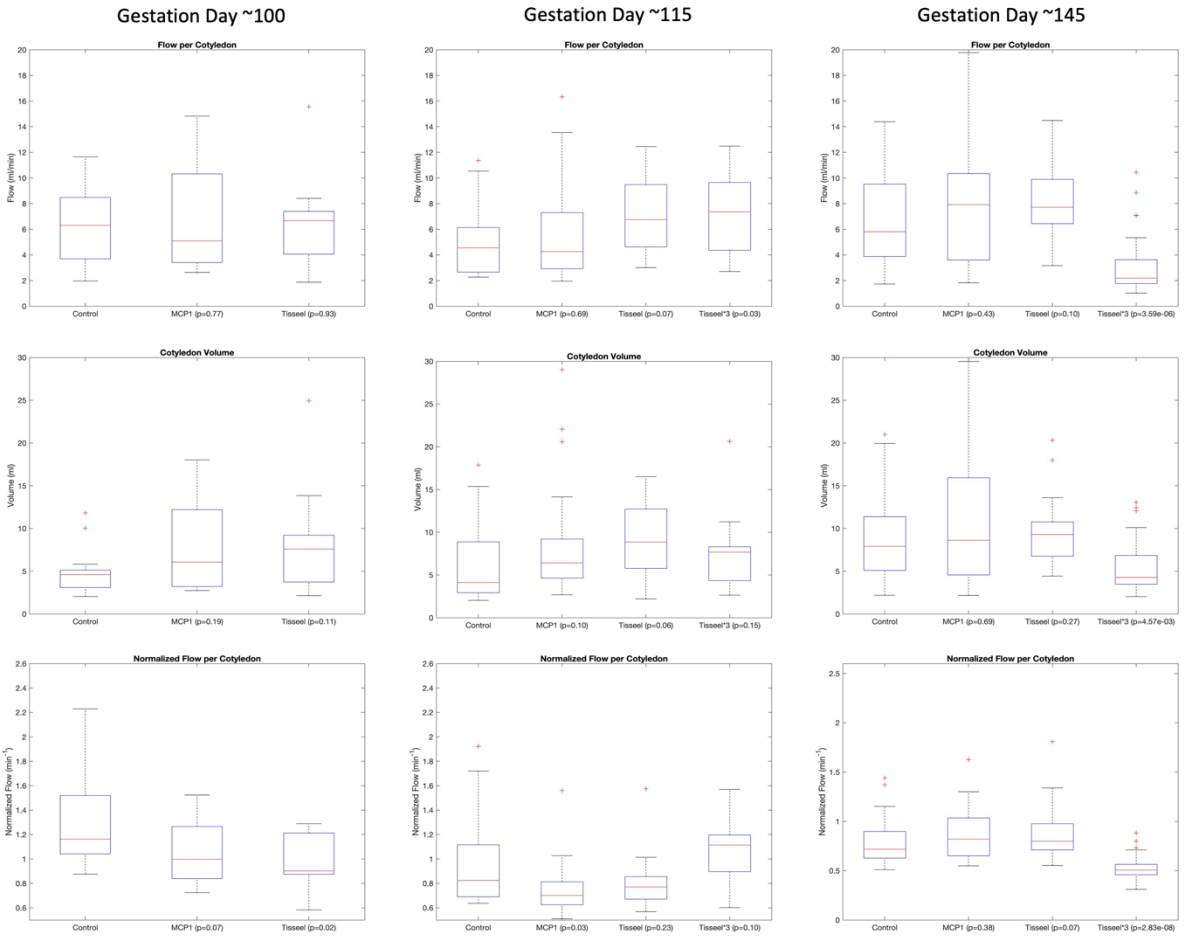

Figure 30. Box-and-whisker plots of flow, volume, and normalized flow of each cotyledon for each gestational timepoint (GTP; left to right).

The p-value of the Wilcoxon rank sum test for each treatment group comparing to the control animals are shown in the legends on the bottom of each plot.

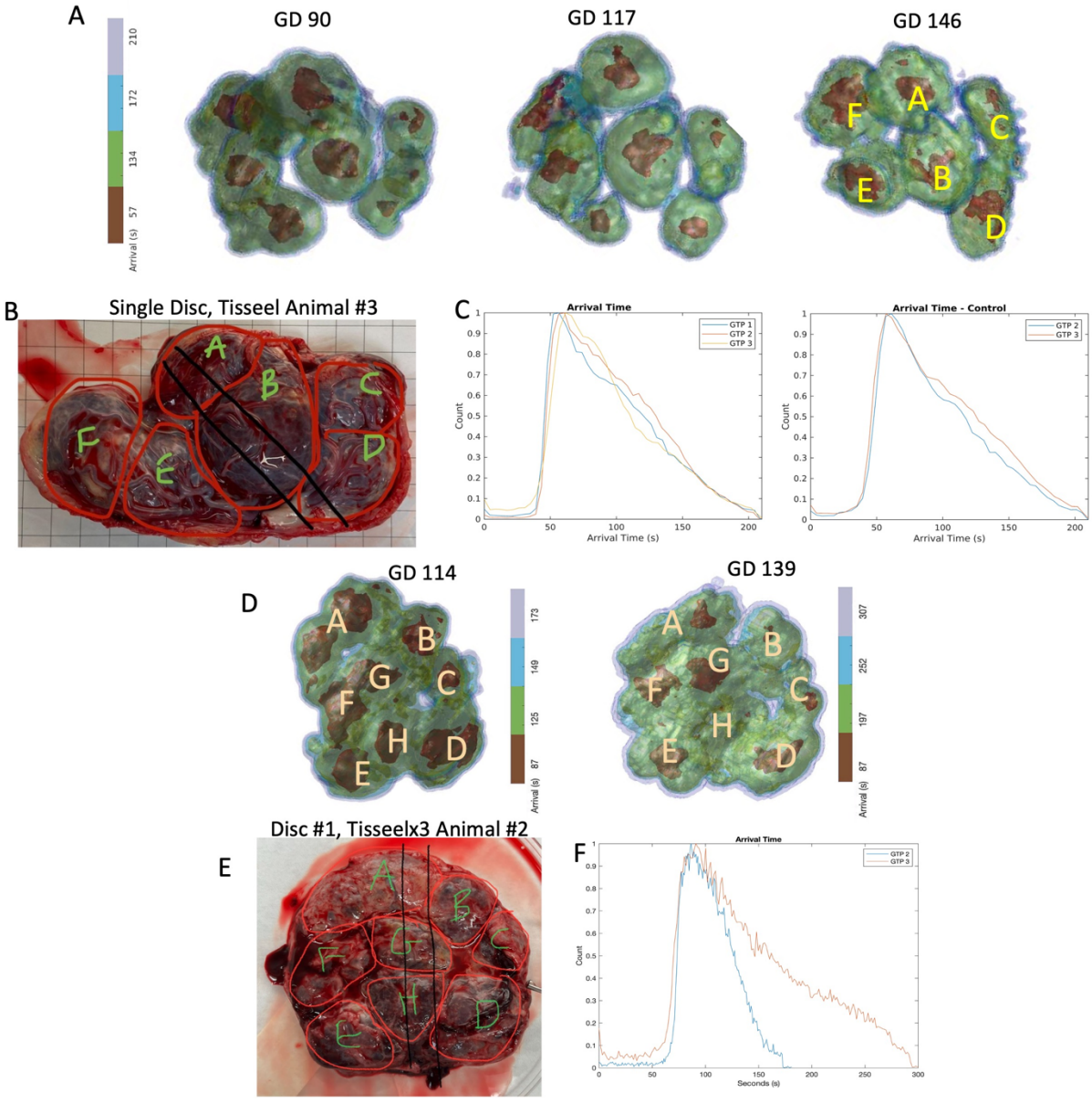

Figure 31. Contrast arrival time maps for each gestational timepoint (A), a photo of the placenta at dissection (B), and arrival time histograms (C) at available gestational time points (GTP) for a Tisseel-treated and a control animal.

Apparent decrease in cotyledon number is observed throughout gestation; additionally, the central region of each cotyledon (arrival time < 20s) decreases slightly relative to the cotyledon size. The arrival time map at GD 146 matches well anatomically with the placenta at dissection. Bottom: arrival time maps (D) at two gestational timepoints (~1 day and ~15 days after treatment), dissection photo (E), and arrival time histograms (F) of the two timepoints (GTPs).

5.4 Discussion

This study introduces two new models for placental injuries in the rhesus macaque using MCP-1 and Tisseel injections and demonstrates successful measurement of cotyledon-specific flow parameters for these models. To date, no established model for local placental injuries exists. The Tisseel injections, particularly the triple dose, caused placental injury that was identified in histopathology and MRI, making it a promising approach that warrants further pursuit into optimal intervention timing and dose to become a robust animal model. Meanwhile, the MCP-1 injections did not evoke trackable changes in histopathology or MRI, thereby this animal model with its currently protocol is not useful.

The analysis workflow in this study is adapted from previous studies[135][132], with changes including imaging parameters, watershed algorithm, and flow fitting methods. This could contribute to a lower average total placental flow of the three control animals (69.7 ml/min) compared to previously reported volumetric flow (403 ml/min) [132]. However, the total flow in our study is comparable to that of a previous study using similar analysis workflow (63.5 ml/min). Additionally, significantly lower cotyledon volume was observed in the Tisseelx3 animals at around gestation day 145, which agrees with a previous study using pathological models induced by ZIKA virus[74]. Longitudinal analysis confirms slight increase in placental volume, placental surface area, and total maternal placental flow with gestation age as previously observed[74].

Significantly lower flow parameters were observed for the Tisseelx3 treatment groups at GD ~145 (approximately 45 days after the Tisseel treatments), which agrees with the preliminary histopathology analysis that indicates seemingly more infarcted and fibrotic tissue. Tissue fibrosis could have hemodynamic impact that compromises placental transport of nutrients to the fetus[136]. Interestingly, the decrease in flow parameters is not observed at GD ~115 (15 days after Tisseel

treatments), even though a previous study has shown that Tisseel induces almost immediate (within 4 to 10 minutes) hemostasis[67]. This could be due to the combination of progressive placental insufficiency with time, as well as the increasing demand from the fetus as gestation progresses[137]. There was no such change in blood flow between the other two treatment groups (MCP-1 and Tisseel) for either gestational time point, comparing to the controls. This is possibly due to insufficient injury in the first place or placental plasticity that can compensate for certain degrees of injury; a previous study has shown that the rhesus macaque placenta can compensate for up to a 40% reduction in functional capacity[138]. This also agrees with our preliminary pathological findings in that the two treatments only resulted in modest placental injuries, except for one animal treated with Tisseel that was histologically shown to have ischemia in multiple areas of the placenta.

The decrease of the central region of the contrast arrival time maps with gestation could further corroborate the negative influence of Tisseel injection on placental intervillous blood flow, since this suggests larger regions of the placenta that take longer for the contrast agent to reach. Interestingly, for the Tisseel animal and the two Tisseelx3 animals, although the injections occurred locally (and likely distributed through multiple cotyledons for the Tisseelx3 group), all cotyledons show various amount of decreased center of flow. Depending on the significance of the vascular structure at the injection site, the introduction of Tisseel could impact one or multiple portions of the maternal villous tree, causing a global effect on placental flow[139].

This study applied several improvements to existing methodology[74], which was adapted from a study by Schabel et al as previously mentioned[132]. We made some changes in the algorithms that could potentially increase the accuracy of cotyledon blood flow measurements. First, this study uses a 3D watershed algorithm (3D suite, ImageJ[134]) instead of a 2D-based algorithm to

automatically segment the individual cotyledons. This new algorithm calculates the distance map and performs region growth in 3D, rather than in 2D with a pixel connectivity index, which gave us improved robustness. In addition, the calculation of individual cotyledon flow in this study is based on the highest slope in the enhanced volume vs. time curve. This was accomplished by calculating the first derivative numerically and choosing the arrival time with the highest value. This method could result in greater robustness for flow calculation than the previous implementation which used a linear fit of the cumulative total volume of enhanced voxels over time, which heavily depends on accurately determining the start and end time of signal enhancement[74]. In addition, this study reports normalized blood flow, calculated as blood flow per volume of each cotyledon. Previous studies have reported the positive association of placental growth and flow changes with time[140,141]. In our study, the flow is calculated as the volume of maternal blood entering the cotyledon per unit time, which could be largely impacted by the cotyledon size, since larger cotyledon usually contains more maternal blood. Therefore, normalizing the flow could potentially remove the confounding factor cotyledon size has on the flow.

Limitations

Our study has a modest sample size: 2-3 placentas per treatment group, 6-15 cotyledons per disc of placenta. A considerable number of animals only developed a single placental disc, which was unexpected given the reported low percentage (9.5%) of monodiscoid placenta in rhesus macaques[142]. This was not caused by the injury models as the single disc placentas had already developed at the time of injury. Single disc placentas could potentially bias the flow per cotyledon due to the different distribution of blood to a single placenta as opposed to two discs. The small sample size also limits the available quantitative statistical approaches available for this study.

Potential movements of the fetus during imaging, especially for a time-dependent imaging series, could also result in inaccuracies in flow measurements.

Each pregnancy in this study is treated as an independent experiment due to the limited number of individual animals, although three of our animals went through multiple pregnancies. This could impact the independence of individual data points.

Lastly, although this study offers an overall impression of the pathological findings, detailed quantitative per-cotyledon analysis of pathology is lacking, therefore limiting the cotyledon-to-cotyledon comparison between flow and pathology.

5.5 Conclusions

This study examined the effects of MCP-1 and Tisseel injection into the placental intervillous space in rhesus macaques. Cotyledon-specific maternal placental blood flow was successfully calculated, and significantly lower cotyledon volume, flow, and normalized flow was shown for the animals who received the higher dose Tisseel injection. In addition, the injections of the lower dose of Tisseel or MCP-1 were shown to have similar pathology findings to the controls and only modest effects on placental cotyledons and flow and are unlikely to induce pregnancy complications. Directions of future studies include injection of Tisseel at an earlier gestation stage to track placental development through a longer gestational window, as well as comparing placental flow with a more quantitative pathological description of each cotyledon.

Acknowledgements

We gratefully acknowledge GE Healthcare for research support of UW-Madison, and AMAG Pharmaceuticals for providing ferumoxytol used in our imaging procedures. We also thank the Wisconsin National Primate Research Center (WNPRC) Veterinary, Scientific Protocol

Implementation, and Animal Services staff for providing animal care, and assisting in procedures including breeding, pregnancy monitoring, and sample collection.

Chapter 6. Vasculature Assessment of Rhesus Macaque Placental Injury using Variable Flip Angle T1-Mapping and Dynamic Contrast Enhanced MRI

6.1 Introduction

Maternal placental vasculature development during pregnancy could play a crucial role in a successful gestational outcome[143–145]. Placental vasculature function is governed by multiple parameters including oxygenation and perfusion. Combining relaxation times, such as T2, T2*, and T1 might permit estimation of SO2, pO2, and hematocrit levels[146]. Previous study has found similar patterns between T2* maps and early uptake using DCE MRI in rhesus macaques, particularly a spatial correlation of high perfusion regions or inflow zones[147]. However, such local comparison focusing on regions of potential placental infarction and necrosis is currently lacking, as there are few cases with induced placental thrombosis available for imaging.

Ferumoxytol is an FDA-approved iron supplement used off-label as MRI contrast agent and has been shown to provide good depiction of maternal placental vasculature, including the placentas on the placenta accreta spectrum[148–150]. Studies show that ferumoxytol does not cross the maternal-fetal barrier, thus decreasing the risks to the fetus associated with contrast infusion[24,74,117]. Additionally, ferumoxytol was determined to have little to no risk to the mother or the fetus through detailed pathological analysis in a non-human primate model[117].

Previous studies have shown promising results to quantify maternal placental perfusion in animal models using two ferumoxytol-enhanced MRI methods: dynamic contrast enhanced (DCE) MRI[24,74,132] to measure placental blood flow on a cotyledon-specific level, and pre- and post-contrast T1-weighted variable flip angle (VFA) T1 mapping[58,120] to measure fractional blood

volume in mice, rhesus macaques, and human subjects with fetal growth restriction. However, limited studies have evaluated these two methods with reference to each other, especially on a more local scale, to compare sites with more modulated perfusion, such as placental inflow zones (high perfusion) and diseased sites with inflammation and/or tissue necrosis (low perfusion).

This study applies Tisseel (Baxter Healthcare Corp) injections for three rhesus macaques in the anterior lobe of the placenta to create local placental thrombosis. Tisseel is an FDA-approved fibrin sealant used surgically to stop bleeding[67]. The infarcts caused by Tisseel could mimic biological processes that holds potential to contribute to clinical gestational complications such as fetal growth restrictions. Previous study has shown from histopathological analysis that Tisseel injection for three rhesus macaque animals has likely caused coragulative necrosis in the placental tissue likely caused by the injection[151]. Subsequently, the impedance of cotyledon-specific blood flow likely resulting from the same placental injuries was also observed using ferumoxytol-enhanced DCE MRI[151]. Additionally, maternal placental blood volume mapping on the same animals shows similar trend of areas with low blood volume[152].

We hypothesize that co-registered ferumoxytol contrast arrival time maps from DCE MRI and fractional blood volume maps from VFA T1-mapping could provide better visual assessment for placentas with local tissue infarction and necrosis.

6.2 Methods

Subjects: Three rhesus macaque subjects went through MRI session at gestation days 146, 149, and 139, respectively. At around gestation day 100, all subjects received Tisseel injections in the anterior lobe of the placenta. One subject received a single dose of 0.5ml, whereas the other two received a dose of 1.5ml in three separate locations on the lobe.

Imaging: All scans were performed on a 3.0T system (Discovery MR750, GE Healthcare) with a 32-channel phase array coil. The subjects were sedated with isoflurane and imaged in right-lateral position. Ferumoxytol contrast agent (4mg/kg) were intravenously infused during DCE imaging. Figure 32 shows the imaging workflow for this study.

DCE Imaging and Processing[74,132]: A T1-weighted spoiled gradient echo product sequence (DISCO, TR=4.8ms, TE=1.8ms, spatial resolution=0.86x0.86x1.00mm3, temporal resolution=4.5~7.7s, number of timeframes=40) was used. Semi-manual segmentation (ITK-SNAP[113]) was performed on the last timepoint of DCE sequence. The arrival time maps were obtained by fitting pixel-wise DCE signal to sigmoid model and finding the inflection point.

VFA Imaging and Processing[120,121]: A 3D radial spoiled gradient echo sequence (TR=6.0ms, TE=1.2ms, scan time=525.9s, spatial resolution=$0.87\times0.87\times1.00mm^3$) was performed at four different flip angles (2°, 6°, 10°, 15°) before and 30 minutes after ferumoxytol infusion. Pixel-wise signal intensity of each flip angle datapoint was fitted via monoexponential fit to obtain the R1 maps. Maternal fractional blood volume (FBV) was calculated as the ratio between ΔR1 (difference between pre- and post-contrast R1 maps) in the placenta and ΔR1 in maternal blood.

Data Analysis: Registration between the 15° flip angle T1 anatomical image (moving) and time averaged DCE image (fixed) were done using deformable registration (ANTS[125]). The same placental mask was applied to the averaged DCE signal, blood volume maps, and the arrival time maps for pixel-wise comparison.

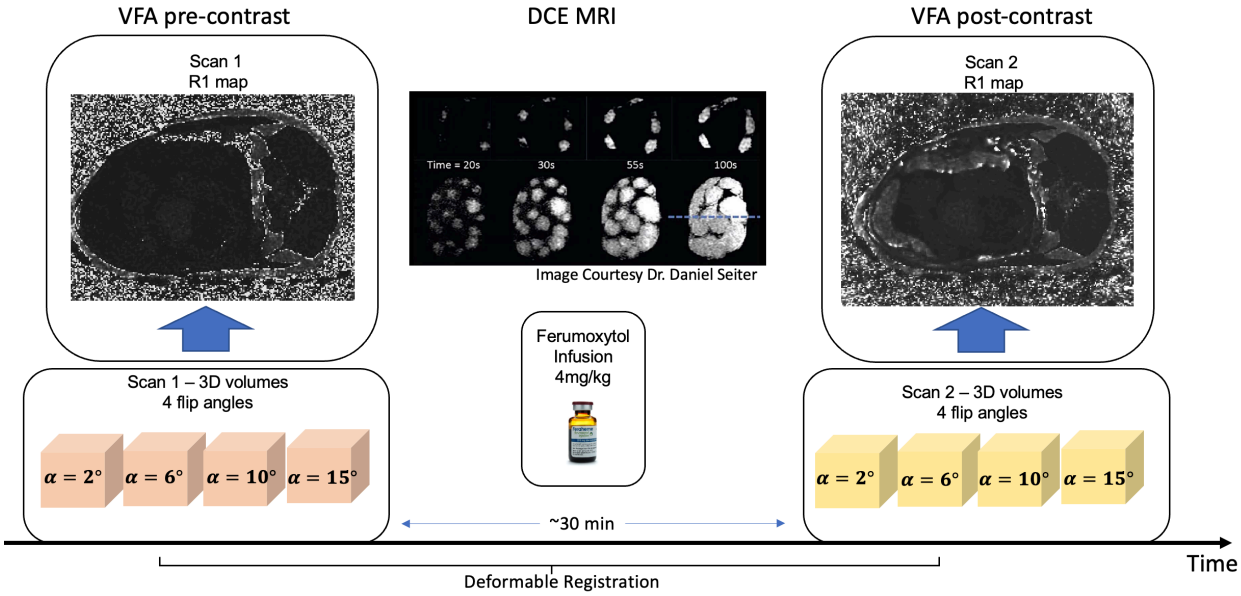

Figure 32. Imaging workflow for this study.

3D spoiled gradient echo variable flip angle (VFA) sequence was performed for four separate flip angles. During ferumoxytol infusion, dynamic contrast enhanced (DCE) MRI was performed. After approximately 30 minutes since the pre-contrast VFA sequence, the same protocol was repeated for the post-contrast imaging. The 6° pre- and post-contrast VFA images were registered to reduce motion artifacts.

6.3 Results

All scans were performed successfully with minimal imaging artifacts for processing. Blood volume maps and DCE flow maps were successfully generated for the three subjects. Histopathological analysis done by a pathologist of over 15 years of experience shows various levels of tissue necrosis and fibrosis likely associated with the injections for all three subjects.

For all three subjects, figure 33 shows co-registered Fractional blood volume map (left column), time-averaged dynamic contrast enhanced (DCE) signal (middle column), and T1-weighted post-contrast anatomical image (right column) used for blood volume calculation. Green arrows show areas of enhanced signal, whereas the red arrows show lower image signal and lower

blood volume, possibly suggesting tissue infarction and necrosis. The time-averaged DCE signal shows relatively higher motion artifact, possibly due to the lack of registration in-between each time snapshots.

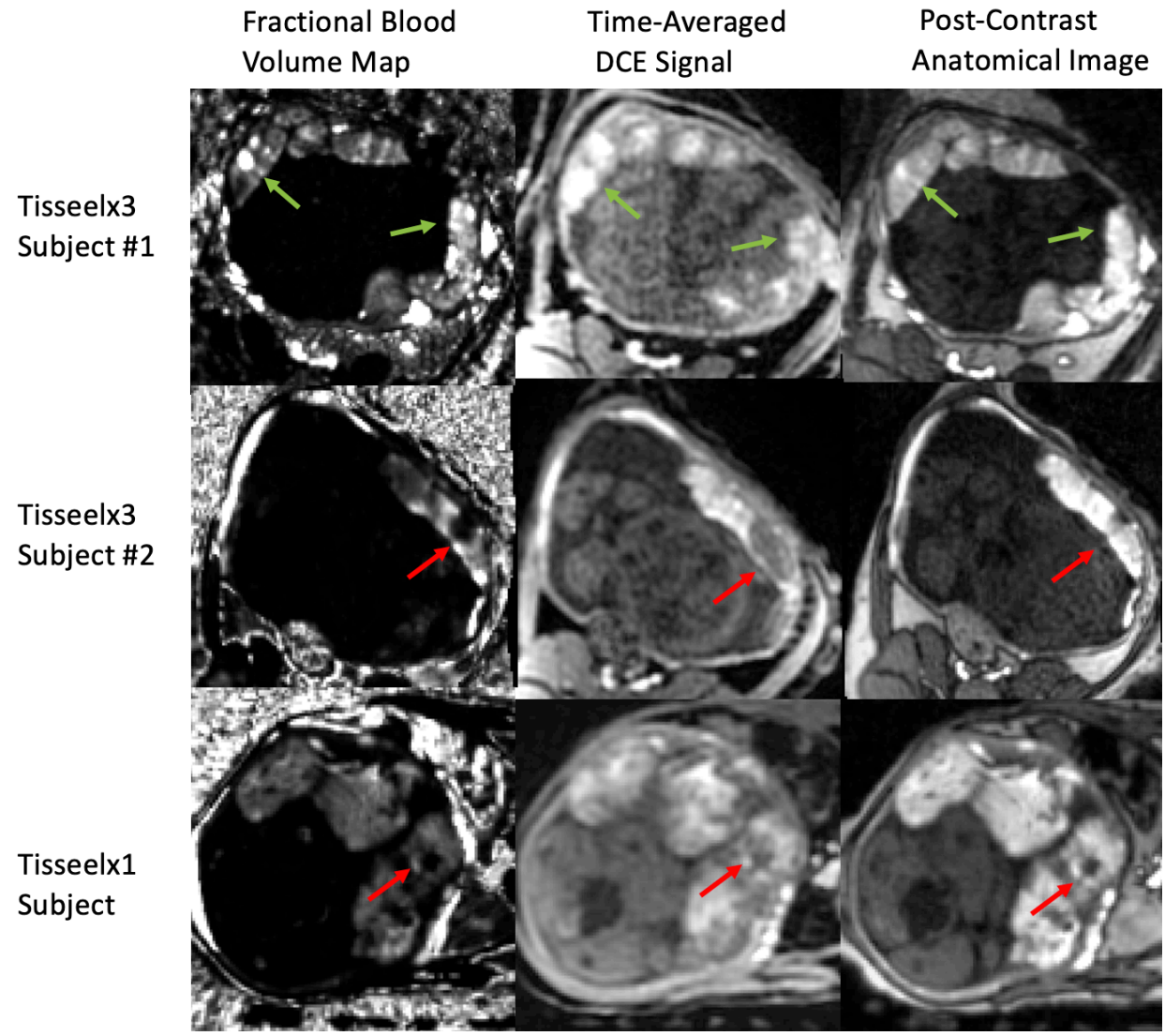

Figure 33. Co-registered Fractional blood volume map (left column), time-averaged dynamic contrast enhanced (DCE) signal (middle column), and T1-weighted post-contrast anatomical image (right column) used for blood volume calculation.

Green arrows show areas of enhanced signal, whereas the red arrows show lower image signal and lower blood volume, possibly suggesting tissue infarction and necrosis.

Figure 34 shows heat maps of fractional blood volume (left column) and contrast arrival time maps (right column) of the three subjects. Generally, regions of high blood volumes correspond to regions of low arrival time, meaning the contrast reaches 50% of maximum DCE signal faster. The Tisseelx3 subject #2 has lower blood volume in the slice shown, and correspondingly the arrival times are longer. Tisseelx3 subjects have higher arrival times than the Tisselx1 subject.

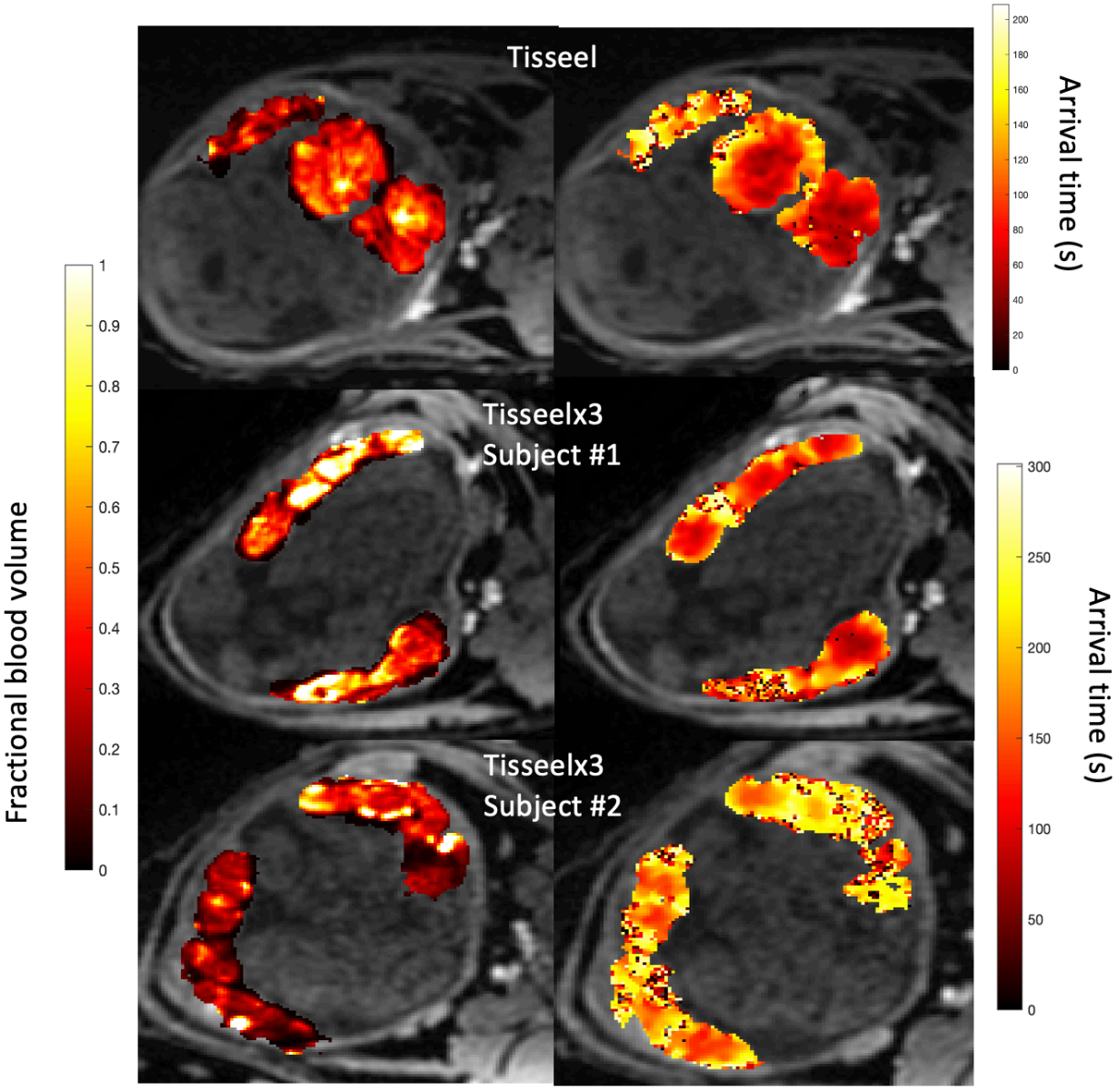

Figure 34. Heat maps of fractional blood volume (left column) and contrast arrival time maps (right column) of the three subjects.

Generally, regions of high blood volumes correspond to regions of low arrival time, meaning the contrast reaches 50% of maximum DCE signal faster. The slice of the Tisseelx3 subject 2 has lower blood volume, and correspondingly the arrival times are longer.

Figure 35 shows density maps of pixel-wise locally corresponding fractional blood volume (FBV) vs. normalized time-averaged DCE signal (left column) and vs. contrast arrival time (right column). The scale bar on the right shows the density of the scatter plots. There is a generally positive correlation between FBV and the DCE signal; two subjects show a negative trend between FBV and arrival time.

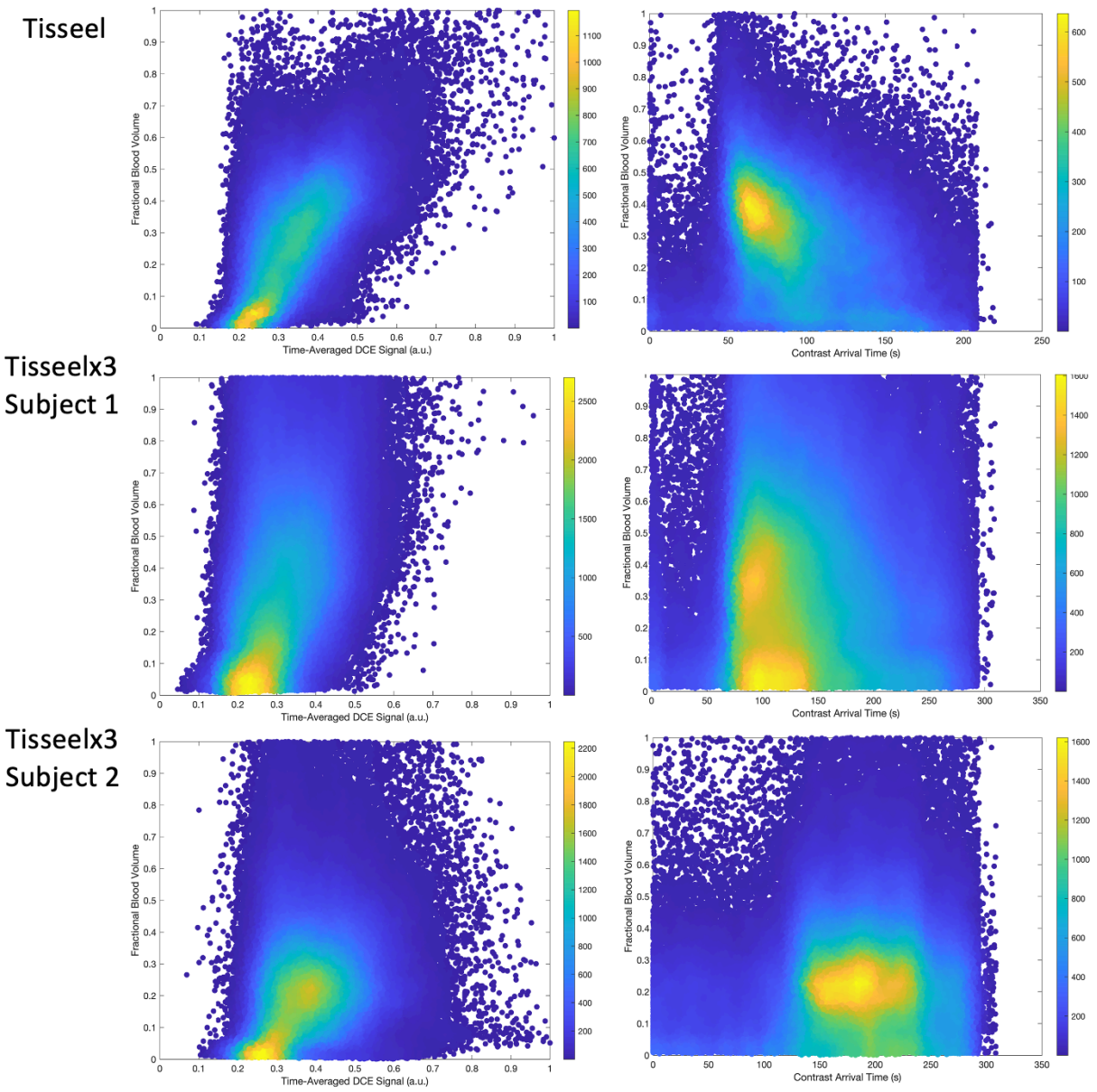

Figure 35. Density maps of pixel-wise locally corresponding fractional blood volume (FBV) vs. normalized time-averaged DCE signal (left column) and vs. contrast arrival time (right column).

The scale bar on the right shows the density of the scatter plots. There is a generally positive correlation between FBV and the DCE signal; two subjects show a negative trend between FBV and arrival time.

6.4 Discussion

This study assesses local placental injury of Tisseel-treated rhesus macaques by co-registering averaged DCE images and fractional blood volume maps. To our knowledge, this is the first study to use multi-modal imaging methods to examine local mal-perfusion areas through deformable image registration. From histopathological analysis through a central slice of the placenta, all three rhesus macaque subjects (one injected with 0.5ml Tisseel and two with 1.5ml Tisseel) in this study exhibit various degrees of tissue infarctions and coagulative necrosis likely due to the Tisseel injection. Note that two other animals went through the single-dose (0.5ml Tisseel) treatment as well but received moderate pathological results, and therefore were excluded from this study due to the lack of low perfusion areas. This suggests a 1.5ml injection could be more effective in creating placental injury due to the underlying placental plasticity.

From co-registered images, we observe local correlations between the DCE signal and blood volume in regions with possible tissue infarctions. Interestingly, the areas of low signal in time-averaged DCE images seem to be larger than post-contrast T1-weighted anatomical images as well as the blood volume maps. This could be due to the impedance of flow in those areas causing longer times for the contrast to arrive. The center of the mal-perfused areas remains “dark” by the time of the T1 post-contrast imaging (~30 mins after DCE), suggesting that the contrast agent could not reach those areas, indicating potential tissue necrosis.

From the arrival time heat maps, we observe longer contrast agent arrival times for the two Tisseel*3 subjects, suggesting potential increased severity of the placental injury. In general, local increases in contrast arrival time correspond to areas with lower blood volume. However, for some areas with zero blood volume (which may correlate to necrotic tissue), contrast arrival time calculation might not be accurately reflected since the contrast never arrives (time = infinity).

Globally across all pixels, such trend was reflected in FBV vs. DCE plots but not as strongly in the FBV vs. arrival time plots. This could be because for some Tisseel-infected non-necrotic regions, the arrival time might be very long due to impeded flow, but the contrast may eventually be present at the time of post-contrast imaging for the FBV calculation, resulting in unaffected FBV measurement. Similar issues with the infinite arrival time for the necrotic tissues may also affect the accuracy of pixel-wise trend fitting.

There are several limitations of this study. First, there is limited number of animals and in-depth statistical analysis is therefore lacking. Each animal has various degrees of placental injury and the extent of each area of infarction in 3-D is unknown since the pathological analysis was done by examining the central slice only. Second, the accuracy of deformable image registration could largely affect the outcome of the more local-based analysis, such as pixel-wise regression fitting. A more established validation algorithm to the accuracy of registration, especially for regions of tissue necrosis, could be of importance. Third, our current algorithm for arrival time calculation is not adapted to areas with no contrast arrival (arrival time = infinity). Therefore, further fine-tuning of our algorithm to reflect those areas is needed.

To mitigate the effects caused by necrotic tissue areas and to provide a sanity check, future study will investigate the accuracy of pixel-wise agreements of multi-modal MRI for control subjects. Subsequently, improvements will be made on registration validation and arrival time algorithm before applying this technique to more subjects.

Chapter 7. Summary and Future Work

7.1 Summary

In this thesis, I present post-processing analysis and measurements for several placental quantitative MRI markers, including arterial spin labeling-based perfusion, T2*, maternal blood volume, and dynamic contrast enhanced MRI-based blood flow, to investigate their potential diagnostic efficacy through various stages of gestation.

Technical feasibility for a novel multi-slice velocity-selective arterial spin labeling (VS-ASL) sequence was demonstrated by measuring placental perfusion in rhesus macaques. At three

gestational timepoints correlating to the three trimesters of pregnancy, perfusion maps were successfully generated for seven rhesus macaques, four of which were infected with Zika virus. A comparison between central slice and overall (8 slices covering whole placenta) perfusion show 20% difference, suggesting the need for volumetric coverage in perfusion measurements. In this study, the sequence development and scanning protocol was established by Dr. Kevin Johnson. I proceeded with perfusion measurements and in depth data analysis, which demonstrated the feasibility of such sequence in an animal model and the advantages of a multi slice ASL approach.

Early gestation (14 weeks, 20 weeks) baseline T2* mapping was conducted for a large human subject cohort (N=97), to assess T2*-based blood oxygen level dependent (BOLD) effect on subjects with gestational complications. Stable muscle ROI T2* across the two gestation ages suggests the robustness of the protocol with time. T2* histograms at 14 weeks presented lower mode and higher skewness to the left for the subjects diagnosed with preeclampsia. Scatter plots show trend of lower T2* for subjects with gestational complications; however, at early gestation, such trend might be subject-specific due to the underlying early developmental factors at play. This work expands from a previous study by Dr. Ante Zhu, which consists of 36 human subjects from our cohort. I applied the established T2* mapping technique to the entire cohort and performed statistical analysis across all subjects.

A post-processing technique to measure maternal placental blood volume (BV) with variable flip angle T1-mapping was developed in the context of both human and rhesus macaque subjects. BV maps were successfully generated with such framework in a feasibility study for eleven rhesus macaques. Subsequently, human BV results were reported for the first time with three human subjects with fetal growth restriction as a preliminary study. Lastly, this technique was applied to three rhesus macaques with placental vascular injury. Local variations, including areas with low

BV, were observed from 3D BV maps. This suggests potential diagnostic efficacy of BV in the future. In this study, I established the blood volume measurement methodology and analysis workflow for placenta from scratch, including 3D image registration for the VFA volumes for T1 maps as well as the pre- and post-contrast image registration and voxel-wise calculations of blood volumes. I then succesfully applied the approach to three cohorts to demonstrate feasibility of such measurements, as well as its potential diagnostic efficacy.

Dynamic contrast-enhanced (DCE) MRI technique was applied to measure placental blood flow at a cotyledon-specific level for rhesus macaque subjects with placental vascular injury. An improved 3D watershed algorithm was introduced to improve the robustness of cotyledon segmentation. DCE analysis showed significantly lower blood flow, cotyledon volume, and normalized blood flow for animals treated with 1.5ml Tisseel, a fibrin sealant used surgically to stop bleeding. This demonstrates the potential diagnostic efficacy of DCE based blood flow analysis and serves as a potential baseline for future perfusion correlation using arterial spin labeling. This study was based on an established DCE post-processing workflow by Dr. Kai Ludwig, which had been later modified by Dr. Daniel Seiter. I further improved the approach by replacing the2D watershed algorithm with a 3D method to improve robustness in the segmentation of the individual cotyledons. In addition, I modified the flow calculation to be the highest slope (largest derivative) of the signal enhancing curve, rather than the previous slope from linear fitting. This could potentially improve the accuracy of the flow calculation for cases of delayed enhancement.

A deformable registration technique was applied to compare blood volume maps, R1 maps, and contrast agent arrival time maps of three rhesus macaques who demonstrated placental pathology such as tissue necrosis. Correlated areas of mal-perfusion were observed in all three

maps, suggesting data fidelity. Pixel-wise comparison show a trend of positive correlation between fractional blood volume and time-averaged DCE signal, and a trend of negative correlation between fractional blood volume and contrast agent arrival times. Future adjustments might be needed to improve arrival time determination for areas with tissue necrosis. In this work, I applied the deformable registration techniques to the qualitative maps I obtained from previous chapters, and performed local analysis focused on the sites of placental injury.

7.2 Future Work

7.2.1 Cotyledon-Specific Correlations with Pathology: Blood Volume and DCE-MRI

As Chapter 5 suggests, DCE-MRI can measure cotyledon-specific flow parameters, which could allow for more direct comparison with pathology results for the rhesus macaque subjects treated with Tisseel. Current pathology analysis is qualitative (based on pathology report with a central slice of placenta) and unable to offer a cotyledon-to-cotyledon comparison. As a next step, we are collaborating with Logan Keding from the Wisconsin National Primate Research Center to generate a quantitative report that reflects each cotyledon's pathology.

To achieve this, each cotyledon's central slice will be stained for histopathological analysis. Segmentation is then performed to delineate visible placental tissue in that slice, as well as necrotic tissue within the placenta. A ratio between the two segmented areas can give a quantitative overview of the cotyledon's health. Figure 36 shows this workflow.

The 3D-rendered placental volume in-vivo could be hard to match with flattened placental volume ex-vivo, due to the difference of shape once the placenta is birthed. For easier matching, one could apply the established placental flattening algorithm[153], which predicts what the placenta would look like flattened out.

Additionally, with deformable registration between fractional blood volume and DCE signal (introduced in Chapter 6), the segmented cotyledons can be applied to the blood volume maps as well. Therefore, similar comparison and analysis can be done with the blood volume as well.

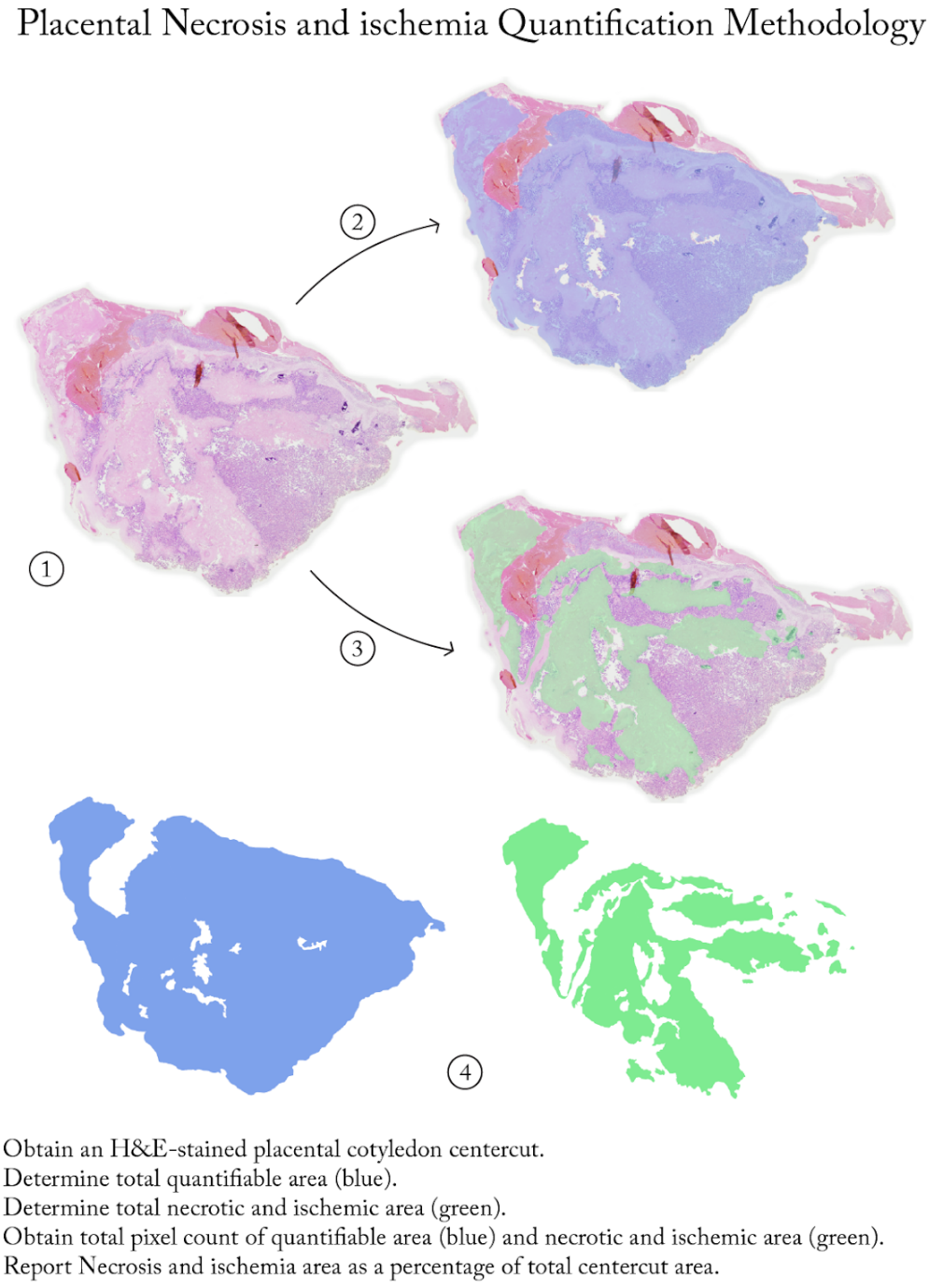

Figure 36. Placental Necrosis and Ischemia Quantification Methodology Workflow. Image courtesy of Logan Keding.

7.2.2 Big-Data Analysis: Placental Shape, Surface Area, Implantation Site, and More

Insufficient placental development has been associated with adverse gestational outcomes such as fetal growth restriction, pre-term birth, and preeclampsia. However, the assessments of naïve placental parameters and their relationship with maternal characteristics (age, race, number of pregnancies, health history, etc.), are currently lacking, especially in the context of a large cohort representative of general population. A study recently published by Sletner et al from a multi-ethnic population of 823 subjects reports smaller surface area within the Asian population, as well as an association between placental thickness and maternal fat mass[154]. With our large cohort of ~100 subjects, it could be of importance to investigate and compare these placental parameters and their potential relationship to maternal characteristics.

Placenta accreta is a condition where the placenta grows deeply into the uterine wall[155]. Recently, Kliewer et al from our institution has used Ferumoxytol contrast agent to identify signs of placenta accrete by looking at the placental structure and vascularity[126,148]. It is therefore of great interest to explore placental implantation site and geometry to assess potential diagnostic and prediction efficacy for placenta accreta. To achieve this, a preliminary study has collected placental structural data with a single shot fast spin sequence to characterize the placentation site. For each scan, the placentation site was characterized by position in 3 ways: anterior or posterior, left or right, and superior or inferior, by dividing the uterus in half as shown in Figure 37. The placenta shown would be classified as an anterior, right, inferior placentation site. Future study would be to expand this analysis for our cohort of ~100 subjects.

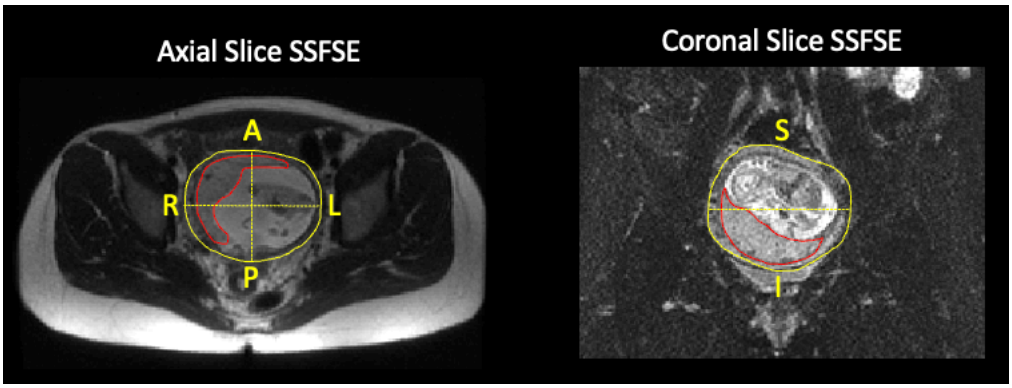

Figure 37. Placental implantation site characterization. Image courtesy of Dr. Philip Corrado.

7.2.3 Quantifying Placental Inflammation using T2* Mapping

Iron oxide nanoparticles, such as ferumoxytol contrast agent, has be shown be taken up by macrophages in tissue as an inflammatory response[156]. This iron deposition can be assessed using T2* mapping, as ferumoxytol causes a regional shortening of T2* [157]. In Chapter 5, we introduced Macrophage chemoattractant protein 1 (MCP1) that could induce an inflammatory response in rhesus macaque placenta[158]. One day after each MRI scan with ferumoxytol infusion, the rhesus macaques went through another scan to obtain the T2* map for analysis of iron deposition and ferumoxytol retention in the decidua. We hypothesize regionally lower T2* (higher R2*) values in animals treated with MCP1 comparing to the control subjects. This study could further investigate the diagnostic efficacy of T2* mapping as a potential quantitative MRI marker to assess tissue inflammatory response.

7.2.4 Assessing the Capability of Fe-Enhanced MRA to Visualize Maternal Placental Vasculature

Contrast-enhanced MR angiography allows for the potential of clear visualization of placental vasculature. Current placental MRA studies include an ex-vivo contrast-enhanced MRA with gadolinium-based contrast agents[159,160], an in-vivo human placental MRA without contrast agent[160], and a rhesus macaque MRA study done by our lab using ferumoxytol contrast agent[161]: Macdonald et al. investigated the capability of ferumoxytol-enhanced MRA to visualize uterine and ovarian arteries and veins for 10 rhesus macaques[3].

A high-resolution, spoiled gradient, 3D ultrashort echo time (UTE) sequence[162] using a center out radial trajectory (TR/TE=4.4/0.1ms; FA=10°; FOV=18x18x18cm^3; isotropic spatial resolution=0.5mm, scan time~350s) was used to acquire MRA scans for animals stated in Chapter 5. Complex subtraction (post – pre contrast) processing can be employed to create an angiogram with suppressed background signal from these acquisitions. The maximum intensity projection images can then be scored by an experienced radiologist to assess visibility of the vessels. Analyzed vessels include the ovarian arteries and veins, uterine arteries, and veins, and the blood vessels of the maternal fetal interface[163]. Vessels will be scored on a 3-point grading system (1=not visible; 2=partially visible; 3=fully visible) and the number of placental branch vessel will be recorded. All vessels will be segmented in MIMICs (Materialise, Leuven, Belgium). In addition, placental flattening algorithms could be implemented to display vascular structure as it should be seen ex-vivo after delivery[153].

We expect to see clear rendering of vasculature at the maternal-fetal interface through maximum intensity projection images of the rhesus subjects. Additionally, for some animals treated with blood clot agent (Tisseel), we expect to see minimal signal enhancement in branches

with tissue necrosis. We will obtain radiologist scoring on the vessels covering the placental regions to assess feasibilities of Fe-enhanced MRA to visualize small vessels and possible occlusions. Placental flattening should display vascular branching structures within the intervillous space of the placenta, which could be used as indicators for placental organization and health as anatomical landmark for 3D printing in future projects such as image guided pathology.

Bibliography

1. Siauve N, Chalouhi GE, Deloison B, et al. Functional imaging of the human placenta with magnetic resonance. *Am J Obstet Gynecol*. 2015;213(4 Suppl):S103-14. doi:10.1016/j.ajog.2015.06.045

2. Guttmacher AE, Maddox YT, Spong CY. The Human Placenta Project: placental structure, development, and function in real time. *Placenta*. 2014;35(5):303-304. doi:10.1016/j.placenta.2014.02.012

3. Macdonald JA, Corrado PA, Nguyen SM, et al. Uteroplacental and Fetal 4D Flow MRI in the Pregnant Rhesus Macaque. *J Magn Reson Imaging*. 2019;49(2):534-545. doi:10.1002/jmri.26206

4. Thornburg KL, Marshall N. The placenta is the center of the chronic disease universe. *Am J Obstet Gynecol*. 2015;213(4 Suppl):S14-20. doi:10.1016/j.ajog.2015.08.030

5. Barker DJ. The fetal and infant origins of adult disease. *BMJ*. 1990;301(6761):1111. doi:10.1136/bmj.301.6761.1111

6. Society for Maternal-Fetal Medicine Publications Committee, Berkley E, Chauhan SP, Abuhamad A. Doppler assessment of the fetus with intrauterine growth restriction. *Am J Obstet Gynecol*. 2012;206(4):300-308. doi:10.1016/j.ajog.2012.01.022

7. Sørensen A, Hutter J, Seed M, Grant PE, Gowland P. T2*-weighted placental MRI: basic research tool or emerging clinical test for placental dysfunction? *Ultrasound in Obstetrics and Gynecology*. 2020;55(3):293-302. doi:10.1002/uog.20855

8. Ho AEP, Hutter J, Jackson LH, et al. T2∗ Placental Magnetic Resonance Imaging in Preterm Preeclampsia: An Observational Cohort Study. *Hypertension*. 2020;75(6):1523-1531. doi:10.1161/HYPERTENSIONAHA.120.14701

9. Hutter J, Slator PJ, Jackson L, et al. Multi-modal functional MRI to explore placental function over gestation. *Magn Reson Med*. 2019;81(2):1191-1204. doi:10.1002/mrm.27447

10. Derwig I, Lythgoe DJ, Barker GJ, et al. Association of placental perfusion, as assessed by magnetic resonance imaging and uterine artery Doppler ultrasound, and its relationship to pregnancy outcome. *Placenta*. 2013;34(10):885-891. doi:10.1016/j.placenta.2013.07.006

11. Abaci Turk E, Stout JN, Ha C, et al. Placental MRI: Developing Accurate Quantitative Measures of Oxygenation. *Top Magn Reson Imaging*. 2019;28(5):285-297. doi:10.1097/RMR.0000000000000221

12. Zhu A, Reeder SB, Johnson KM, et al. Evaluation of a motion-robust 2D chemical shift-encoded technique for R2* and field map quantification in ferumoxytol-enhanced MRI of the placenta in pregnant rhesus macaques. *Journal of Magnetic Resonance Imaging*. 2020;51(2):580-592. doi:10.1002/jmri.26849

13. Burton GJ, Jauniaux E. Pathophysiology of placental-derived fetal growth restriction. *Am J Obstet Gynecol*. 2018;218(2S):S745-S761. doi:10.1016/j.ajog.2017.11.577

14. Barker D, Osmond C, Grant S, et al. Maternal cotyledons at birth predict blood pressure in childhood. *Placenta*. 2013;34(8):672-675. doi:10.1016/j.placenta.2013.04.019

15. Schabel MC, Roberts VHJ, Lo JO, et al. Functional imaging of the nonhuman primate Placenta with endogenous blood oxygen level–dependent contrast. *Magn Reson Med*. 2016;76(5):1551-1562. doi:10.1002/mrm.26052

16. Hirsch AJ, Roberts VHJ, Grigsby PL, et al. Zika virus infection in pregnant rhesus macaques causes placental dysfunction and immunopathology. *Nat Commun*. 2018;9(1):263. doi:10.1038/s41467-017-02499-9

17. Bernstein IM, Horbar JD, Badger GJ, Ohlsson A, Golan A. Morbidity and mortality among very-low-birth-weight neonates with intrauterine growth restriction. The Vermont Oxford Network. *Am J Obstet Gynecol*. 2000;182(1 Pt 1):198-206. doi:10.1016/s0002-9378(00)70513-8

18. Hack M, Flannery DJ, Schluchter M, Cartar L, Borawski E, Klein N. Outcomes in young adulthood for very-low-birth-weight infants. *N Engl J Med*. 2002;346(3):149-157. doi:10.1056/NEJMoa010856

19. Barker DJP, Eriksson JG, Forsén T, Osmond C. Fetal origins of adult disease: strength of effects and biological basis. *Int J Epidemiol*. 2002;31(6):1235-1239. doi:10.1093/ije/31.6.1235

20. Ingram E, Morris D, Naish J, Myers J, Johnstone E. MR Imaging Measurements of Altered Placental Oxygenation in Pregnancies Complicated by Fetal Growth Restriction. *Radiology*. 2017;285(3):953-960. doi:10.1148/radiol.2017162385

21. Kelly AC, Powell TL, Jansson T. Placental function in maternal obesity. *Clin Sci (Lond)*. 2020;134(8):961-984. doi:10.1042/CS20190266

22. Coles C. Critical Periods for Prenatal Alcohol Exposure: Evidence From Animal and Human Studies. *Alcohol Health Res World*. 1994;18(1):22-29.

23. Hong S, Le Y, Lio KU, Zhang T, Zhang Y, Zhang N. Performance comparison of ultrasonography and magnetic resonance imaging in their diagnostic accuracy of placenta accreta spectrum disorders: a systematic review and meta-analysis. *Insights Imaging*. 2022;13(1):50. doi:10.1186/s13244-022-01192-w

24. Ludwig KD, Fain SB, Nguyen SM, et al. Perfusion of the placenta assessed using arterial spin labeling and ferumoxytol dynamic contrast enhanced magnetic resonance imaging in the rhesus macaque. *Magn Reson Med*. 2019;81(3):1964-1978. doi:10.1002/mrm.27548

25. Huen I, Morris DM, Wright C, et al. R1 and R2* changes in the human placenta in response to maternal oxygen challenge. *Magn Reson Med*. 2013;70(5):1427-1433. doi:10.1002/mrm.24581

26. Liu D, Shao X, Danyalov A, et al. Human Placenta Blood Flow During Early Gestation With Pseudocontinuous Arterial Spin Labeling MRI. *J Magn Reson Imaging*. 2020;51(4):1247-1257. doi:10.1002/jmri.26944

27. Roberts JM, Escudero C. The placenta in preeclampsia. *Pregnancy Hypertens*. 2012;2(2):72-83. doi:10.1016/j.preghy.2012.01.001

28. Yurttutan N, Bakacak M, Kızıldağ B. Comparison of the T2-star Values of Placentas Obtained from Pre-eclamptic Patients with Those of a Control Group: an Ex-vivo Magnetic Resonance Imaging Study. *Balkan Med J*. 2017;34(5):412-416. doi:10.4274/balkanmedj.2016.1472

29. Ingram E, Morris D, Naish J, Myers J, Johnstone E. MR imaging measurements of altered placental oxygenation in pregnancies complicated by fetal growth restriction. *Radiology*. 2017;285(3):953-960. doi:10.1148/radiol.2017162385

30. Sinding M, Peters DA, Frøkjær JB, et al. Placental magnetic resonance imaging T2∗ measurements in normal pregnancies and in those complicated by fetal growth restriction. *Ultrasound in Obstetrics and Gynecology*. 2016;47(6):748-754. doi:10.1002/uog.14917

31. Turk EA, Luo J, Gagoski B, et al. Spatiotemporal alignment of in utero BOLD-MRI series. *J Magn Reson Imaging*. 2017;46(2):403-412. doi:10.1002/jmri.25585

32. Siauve N, Chalouhi GE, Deloison B, et al. Functional imaging of the human placenta with magnetic resonance. *Am J Obstet Gynecol*. 2015;213(4 Suppl):S103-14. doi:10.1016/j.ajog.2015.06.045

33. Ginosar Y, Gielchinsky Y, Nachmansson N, et al. BOLD-MRI demonstrates acute placental and fetal organ hypoperfusion with fetal brain sparing during hypercapnia. *Placenta*. 2018;63:53-60. doi:10.1016/j.placenta.2017.09.005

34. Luo J, Abaci Turk E, Bibbo C, et al. In Vivo Quantification of Placental Insufficiency by BOLD MRI: A Human Study. *Sci Rep*. 2017;7(1):3713. doi:10.1038/s41598-017-03450-0

35. Andersen AS, Anderson KB, Hansen DN, et al. Placental MRI: Longitudinal relaxation time (T1) in appropriate and small for gestational age pregnancies. *Placenta*. 2021;114:76-82. doi:10.1016/j.placenta.2021.08.057

36. Armstrong T, Liu D, Martin T, et al. HHS Public Access. 2020;49(1):291-303. doi:10.1002/jmri.26203.3D

37. Hutter D, Kingdom J, Jaeggi E. Causes and mechanisms of intrauterine hypoxia and its impact on the fetal cardiovascular system: a review. *Int J Pediatr*. 2010;2010:401323. doi:10.1155/2010/401323

38. Detre JA, Zhang W, Roberts DA, et al. Tissue specific perfusion imaging using arterial spin labeling. *NMR Biomed*. 1994;7(1-2):75-82. doi:10.1002/nbm.1940070112

39. Buchbender S, Obenauer S, Mohrmann S, et al. Arterial spin labelling perfusion MRI of breast cancer using FAIR TrueFISP: initial results. *Clin Radiol*. 2013;68(3):e123-7. doi:10.1016/j.crad.2012.10.011

40. Gowland PA, Francis ST, Duncan KR, et al. In vivo perfusion measurements in the human placenta using echo planar imaging at 0.5 T. *Magn Reson Med*. 1998;40(3):467-473. doi:10.1002/mrm.1910400318

41. Francis ST, Duncan KR, Moore RJ, Baker PN, Johnson IR, Gowland PA. Non-invasive mapping of placental perfusion. *Lancet*. 1998;351(9113):1397-1399. doi:10.1016/S0140-6736(97)07089-X

42. Hernandez-Garcia L, Jahanian H, Greenwald MK, Zubieta JK, Peltier SJ. Real-time functional MRI using pseudo-continuous arterial spin labeling. *Magn Reson Med*. 2011;65(6):1570-1577. doi:10.1002/mrm.22922

43. Shao X, Liu D, Martin T, et al. Measuring human placental blood flow with multidelay 3D GRASE pseudocontinuous arterial spin labeling at 3T. *J Magn Reson Imaging*. 2018;47(6):1667-1676. doi:10.1002/jmri.25893

44. Wong EC, Cronin M, Wu WC, Inglis B, Frank LR, Liu TT. Velocity-selective arterial spin labeling. *Magn Reson Med*. 2006;55(6):1334-1341. doi:10.1002/mrm.20906

45. Zun Z, Limperopoulos C. Placental perfusion imaging using velocity-selective arterial spin labeling. *Magn Reson Med*. 2018;80(3):1036-1047. doi:10.1002/mrm.27100

46. Harteveld AA, Hutter J, Franklin SL, et al. Systematic evaluation of velocity-selective arterial spin labeling settings for placental perfusion measurement. *Magn Reson Med*. 2020;84(4):1828-1843. doi:10.1002/mrm.28240

47. Zun Z, Zaharchuk G, Andescavage NN, Donofrio MT, Limperopoulos C. Non-Invasive Placental Perfusion Imaging in Pregnancies Complicated by Fetal Heart Disease Using Velocity-Selective Arterial Spin Labeled MRI. *Sci Rep*. 2017;7(1):16126. doi:10.1038/s41598-017-16461-8

48. Oh KY, Roberts VHJ, Schabel MC, Grove KL, Woods M, Frias AE. Gadolinium Chelate Contrast Material in Pregnancy: Fetal Biodistribution in the Nonhuman Primate. *Radiology*. 2015;276(1):110-118. doi:10.1148/radiol.15141488

49. Tanaka YO, Sohda S, Shigemitsu S, Niitsu M, Itai Y. High temporal resolution dynamic contrast MRI in a high risk group for placenta accreta. *Magn Reson Imaging*. 2001;19(5):635-642. doi:10.1016/s0730-725x(01)00388-5

50. Lo JO, Roberts VHJ, Schabel MC, et al. Novel Detection of Placental Insufficiency by Magnetic Resonance Imaging in the Nonhuman Primate. *Reproductive Sciences*. 2018;25(1):64-73. doi:10.1177/1933719117699704

51. Bashir MR, Bhatti L, Marin D, Nelson RC. Emerging applications for ferumoxytol as a contrast agent in MRI. *J Magn Reson Imaging*. 2015;41(4):884-898. doi:10.1002/jmri.24691

52. Vasanawala SS, Nguyen KL, Hope MD, et al. Safety and technique of ferumoxytol administration for MRI. *Magn Reson Med*. 2016;75(5):2107-2111. doi:10.1002/mrm.26151

53. Hope MD, Hope TA, Zhu C, et al. Vascular Imaging With Ferumoxytol as a Contrast Agent. *AJR Am J Roentgenol*. 2015;205(3):W366-73. doi:10.2214/AJR.15.14534

54. Toth GB, Varallyay CG, Horvath A, et al. Current and potential imaging applications of ferumoxytol for magnetic resonance imaging. *Kidney Int*. 2017;92(1):47-66. doi:10.1016/j.kint.2016.12.037

55. Nguyen KL, Yoshida T, Kathuria-Prakash N, et al. Multicenter Safety and Practice for Off-Label Diagnostic Use of Ferumoxytol in MRI. *Radiology*. 2019;293(3):554-564. doi:10.1148/radiol.2019190477

56. FDA. No Title. U.S. Food and Drug Administration - FDA Drug Safety Communication: FDA strengthens warnings and changes prescribing instructions to decrease the risk of serious allergic reactions with anemia drug Feraheme (ferumoxytol).

57. Starekova J, Nagle S, Schieber M, Reeder SB, Meduri V. Ferumoxytol-Enhanced Pulmonary MRA in Pregnancy: Evaluation of Initial Safety and Image Quality. In: *Proc. Intl. Soc. Mag. Reson. Med.* ; 2021.

58. Badachhape AA, Devkota L, Stupin I V, et al. Nanoparticle Contrast-enhanced T1-Mapping Enables Estimation of Placental Fractional Blood Volume in a Pregnant Mouse Model. *Sci Rep*. 2019;9(1):18707. doi:10.1038/s41598-019-55019-8

59. Gaglia JL, Harisinghani M, Aganj I, et al. Noninvasive mapping of pancreatic inflammation in recent-onset type-1 diabetes patients. *Proc Natl Acad Sci U S A*. 2015;112(7):2139-2144. doi:10.1073/pnas.1424993112

60. Slator PJ, Hutter J, Palombo M, et al. Combined diffusion-relaxometry MRI to identify dysfunction in the human placenta. *Magn Reson Med*. 2019;82(1):95-106. doi:10.1002/mrm.27733

61. Schabel MC, Roberts VHJ, Lo JO, et al. Functional imaging of the nonhuman primate Placenta with endogenous blood oxygen level-dependent contrast. *Magn Reson Med*. 2016;76(5):1551-1562. doi:10.1002/mrm.26052

62. Zhu A, Reeder SB, Johnson KM, et al. Quantitative ferumoxytol-enhanced MRI in pregnancy: A feasibility study in the nonhuman primate. *Magn Reson Imaging*. 2020;65:100-108. doi:10.1016/j.mri.2019.10.006

63. Hutter J, Jackson L, Ho A, et al. The use of functional placental magnetic resonance imaging for assessment of the placenta after prolonged preterm rupture of the membranes in vivo: A pilot study. *Acta Obstet Gynecol Scand*. 2021;100(12):2244-2252. doi:10.1111/AOGS.14267

64. Derwig I, Barker GJ, Poon L, et al. Association of placental T2 relaxation times and uterine artery Doppler ultrasound measures of placental blood flow. *Placenta*. 2013;34(6):474-479. doi:10.1016/J.PLACENTA.2013.03.005

65. Yurttutan N, Bakacak M, Kızıldağ B. Comparison of the T2-star Values of Placentas Obtained from Pre-eclamptic Patients with Those of a Control Group: an Ex-vivo Magnetic Resonance Imaging Study. *Balkan Med J*. 2017;34(5):412-416. doi:10.4274/BALKANMEDJ.2016.1472

66. Poulsen SS, Sinding M, Hansen DN, Peters DA, Frøkjær JB, Sørensen A. Placental T2* estimated by magnetic resonance imaging and fetal weight estimated by ultrasound in the prediction of birthweight differences in dichorionic twin pairs. *Placenta*. 2019;78:18-22. doi:10.1016/J.PLACENTA.2019.02.005

67. Karpenko AA, Cheban A V, Rabtsun AA, et al. Fibrin Sealant TISSEEL Lyo as a haemostatic agent in vascular surgery: Results of randomized, controlled, patient-blinded, multicentre clinical study in the Russian population. *Sci Prog*. 2023;106(3):368504231182834. doi:10.1177/00368504231182834

68. Siauve N, Chalouhi GE, Deloison B, et al. Functional imaging of the human placenta with magnetic resonance. *Am J Obstet Gynecol*. 2015;213(4 Suppl):S103-14. doi:10.1016/j.ajog.2015.06.045

69. Jabehdar Maralani P, Kapadia A, Liu G, et al. Canadian Association of Radiologists Recommendations for the Safe Use of MRI During Pregnancy. *Can Assoc Radiol J*. 2022;73(1):56-67. doi:10.1177/08465371211015657

70. Garcia-Bournissen F, Shrim A, Koren G. Safety of gadolinium during pregnancy. *Can Fam Physician*. 2006;52(3):309-310.

71. Arthuis C, Jungelson A, Taso M, et al. Evaluation of the reproducibility and confounders of fair ASL placenta perfusion measurement in normal pregnancies. *Gynécologie Obstétrique Fertilité & Sénologie* . 2022;50(5):437. doi:10.1016/j.gofs.2022.02.032

72. Liu D, Shao X, Danyalov A, et al. Human Placenta Blood Flow During Early Gestation With Pseudocontinuous Arterial Spin Labeling MRI. *J Magn Reson Imaging*. 2020;51(4):1247-1257. doi:10.1002/jmri.26944

73. Seiter D, Chen R, Ludwig K, et al. Chapter 4: Velocity-Selective Arterial Spin Labeling Perfusion Measurements in 2nd Trimester Human Placenta with Varying BMI. In: *Proc 30th Annual Meeting ISMRM (2022)*. ; 2022.

74. Seiter DP, Nguyen SM, Morgan TK, et al. Ferumoxytol Dynamic Contrast Enhanced Magnetic Resonance Imaging Identifies Altered Placental Cotyledon Perfusion in Rhesus Macaques. *Biol Reprod*. Published online August 26, 2022. doi:10.1093/biolre/ioac168

75. Hutter J, Slator PJ, Jackson L, et al. Multi-modal functional MRI to explore placental function over gestation. *Magn Reson Med*. 2019;81(2):1191-1204. doi:10.1002/mrm.27447

76. Harteveld AA, Hutter J, Franklin SL, et al. Systematic evaluation of velocity-selective arterial spin labeling settings for placental perfusion measurement. *Magn Reson Med*. 2020;84(4):1828-1843. doi:10.1002/mrm.28240

77. Howell KR, Powell TL. Effects of maternal obesity on placental function and fetal development. *Reproduction*. 2017;153(3):R97-R108. doi:10.1530/REP-16-0495

78. Hutter J, Jackson L, Ho A, et al. T2* relaxometry to characterize normal placental development over gestation in-vivo at 3T. *Wellcome Open Res*. 2019;4:166. doi:10.12688/wellcomeopenres.15451.1

79. Ho A, Chappell LC, Story L, et al. Visual assessment of the placenta in antenatal magnetic resonance imaging across gestation in normal and compromised pregnancies: Observations from a large cohort study. *Placenta*. 2022;117:29-38. doi:10.1016/J.PLACENTA.2021.10.006

80. Abaci Turk E, Stout JN, Ha C, et al. Placental MRI: Developing Accurate Quantitative Measures of Oxygenation. *Topics in Magnetic Resonance Imaging*. 2019;28(5):285-297. doi:10.1097/RMR.0000000000000221

81. Sørensen A, Sinding M. Placental Magnetic Resonance Imaging: A Method to Evaluate Placental Function In Vivo. *Obstet Gynecol Clin North Am*. 2020;47(1):197-213. doi:10.1016/J.OGC.2019.10.009

82. Schabel MC, Roberts VHJ, Gibbins KJ, et al. Quantitative longitudinal T2*mapping for assessing placental function and association with adverse pregnancy outcomes across gestation. *PLoS One*. 2022;17(7 July). doi:10.1371/journal.pone.0270360

83. Hansen DN, Sinding M, Petersen A, et al. T2*-weighted placental magnetic resonance imaging: a biomarker of placental dysfunction in small-for-gestational-age pregnancies. *Am J Obstet Gynecol MFM*. 2022;4(3). doi:10.1016/j.ajogmf.2022.100578

84. Sinding M, Sørensen A, Hansen DN, Peters DA, Frøkjær JB, Petersen AC. T2* weighted placental MRI in relation to placental histology and birth weight. *Placenta*. 2021;114:52-55. doi:10.1016/J.PLACENTA.2021.07.304

85. Steinweg JK, Hui GTY, Pietsch M, et al. T2* placental MRI in pregnancies complicated with fetal congenital heart disease. *Placenta*. 2021;108:23-31. doi:10.1016/J.PLACENTA.2021.02.015

86. Anderson KB, Andersen AS, Hansen DN, et al. Placental transverse relaxation time (T2) estimated by MRI: Normal values and the correlation with birthweight. *Acta Obstet Gynecol Scand*. 2021;100(5):934-940. doi:10.1111/aogs.14057

87. Zun Z, Kapse K, Quistorff J, et al. Feasibility of QSM in the human placenta. *Magn Reson Med*. 2021;85(3):1272-1281. doi:10.1002/MRM.28502

88. Baadsgaard K, Hansen DN, Peters DA, Fr JB, Sinding M, Anne S. T2 * weighted fetal MRI and the correlation with placental dysfunction. *Placenta*. 2023;131(December 2022):90-97. doi:10.1016/j.placenta.2022.12.002

89. Wright C, Morris DM, Baker PN, et al. Magnetic resonance imaging relaxation time measurements of the placenta at 1.5 T. *Placenta*. 2011;32(12):1010-1015. doi:10.1016/j.placenta.2011.07.008

90. Ingram E, Morris D, Naish J, Myers J, Johnstone E. MR imaging measurements of altered placental oxygenation in pregnancies complicated by fetal growth restriction. *Radiology*. 2017;285(3):953-960. doi:10.1148/radiol.2017162385

91. Sørensen A, Hutter J, Seed M, Grant PE, Gowland P. T2*-weighted placental MRI: basic research tool or emerging clinical test for placental dysfunction? *Ultrasound in Obstetrics and Gynecology*. 2020;55(3):293-302. doi:10.1002/uog.20855

92. Hutter J, Jackson L, Ho A, et al. T2* relaxometry to characterize normal placental development over gestation in-vivo at 3T. *Wellcome Open Res*. 2019;4:166. doi:10.12688/wellcomeopenres.15451.1

93. Matthias Christian Schabel , Victoria H.J. Roberts , D. Monica Rincon , Jessica Gaffney , Jamie O Lo , Karen J Gibbins N, 1 2 3 4 3 4 4, Blue , Glen R Morrell , Christopher D Kroenke , Robert M Silver and AEF, 4 5 6 7 5. A Longitudinal Multisite Study of Endogenous BOLD MRI In Human Pregnancies. In: John Wiley and Sons Inc; 2020.

94. Ho AEP, Hutter J, Jackson LH, et al. T2∗ Placental Magnetic Resonance Imaging in Preterm Preeclampsia: An Observational Cohort Study. *Hypertension*. 2020;75(6):1523-1531. doi:10.1161/HYPERTENSIONAHA.120.14701

95. Armstrong T, Liu D, Martin T, et al. 3D R2* mapping of the placenta during early gestation using free-breathing multiecho stack-of-radial MRI at 3T. *Journal of Magnetic Resonance Imaging*. 2019;49(1):291-303. doi:10.1002/jmri.26203

96. Sinding M, Peters DA, Frøkjær JB, et al. Placental magnetic resonance imaging T2∗ measurements in normal pregnancies and in those complicated by fetal growth restriction. *Ultrasound in Obstetrics and Gynecology*. 2016;47(6):748-754. doi:10.1002/uog.14917

97. Ho A, Hutter J, Slator P, et al. Placental magnetic resonance imaging in chronic hypertension: A case-control study. *Placenta*. 2021;104:138-145. doi:10.1016/j.placenta.2020.12.006

98. Steinweg JK, Hui GTY, Pietsch M, et al. T2* placental MRI in pregnancies complicated with fetal congenital heart disease. *Placenta*. 2021;108:23-31. doi:10.1016/j.placenta.2021.02.015

99. Ho AEP, Hutter J, Jackson LH, et al. T2* Placental Magnetic Resonance Imaging in Preterm Preeclampsia: An Observational Cohort Study. *Hypertension*. 2020;75(6):1523-1531. doi:10.1161/HYPERTENSIONAHA.120.14701

100. Sinding M, Peters DA, Frøkjær JB, et al. Prediction of low birth weight: Comparison of placental T2* estimated by MRI and uterine artery pulsatility index. *Placenta*. 2017;49:48-54. doi:10.1016/j.placenta.2016.11.009

101. Sinding M, Peters DA, Frøkjær JB, et al. Prediction of low birth weight: Comparison of placental T2* estimated by MRI and uterine artery pulsatility index. *Placenta*. 2017;49:48-54. doi:10.1016/j.placenta.2016.11.009

102. He J, Chen Z, Chen C, Liu P. Comparative study of placental T2* and intravoxel incoherent motion in the prediction of fetal growth restriction. *Placenta*. 2021;111:47-53. doi:10.1016/J.PLACENTA.2021.06.005

103. Krishnamurthy U, Szalai G, Neelavalli J, et al. Quantitative T2 changes and susceptibility-weighted magnetic resonance imaging in murine pregnancy. *Gynecol Obstet Invest*. 2014;78(1):33-40. doi:10.1159/000362552

104. Stout JN, Liao C, Gagoski B, et al. Quantitative T1 and T2 mapping by magnetic resonance fingerprinting (MRF) of the placenta before and after maternal hyperoxia. *Placenta*. 2021;114:124-132. doi:10.1016/j.placenta.2021.08.058

105. Huen I, Morris DM, Wright C, et al. R1 and R2* changes in the human placenta in response to maternal oxygen challenge. *Magn Reson Med*. 2013;70(5):1427-1433. doi:10.1002/mrm.24581

106. Hutter J, Harteveld AA, Jackson LH, et al. Perfusion and apparent oxygenation in the human placenta (PERFOX). *Magn Reson Med*. 2020;83(2):549-560. doi:10.1002/MRM.27950

107. Slator PJ, Hutter J, Palombo M, et al. Combined diffusion-relaxometry MRI to identify dysfunction in the human placenta. *Magn Reson Med*. 2019;82(1):95-106. doi:10.1002/mrm.27733

108. Hutter J, Slator PJ, Jackson L, et al. Multi-modal functional MRI to explore placental function over gestation. *Magn Reson Med*. 2019;81(2):1191-1204. doi:10.1002/mrm.27447

109. Kameyama KN, Kido A, Himoto Y, et al. What is the most suitable MR signal index for quantitative evaluation of placental function using Half-Fourier acquisition single-shot turbo spin-echo compared with T2-relaxation time? *Acta Radiol*. 2018;59(6):748-754. doi:10.1177/0284185117727786

110. Abaci Turk E, Abulnaga SM, Luo J, et al. Placental MRI: Effect of maternal position and uterine contractions on placental BOLD MRI measurements. *Placenta*. 2020;95:69-77. doi:10.1016/j.placenta.2020.04.008

111. Abaci Turk E, Stout JN, Feldman HA, et al. Change in T2* measurements of placenta and fetal organs during Braxton Hicks contractions. *Placenta*. 2022;128:69-71. doi:10.1016/J.PLACENTA.2022.08.011

112. Hutter J, Kohli V, Dellschaft N, et al. Dynamics of T2* and deformation in the placenta and myometrium during pre-labour contractions. *Sci Rep*. 2022;12(1). doi:10.1038/S41598-022-22008-3

113. Yushkevich PA, Piven J, Hazlett HC, et al. User-guided 3D active contour segmentation of anatomical structures: significantly improved efficiency and reliability. *Neuroimage*. 2006;31(3):1116-1128. doi:10.1016/j.neuroimage.2006.01.015

114. Zhu A, Starekova J, Batan T, et al. Preliminary Study on the Longitudinal T2*-based BOLD Placental MRI in Obese Pregnant Human Subjects. In: *Proc 28th Annual Meeting ISMRM*. ; 2019.

115. Schabel MC, Roberts VHJ, Gibbins KJ, et al. Quantitative longitudinal T2* mapping for assessing placental function and association with adverse pregnancy outcomes across gestation. *PLoS One*. 2022;17(7):e0270360. doi:10.1371/journal.pone.0270360

116. Brosens I, Pijnenborg R, Vercruysse L, Romero R. The "Great Obstetrical Syndromes" are associated with disorders of deep placentation. *Am J Obstet Gynecol*. 2011;204(3):193-201. doi:10.1016/j.ajog.2010.08.009

117. Nguyen SM, Wiepz GJ, Schotzko M, et al. Impact of ferumoxytol magnetic resonance imaging on the rhesus macaque maternal-fetal interface†. *Biol Reprod*. 2020;102(2):434-444. doi:10.1093/biolre/ioz181

118. Kliewer MA, Bockoven CG, Reeder SB, et al. Ferumoxytol-enhanced MR demonstration of changes to internal placental structure in placenta accreta spectrum: Preliminary findings. *Placenta*. 2023;134:1-8. doi:10.1016/j.placenta.2023.02.003

119. Starekova J, Nagle SK, Schiebler ML, Reeder SB, Meduri VN. Pulmonary MRA During Pregnancy: Early Experience With Ferumoxytol. *J Magn Reson Imaging*. Published online October 31, 2022. doi:10.1002/jmri.28504

120. Chen R, Nguyen S, Murphy M, et al. Longitudinal Placental Blood Volume Measurements on Zika-Infected Rhesus Macaques Using Variable Flip Angle T1 Mapping. In: *Proc 29th Annual Meeting ISMRM*. ; 2021.

121. Chen R, Fain S, Magness R, et al. Maternal Blood Volume Measurements of Human Placenta with Fetal Growth Restriction using Ferumoxytol-Enhanced MRI. In: *Proc 30th Annual Meeting ISMRM*. ; 2022.

122. Deoni SCL. Quantitative relaxometry of the brain. *Top Magn Reson Imaging*. 2010;21(2):101-113. doi:10.1097/RMR.0b013e31821e56d8

123. Colbert CM, Thomas MA, Yan R, et al. Estimation of fractional myocardial blood volume and water exchange using ferumoxytol-enhanced magnetic resonance imaging. *J Magn Reson Imaging*. 2021;53(6):1699-1709. doi:10.1002/jmri.27494

124. Knobloch G, Colgan T, Wiens CN, et al. Relaxivity of Ferumoxytol at 1.5 T and 3.0 T. *Invest Radiol*. 2018;53(5):257-263. doi:10.1097/RLI.0000000000000434

125. Avants BB, Tustison NJ, Stauffer M, Song G, Wu B, Gee JC. The Insight ToolKit image registration framework. *Front Neuroinform*. 2014;8:44. doi:10.3389/fninf.2014.00044

126. Kliewer MA, Bockoven CG, Reeder SB, Bagley AR, Fritsch MK. Ferumoxytol-enhanced magnetic resonance imaging with volume rendering: A new approach for the depiction of internal placental structure in vivo. *Placenta*. 2023;131. doi:10.1016/j.placenta.2022.12.001

127. Hobbs TR, Blue SW, Park BS, Greisel JJ, Conn PM, Pau FKY. Measurement of Blood Volume in Adult Rhesus Macaques (Macaca mulatta). *J Am Assoc Lab Anim Sci*. 2015;54(6):687-693.

128. Hytten F. Blood volume changes in normal pregnancy. *Clin Haematol*. 1985;14(3):601-612.

129. Soma-Pillay P, Nelson-Piercy C, Tolppanen H, Mebazaa A. Physiological changes in pregnancy. *Cardiovasc J Afr*. 2016;27(2):89-94. doi:10.5830/CVJA-2016-021

130. Cheng JY, Hanneman K, Zhang T, et al. Comprehensive motion-compensated highly accelerated 4D flow MRI with ferumoxytol enhancement for pediatric congenital heart disease. *J Magn Reson Imaging*. 2016;43(6):1355-1368. doi:10.1002/jmri.25106

131. Luhar A, Khan S, Finn JP, et al. Contrast-enhanced magnetic resonance venography in pediatric patients with chronic kidney disease: initial experience with ferumoxytol. *Pediatr Radiol*. 2016;46(9):1332-1340. doi:10.1007/s00247-016-3605-z

132. Frias AE, Schabel MC, Roberts VHJ, et al. Using dynamic contrast-enhanced MRI to quantitatively characterize maternal vascular organization in the primate placenta. *Magn Reson Med*. 2015;73(4):1570-1578. doi:10.1002/mrm.25264

133. Barry PA, Lockridge KM, Salamat S, et al. Nonhuman primate models of intrauterine cytomegalovirus infection. *ILAR J*. 2006;47(1):49-64. doi:10.1093/ilar.47.1.49

134. Ollion J, Cochennec J, Loll F, Escudé C, Boudier T. TANGO: A generic tool for high-throughput 3D image analysis for studying nuclear organization. *Bioinformatics*. 2013;29(14). doi:10.1093/bioinformatics/btt276

135. Lo JO, Roberts VHJ, Schabel MC, et al. Novel Detection of Placental Insufficiency by Magnetic Resonance Imaging in the Nonhuman Primate. *Reprod Sci*. 2018;25(1):64-73. doi:10.1177/1933719117699704

136. Harvey A, Montezano AC, Lopes RA, Rios F, Touyz RM. Vascular Fibrosis in Aging and Hypertension: Molecular Mechanisms and Clinical Implications. *Can J Cardiol*. 2016;32(5):659-668. doi:10.1016/j.cjca.2016.02.070

137. Wardinger JE, Ambati S. *Placental Insufficiency*.; 2023.

138. Roberts VHJ, Räsänen JP, Novy MJ, et al. Restriction of placental vasculature in a non-human primate: A unique model to study placental plasticity. *Placenta*. 2012;33(1):73-76. doi:10.1016/j.placenta.2011.10.003

139. Redline RW. Classification of placental lesions. *Am J Obstet Gynecol*. 2015;213(4):S21-S28. doi:10.1016/j.ajog.2015.05.056

140. Sadick M, Richers J, Tuschy B, Schad LR, Schoenberg SO, Zöllner FG. Feasibility of quantitative MR-perfusion imaging to monitor treatment response after uterine artery embolization (UAE) in symptomatic uterus fibroids. *Magn Reson Imaging*. 2019;59:31-38. doi:10.1016/j.mri.2019.02.008

141. Sadick M, Hofmann L, Weiß C, Tuschy B, Schönberg SO, Zöllner FG. Long-term evaluation of uterine fibroid embolisation using MRI perfusion parameters and patient questionnaires: preliminary results. *BMC Med Imaging*. 2022;22(1):214. doi:10.1186/s12880-022-00926-y

142. Roberts VHJ, Castro JN, Wessel BM, Conrad DF, Lewis AD, Lo JO. Rhesus macaque fetal and placental growth demographics: A resource for laboratory animal researchers. *Am J Primatol*. Published online 2023. doi:10.1002/ajp.23526

143. Brosens I, Puttemans P, Benagiano G. Placental bed research: I. The placental bed: from spiral arteries remodeling to the great obstetrical syndromes. *Am J Obstet Gynecol*. 2019;221(5):437-456. doi:10.1016/j.ajog.2019.05.044

144. Qu H, Khalil RA. Vascular mechanisms and molecular targets in hypertensive pregnancy and preeclampsia. *Am J Physiol Heart Circ Physiol*. 2020;319(3):H661-H681. doi:10.1152/ajpheart.00202.2020

145. Aplin JD, Myers JE, Timms K, Westwood M. Tracking placental development in health and disease. *Nat Rev Endocrinol*. 2020;16(9):479-494. doi:10.1038/s41574-020-0372-6

146. Abaci Turk E, Stout JN, Ha C, et al. Placental MRI: Developing Accurate Quantitative Measures of Oxygenation. *Top Magn Reson Imaging*. 2019;28(5):285-297. doi:10.1097/RMR.0000000000000221

147. Schabel MC, Roberts VHJ, Lo JO, et al. Functional imaging of the nonhuman primate Placenta with endogenous blood oxygen level–dependent contrast. *Magn Reson Med*. 2016;76(5):1551-1562. doi:10.1002/mrm.26052

148. Kliewer MA, Bockoven CG, Reeder SB, Bagley AR, Fritsch MK. Ferumoxytol-enhanced magnetic resonance imaging with volume rendering: A new approach for the depiction of internal placental structure in vivo. *Placenta*. 2023;131:104-110. doi:10.1016/j.placenta.2022.12.001

149. Kliewer MA, Bagley AR, Reeder SB, Iruretagoyena JI, Bockoven CG, Fritsch MK. Normal placental structural anatomy: ultrasound and doppler features elucidated with US-MR image fusion and ferumoxytol-enhanced MRI. *Abdom Radiol (NY)*. 2023;48(2):744-751. doi:10.1007/s00261-022-03758-0

150. Kliewer MA, Bockoven CG, Reeder SB, et al. Ferumoxytol-enhanced MR demonstration of changes to internal placental structure in placenta accreta spectrum: Preliminary findings. *Placenta*. 2023;134:1-8. doi:10.1016/j.placenta.2023.02.003

151. Chen R, Seiter D, Keding LT, et al. Cotyledon-Specific Flow Evaluation of Rhesus Macaque Placental Injury Using Ferumoxytol Dynamic Contrast-Enhanced MRI. *Journal of Magnetic Resonance Imaging*. Published online February 20, 2024. doi:10.1002/jmri.29291

152. Chen R, Logan K, Vazquez J, et al. Vascular Assessment of Rhesus Macaque Placental Injury through Maternal Intervillous Blood Volume Measurement. In: *Proc 31st Annual Meeting ISMRM (2023)*.

153. Abulnaga SM, Turk EA, Bessmeltsev M, Grant PE, Solomon J, Golland P. Placental Flattening via Volumetric Parameterization. *Med Image Comput Comput Assist Interv*. 2019;11767:39-47. doi:10.1007/978-3-030-32251-9_5

154. Sletner L, Yajnik CS, Turowski G, et al. Placental weight, surface area, shape and thickness - Relations with maternal ethnicity and cardio-metabolic factors during pregnancy. *Placenta*. 2024;148:69-76. doi:10.1016/j.placenta.2024.02.002

155. Bartels HC, Postle JD, Downey P, Brennan DJ. Placenta Accreta Spectrum: A Review of Pathology, Molecular Biology, and Biomarkers. *Dis Markers*. 2018;2018:1507674. doi:10.1155/2018/1507674

156. Zanganeh S, Hutter G, Spitler R, et al. Iron oxide nanoparticles inhibit tumour growth by inducing pro-inflammatory macrophage polarization in tumour tissues. *Nat Nanotechnol*. 2016;11(11):986-994. doi:10.1038/nnano.2016.168

157. Mohammadzadeh A, Alizadeh S, Shojaie L, Mohammadzadeh M. Association between iron deposition in splenic,hepatic and myocardial tissues assessed by T2* relaxometry technique. *Caspian J Intern Med*. 2021;12(4):600-605. doi:10.22088/cjim.12.4.600

158. Deshmane SL, Kremlev S, Amini S, Sawaya BE. Monocyte chemoattractant protein-1 (MCP-1): an overview. *J Interferon Cytokine Res*. 2009;29(6):313-326. doi:10.1089/jir.2008.0027

159. Chen B, Duan J, Chabot-Lecoanet AC, et al. Ex vivo magnetic resonance angiography to explore placental vascular anatomy. *Placenta*. 2017;58:40-45. doi:10.1016/j.placenta.2017.08.002

160. Neelavalli J, Krishnamurthy U, Jella PK, et al. Magnetic resonance angiography of fetal vasculature at 3.0 T. *Eur Radiol*. 2016;26(12):4570-4576. doi:10.1007/s00330-016-4243-4

161. Jacob M, Philip C, Sydney N, et al. Ferumoxytol MRA in the Pregnant Rhesus Macaque. In: *Proc 27th Annual Meeting ISMRM*. ; 2019.

162. Johnson KM, Fain SB, Schiebler ML, Nagle S. Optimized 3D ultrashort echo time pulmonary MRI. *Magn Reson Med*. 2013;70(5):1241-1250. doi:10.1002/mrm.24570

163. Degner K, Magness RR, Shah DM. Establishment of the Human Uteroplacental Circulation: A Historical Perspective. *Reproductive Sciences*. 2017;24(5):753-761. doi:10.1177/1933719116669056